Investigation of weakly hybridized magnetic molecules

Dissertation
zur Erlangung des Doktorgrades
an der Fakultät für Mathematik, Informatik und Naturwissenschaften
Fachbereich Physik
der Universität Hamburg

vorgelegt von
Emil Józef Sierda

Hamburg
2020

Gutachterinnen der Dissertation:	Prof. Dr. Roland Wiesendanger Dr. Maciej Bazarnik
Zusammensetzung der Prüfungskommission:	Dr. Maciej Bazarnik Prof. Dr. Carmen Herrmann Prof. Dr. Nils Huse Prof. Dr. Michael Potthoff Prof. Dr. Roland Wiesendanger
Vorsitzender der Prüfungskommission:	Prof. Dr. Michael Potthoff
Datum der Disputation:	29.05.2020
Vorsitzender Fach-Promotionsausschusses PHYSIK:	Prof. Dr. Günter Sigl
Leiter des Fachbereichs PHYSIK:	Prof. Dr. Wolfgang Hansen
Dekan der Fakultät MIN:	Prof. Dr. Heinrich Graener

ABSTRACT

Advances in molecular spintronics rely on the in-depth characterization of the molecular building blocks in terms of their electronic and, more importantly, magnetic properties. In most of the studies with that aim published till date, the molecular orbitals were strongly hybridized with the substrates' electronic states. Therefore, the investigations did not characterize the molecules but rather the molecule-substrate hybrid system and there have been concerns about how to separate the two contributions to the measured magnetic signal. An efficient approach is the use of an inert substrate for such studies. Its interaction with the adsorbed molecules is usually weak, which is required in order to preserve the molecule's electronic states.

This dissertation deals with the emergence of magnetism in molecules, from understanding of its origin to the description of molecular interactions with a substrate. It is followed by the description of the concept of spin-based logic devices and their experimental realization. The introduction to the measurement technique (scanning tunneling microscopy) is also provided together with its implementation in the experimental setup. In particular the dissertation focuses on the investigations of the magnetic-field response of a single paramagnetic 5,5'-dibromosalophenatocobalt(II) molecule adsorbed on an Fe-intercalated graphene substrate. This substrate is magnetic and interacts only weakly with the adsorbed molecules. The investigations had been performed by means of spin-polarized scanning tunneling microscopy and spectroscopy. The obtained local magnetization curves, spin-dependent tunneling spectra, and spatial maps of magnetic asymmetry for a single 5,5'-dibromosalophenatocobalt(II) molecule reveal its magnetic properties and coupling to the local environment. The molecules are found to be in three magnetic states. Their magnetic moments align parallel or anti-parallel to the magnetic moment of the substrate caused by relatively strong or weak hybridization, respectively. In the latter case, however, the interaction can be weak enough for manipulation of the molecule's magnetic moment with an external magnetic field. The distinct magnetic behavior of the molecule is found to rely on its position relative to the Fe-intercalated graphene moiré structure. Spatial variations of the electronic properties of the substrate surface in combination with the molecule's adsorption geometry determine the level of hybridization between the molecular orbitals and the surface π-system.

ZUSAMMENFASSUNG

Fortschritte auf dem Gebiet der molekularen Spintronik basieren auf dem fundamentalen Verständnis der elektronischen und insbesondere der magnetischen Eigenschaften von molekularen Grundbausteinen. In den meisten der bisherigen Veröffentlichungen Untersuchungen, welche sich mit dieser Fragestellung befassen, sind die molekularen Orbitale stark mit den elektronischen Zuständen des Substrats hybridisiert, weshalb in diesen Arbeiten nicht das Molekül selbst, sondern das Hybridsystem aus Molekül und Substrat charakterisiert wurde. Aus diesem Grund wurden unterschiedlichste Methoden entwickelt, um die Eigenschaften der Moleküle vom darunterliegenden Substrat zu entkoppeln, mit dem Ziel, die unbeeinflussten magnetischen Eigenschaften des Moleküls bestimmen zu können. Ein effizienter Weg ist es, inerte Materialien für solche Untersuchungen zu verwenden. Die Wechselwirkung inerter Substrate ist in der Regel sehr schwach, was eine Grundvoraussetzung für die Erhaltung der molekularen Orbitale darstellt.

Diese Dissertationsschrift befasst sich mit der Entstehung von Magnetismus in molekularen Systemen beginnend mit dem Verständnis über den grundlegenden Ursprung bis hin zur Beschreibung von molekularen Wechselwirkungen mit dem Substrat. Darüber hinaus wird das Konzept von spin-basierten Logikbauelementen und deren experimentelle Realisation vorgestellt und erläutert. Zusammen mit der Darstellung des experimentellen Aufbaus wird ebenfalls die Rastertunnelmikroskopie als wichtigste Messmethode dieser Arbeit eingeführt. Im weiteren Verlauf dieser Arbeit wird der Fokus insbesondere auf die Untersuchung der magnetfeldabhängigen Eigenschaften von einzelnen 5,5'-Dibromcobaltsalophen Molekülen auf der Eisen-interkallierten Grapheneoberfläche gelegt. Hierbei ist entscheidend, dass die mit Eisen interkallierte Oberfläche magnetisch ist und eine nur sehr schwache Wechselwirkung mit den adsorbierten Molekülen zeigt. Die Untersuchungen wurden mittels spin-polarisierter Rastertunnelmikroskopie und -spektroskopie durchgeführt. Aus den gemessenen lokalen Magnetisierungskurven, den spin-abhängigen Tunnelspektren und den Karten der magnetischen Asymmetrie einzelner5,5'-Dibromcobaltsalophen Moleküle lassen sich Rückschlüsse auf deren magnetische Eigenschaften und deren Kopplung mit ihrer lokalen Umgebung ziehen. Für dieses Molekül wurden drei magnetische Zustände gefunden, dessen magnetische Momente parallel bzw. antiparallel zu den magnetischen Momenten des Substrats ausgerichtet sind, was durch eine verhältnismäßig starke bzw. schwache Hybridisierung hervorgerufen wird. Im letzten Fall kann die Wechselwirkung darüber hinaus so schwach sein, dass sich die magnetischen Momente der Moleküle durch ein äußeres Magnetfeld beeinflussen lassen. Das spezifische magnetische Verhalten der Moleküle hängt zusätzlich noch von der relativen Position zum Moiré Muster des mit Eisen interkallierten Graphenes ab. Hierbei bestimmt die räumliche Variation der elektronischen Zustände des Substrats in der Kombination mit der Adsoptionsgeometrie, wie stark die Hybridisation zwischen den molekularen Orbitalen und den Zuständen des π-Komplexes des Substrats ausgeprägt ist.

ACRONYMS

ENIAC – Electronic Numeric Integrator And Computer
STM – Scanning Tunneling Microscopy
STS – Scanning Tunneling Spectroscopy
SP-STM – Spin-Polarized Scanning Tunneling Microscopy
SP-STS – Spin-Polarized Scanning Tunneling Spectroscopy
CoSal – 5,5'-dibromoSalophenatoCobalt(II)
GR/Fe – Fe-intercalated Graphene
DOS – Density Of States
MO – Molecular Orbital
LDOS – Local Density Of States
RKKY – Ruderman-Kittel-Kasuya-Yoshida
DFT – Density Functional Theory
TMR – Tunneling Magneto-Resistance
HOMO – Highest Occupied Molecular Orbital
LUMO – Lowest Unoccupied Molecular Orbital
DC – Direct Current
AC – Alternating Current
UHV – Ultra High Vacuum
LHe – Liquid Helium
LN_2 - Liquid Nitrogen
NEG – Non-Evaporable Getter
SMM – Single Molecular Magnets

CONTENTS

Abstract V

Zusammenfassung VII

Acronyms IX

Contents XI

1 Introduction 1
- 1.1 Dissertation outline 3

2 Magnetism at the nanoscale 5
- 2.1 Magnetism of single atoms 5
- 2.2 Magnetism of molecules 7
  - 2.2.1 Molecular orbital theory 8
  - 2.2.2 Ligand field theory 9
- 2.3 Superexchange interactions 11
- 2.4 Molecules' interactions with substrates 13

3 Spin-based logic device 17
- 3.1 Spintronics 17
- 3.2 All-spin logic operations 18
- 3.3 Molecule-based spin logic device 20

4 Experimental methods 25
- 4.1 Scanning Tunneling Microscopy 25
  - 4.1.1 Quantum tunneling 27
  - 4.1.2 The Bardeen tunneling theory 28
  - 4.1.3 Tersoff-Hamann model 29
  - 4.1.4 Chen's derivative rule 30
  - 4.1.5 Spin-polarized tunneling 31
  - 4.1.6 Elastic tunneling to molecules 32
  - 4.1.7 Lock-in amplifier 34
  - 4.1.8 Modes of operation 36
  - 4.1.9 Normalization 39
- 4.2 Experimental setup 41
  - 4.2.1 Low-Temperature UHV System 41
  - 4.2.2 Modifications 45

5 SP-STM investigations of molecules 51

6 Results and discussion 55
  6.1 Probe tip preparation 55
  6.2 Sample preparation 57
  6.3 Adsorption geometry of CoSal molecules 59
  6.4 Single atom magnetometry on CoSal metal center 62
  6.5 Field dependent spectroscopy investigations 69
  6.6 Influence of the adsorption geometry on the magnetic state of CoSal 74
7 Conclusions and outlook 77
  7.1 Main results 77
  7.2 Future prospects 77
References 79
Publications 89
Conference contributions 91
Acknowledgments 93

1 INTRODUCTION

"(...) no one person can be the master of more than a small corner of human knowledge. People have to specialize, in narrower and narrower fields."

~ Stephen Hawking

These words from one of the greatest physicists of the XXI century are the best description of how hard it is to make an impact in the vast field of physics. Scientists in the current age must be extremely focused and relentless in their own respective fields, while still taking interest in all of the other wonderful scientific discoveries, physical or otherwise. Some people say that the science was easier in the past as there was plenty of room to grow. I think we can be only grateful that this growth happened and now we live in a world in which the laws of nature are way better understood. This leads to technological advancement which serves our society. The time of the biggest known scientific and engineering boost, caused by obvious circumstances, was the second world war. During that time the pressure to obtain faster and more accurate calculations for military and scientific problems was of highest importance. For that purpose, the first general purpose electronic computer was built. The Electronic numerical integrator and computer (ENIAC) allowed for a 2400-fold speed increase over human-based calculations. It can be considered an ancestor of the computers we know today, which can deal with complex problems at once and deliver an answer very quickly.

The invention of the transistor and its later integration in a circuit marked the beginning of a new era of computers. They became smaller, faster, more reliable and far more energy efficient. In 1965 Moore predicted that the number of transistors in dense integrated circuits will double every year.[1] A decade later he revised his prediction to double the count every two years.[2] His prognosis was unprecedently accurate and the incredible progress it described led to the technological revolution which we, as a society, were a part of in the past few decades. Moore's prediction (sometimes called a law) was accurate till 2016 and as for today the development slowed down and diverted from it. The main cause is the challenging production of 10 nm, 7 nm and 5 nm node chips. However, there is a much bigger problem behind the next corner, as it is predicted that a technological limit exists at around 2-3 nm gate size. This limit is caused by physical phenomena which become more apparent at such small sizes *i.e.* quantum uncertainty. This will make transistors unreliable and, as a consequence, unusable.

Alongside miniaturization there are two other barriers to the progression of today's information processing technology – speed and energy efficiency. The speed of a single transistor is limited by how fast it can change its state. The current record for a transistor state change is 798 GHz (at 4.3 K) for a SiGe heterojunction bipolar transistor.[3] However, not only does it require the use of a new material (SiGe instead of Si), but also a bigger gate size of 130 nm and much higher (over 2 times) energy consumption. This approach follows a "More than Moore" philosophy[4] and shows the complexity level of the progress. The problems do not stop with the transistor speed. As a result of the Moore's law the chips became very tightly packed. In combination with the higher energy consumption coming with increased clock speeds, the chips get very hot. This is a major problem with which integrated circuit technology struggles for almost 20 years now. The leading technology companies realized that all of the features of a transistor are linked together and the technology cannot advance in only one field. Instead, they redirect their development with a "More than Moore" strategy and focus on changing the chip architecture or working on new materials. However, it seems that this approach cannot take us much further. In order to overcome the node size limit while pushing the information processing to be ever faster and more energy efficient, we must enhance our efforts in science and technology to develop totally new solutions.

Nowadays, we stand on the verge of a new era of computing and the next few years will show us the best way to progress in the future. For now, there are plenty of great ideas and developments such as molecular electronics,[5-7] quantum electronics[8-9] or spintronics[8,10-14]. To date, however, none made it out of the laboratory. Among these new developments the field of molecular spintronics is promising enough to be considered as a prospect. In this approach, specially designed metalo-organic molecules are connected in networks. Their magnetic metal centers are the functional parts carrying and performing logical operations, with the spins of their electrons being used as a carrier of information instead of their charge. This allows for faster (THz frequency range[15]) and more energy efficient transport and processing of information at a scale of ~1 nm.

Molecules are fascinating creations of nature. They surround us and make fundamental processes in living organisms possible – gas transport in blood, vision, photosynthesis and cell replication to name a few. The usefulness of molecules is not only limited to natural processes however. Humans learned ages ago how to use them for medical purposes or to produce dyes, and in the last century for light emitting diodes or solar cells. In fact, chemistry is so developed today that one can produce virtually any molecule; shape, size and properties can all be chosen. Thanks to this, molecules could possibly take over most current solid-state applications and prove to be the ultimate functional units of future technologies.

The physical and chemical properties of molecules (and other systems on the nanoscale) can be determined using a number of experimental techniques. Scanning tunneling microscopy (STM) and spectroscopy (STS) are well suited tools for this purpose. With their spin-polarized versions (SP-STM/STS) both electronic and magnetic properties can be accessed with high energy and sub-molecular spatial resolution. The characterization of any molecule using this technique requires a substrate on which the molecules are adsorbed. Unfortunately, in such case the substrate influences and alters the molecule's original properties. Effectively a molecule-substrate hybrid system with novel properties is created. Sometimes such influence is desirable and useful while in other cases it is undesirable. The latter applies to the case of studies aimed at the characterization of molecules used in molecular spintronics. Therefore, the magnetic molecules, which need to be characterized, must be somehow decoupled from the substrate's influence on the measured electronic and magnetic signal. One approach is the use of an inert substrate for which the interaction with the adsorbed molecules is usually weak. It allows the molecule to preserve its electronic states and magnetic properties.

1.1 Dissertation outline

In the framework of this dissertation, the magnetic properties of a 5,5'-dibromosalophenatocobalt(II) (CoSal) molecule adsorbed on an Fe-intercalated graphene (GR/Fe) surface, as well as the possibility of manipulation of its magnetic moment are presented. The GR/Fe substrate, being a ferromagnet, stabilizes the magnetic moment of the paramagnetic CoSal molecule, making it suitable for spin-polarized scanning tunneling microscopy studies.

The emergence of magnetism at the nanoscale is given in Chapter 2. It includes the description of the magnetism from single atoms and molecules to the description of their interactions with the substrate.

The concept of a spin-based logic device is presented in Chapter 3. It includes a description of logic operations based on the spin degree of freedom, as well as a first realization together with the challenges for further improvements. Further on, an approach to address some of those challenges by implementing molecules in the design of such all-spin logic devices and the progress that had been made in this regard are presented.

In Chapter 4, all the subjects regarding the experiment are covered. Starting with the topics related to the experimental technique, *i.e.* STM; theory of tunneling from the one-dimensional case to spin-polarized tunneling and tunneling in the presence of molecules. After this, the experimental setup is described in detail together with all the modifications necessary for the successful realization of the experiments.

Chapter 5 presents the current status of STM investigations on single magnetic molecules adsorbed on various substrates, including shortcomings which are the motivation for the experimental studies presented in chapter 6.

The experimental results are presented in Chapter 6. The chapter starts with a description of probe tip and sample preparations used in the experiment. Next, I present a way to detect the behavior of a single paramagnetic CoSal molecule in an external magnetic field and a way to manipulate it. By investigating many CoSal molecules, I observed their distinct behavior in different adsorption sites on the GR/Fe moiré structure. In some cases, this led to a weak hybridization of the molecule and substrate electronic states and made it possible to manipulate the molecule's magnetic moment direction, independent from the substrate, using the external magnetic field.

Chapter 7 summarizes the findings and concludes the discussion on the topic of this dissertation.

2 MAGNETISM AT THE NANOSCALE

Any spintronic device operation is based on inherent properties of magnetic matter – the spin. This chapter provides an introduction to magnetism at the nanoscale, from single atoms up to their interactions with other atoms while forming a molecule, and finally the interactions with a substrate the molecules are being adsorbed on.

The main types of magnetism are ferromagnetism, antiferromagnetism, paramagnetism and diamagnetism. The first two are demonstrations of collective interactions of magnetic moments by exchange interactions which give rise to strong and long-range magnetic order. In case of ferromagnetism all magnetic moments align parallel and are characterized by spontaneous magnetization appearing without an external magnetic field. An alternating alignment of the magnetic moments gives rise to antiferromagnetism which is accompanied by zero net magnetization. Paramagnetism also originates from permanent magnetic moments but unlike the previously mentioned types of magnetic order the interactions between separate moments are negligible. Therefore, the magnetic moments can orient themselves freely in any direction. An external magnetic field induces order in this type of materials and causes the separate magnetic moments to align parallel to the field direction. Lastly, diamagnetism is a weak repulsive response of a non-magnetic material to an external magnetic field. The following is based in parts on the information from following books: Ref. [16-22].

2.1 Magnetism of single atoms

The magnetic moment of single atoms is of dual nature: (1) The spin magnetic moment μ_s is of purely quantum-mechanical origin. The magnitude of the projection of the electron's spin along an arbitrary axis equals $\frac{1}{2}\ \hbar$, implying that the electron acts as a fermion by the spin-statistics theorem. The magnitude of the spin magnetic moment is expressed as $\mu_s = -2\ \mu_B\ S$, where μ_B is the Bohr magneton and S is the total spin. (2) The orbital moment μ_l is present due to the motion of an electron around the atom's nuclei. It has the form $\mu_l = -\ \mu_B\ L$, where L is the total orbital angular momentum. That number takes values $L = 0,\ 1,\ 2$ and 3 corresponding to s, p, d and f-like states, respectively. Although the two types of magnetic moments are separate and should be treated as such, they can experience a coupling. The relative motion of the electron and the nucleus creates a magnetic field acting on the spin magnetic moment which is a source of the spin-orbit coupling. Its energy is given by $E = \lambda\, L \cdot S$, where λ is the spin-orbit coupling constant. In full shells all of the spin and orbital contributions tend to compensate each other and the resulting magnetic moment is zero. Therefore, magnetism can occur only in atoms with partially filled electron shells.

Each element of the periodic table consists of a different set of electrons orbiting the nucleus. Their distribution within the available orbitals aims to minimize the energy of their mutual electrostatic repulsion and is governed by the Hund's rules. The first rule states that the lowest energy atomic state is one that maximizes S under the constraint of the Pauli exclusion principle, *i.e.* in each spatial orbital there is room for only two electrons with spins being anti-parallel to each other. The second rule aims to reduce repulsion between electrons and states that the term with the largest value L has the lowest energy. As example, a Co atom has a ground state configuration of: 1 s^2, 2 s^2, 2 p^6, 3 s^2, 3 p^6, 3 d^7, 4 s^2. The ground state configuration is visualized by a schematic with an energy scale in Fig. 2.1a. The only unfilled orbital is 3 d where one can see three unpaired electrons from which the magnetism of this element arises from.

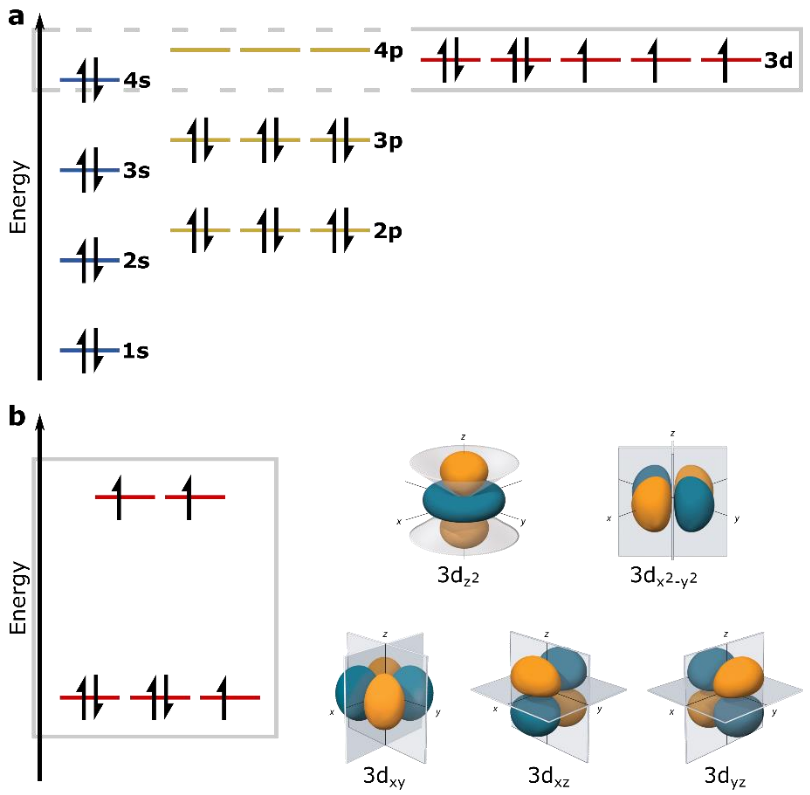

Figure 2.1 Ground state electron configuration of Co. (a) Atom in gas phase. (b) Energy position and 3D representations of 3 d orbitals with lifted degeneracy in octahedral geometry. (Orbitals' geometry adapted from Ref. [23] under CC license.)

The degeneracy can be removed if the underlying symmetry is broken by an external perturbation (*e.g.* other atoms or fields). Such situation is a focus of the following section. Here, it is important to point out that the considered Co atom's 3 *d* orbitals upon lifting degeneracy, will usually result in two energy levels (Fig. 2.1b). The lower energy level consists of 3 d_{xy}, 3 d_{xz} and 3 d_{yz} orbitals, one of which with an unpaired electron while the higher energy consists of 3 d_{z^2} and 3 $d_{z^2\text{-}y^2}$ orbitals, both with one unpaired electron. When adsorbed on a surface or incorporated in a molecule the Co atom's 3 *d* orbitals can produce a different splitting into three or four discrete energy levels favoring different orbitals than presented above (*e.g* a Co atom adsorbed on a MgO surface[24]).

2.2 Magnetism of molecules

In a molecule magnetism can arise from an unpaired electron spin in purely organic molecules or from the incorporation of magnetic metal atoms. Fig. 2.2a shows a model of an organic molecule which contains C, N, O and H atoms. The graph to the right corresponds to the model of a molecule (to the right) and presents the total density of states (DOS) for the two spin channels: spin-up (red) and spin-down (blue) and their difference (dotted black). The difference of the two spin channels is zero for all the energies, and therefore the molecule is not magnetic and its magnetic moment equals zero. Creating a radical by taking away two H atoms, formerly bonded to O atoms, (Fig 2.2b) renders the molecule magnetic which is apparent when comparing the two spin channels or looking at their difference. This molecule has two unpaired electrons and a total magnetic moment of 2 μ_B localized on O atoms. This organic molecule is also capable of reacting with a metal atom. A model of a molecule with a Co atom incorporated in its center is shown in Fig 2.2c. In this state the molecule is also magnetic. However, the magnetism in this case is of different origin than in the case of the radical mentioned before. As discussed in the previous section, the Co atom has three unpaired electrons in its free state. While reacting with this organic molecule, two of the orbitals are filled with electrons supplied by the molecule's O atoms. Therefore, the final product has only one unpaired electron and a total magnetic moment of 1 μ_B localized mainly on the Co atom.

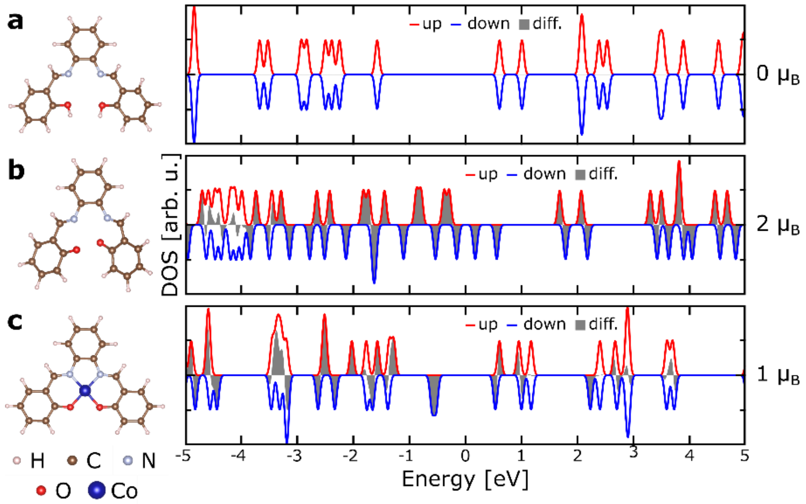

Figure 2.2 Models and density of states of two separate spin channels calculated using density functional theory.[25] Cases for three molecules: (a) salophene, (b) salophene radical (two H atoms are removed) and (c) salophenatocobalt(II). The total magnetic moment of each corresponding molecule is provided to the right of the graphs.

2.2.1 Molecular orbital theory

Interaction of atoms within a molecule (or a cluster) will cause a deformation of atomic orbitals and result in their new distribution which no longer can be described using single unperturbed atomic orbitals. New orbitals which can be described by a linear combination of at least two atomic orbitals are therefore created. The process is called hybridization and involves orbitals which have a similar energy, even ones which belong to the same atom. Hybridization of specific atomic orbitals is the main reason for the specific atom arrangement within molecules and molecular assemblies. Linear arrangements are given by *sp* hybridization, planar by sp^2 or sp^2d hybridization, tetrahedron by sp^3 hybridization, octahedron by sp^3d^2 hybridization *etc.* The resulting molecular geometries reflect the minimum energy electron configuration (ground state). Therefore, the energy levels of orbitals shift towards lower energies upon hybridization due to electron delocalization. The hybridized orbitals of all the atoms comprising of the molecule create a complicated molecular orbital (MO). Its spatial distribution can be very different from the shape of the original orbitals. As an example, some of the orbitals of the salophenatocobalt(II) molecule are presented in Fig. 2.3. Only two MOs partially resemble the geometry of the original Co 3 *d* orbitals (marked by green rectangle in Fig. 2.3): $3d_{xy}$ and $3d_{z^2}$.

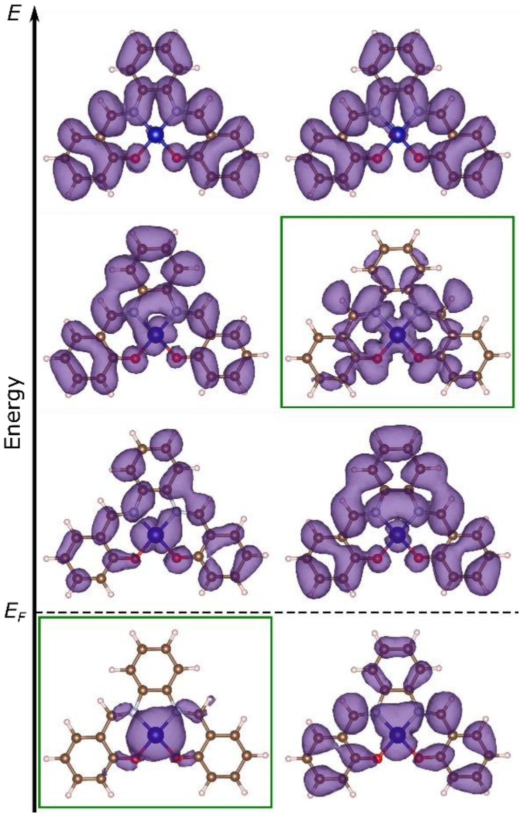

Figure 2.3 Selected molecular orbitals of salophenatocobalt(II) calculated using density functional theory.[25] Two of them partially resembling the original geometry of 3*d* orbitals are boxed in green rectangle.

2.2.2 Ligand field theory

Magnetism emerging in molecules with a magnetic atom is different from the case of hybridizing orbitals. The way magnetic atoms behave in such circumstances is described by crystal field theory. The theory was developed by Bethe[26] and van Fleck[27]. The first results obtained using that method gave an orbital splitting being an order of magnitude smaller than experimentally observed. Better results were obtained when combining crystal field theory with molecular orbital theory used for a better description of the symmetry of the system. The combination is known as ligand field theory and is successfully used for modelling magnetic interactions in various systems.

The idea behind ligand field theory is that the metal ions are influenced by surrounding atoms *via* electrostatic attraction. The electrostatic potential of the molecular environment hinders the ease of the electrons responsible for magnetism in following the Hund's rules. As a result, an anisotropy is induced in the orbital angular momentum and, through spin-orbit coupling, the same happens to the total magnetic moment. In a simplified model, each of the electrons can be treated separately. The interaction is then described in the simple fashion of constructing the energy level scheme for each orbital symmetry and filling them with electrons following the Pauli principle. The different symmetries of the orbitals will result in distinct energy levels in a given ligand field. The two symmetries which are particularly important are tetrahedral and octahedral as other symmetries can be considered as perturbation of the two. In tetrahedral symmetry triplet is of higher energy than doublet, while in octahedral symmetry it is the opposite. As a next step, the electron interactions are taken into account in ad hoc fashion. The correlation between electrons (exchange and Coulomb) will determine two unique ground states: high spin state or low spin state. If the interaction is large relative to the ligand field energy splitting, all of the energy levels are successively filled with electrons of the same spin and electrons with opposite spins are added only after. This leads to the high spin ground state. In contrast, if the ligand field splitting energy is much higher than the electrons' interaction energy, than electrons will only fill lower energy states giving the low spin ground state. If one would like to consider the true multi-electron character of an ion, however, another approach must be used. Multiplet ligand field theory focuses on the intra-atomic Coulomb and exchange interactions between the electrons and uses multiplet theory to determine the symmetry group of the ligand field. The symmetry group obtained in this way determines the splitting of the multiplets and the splitting energy is given by the Tanabe-Sugano diagrams.[28-29]

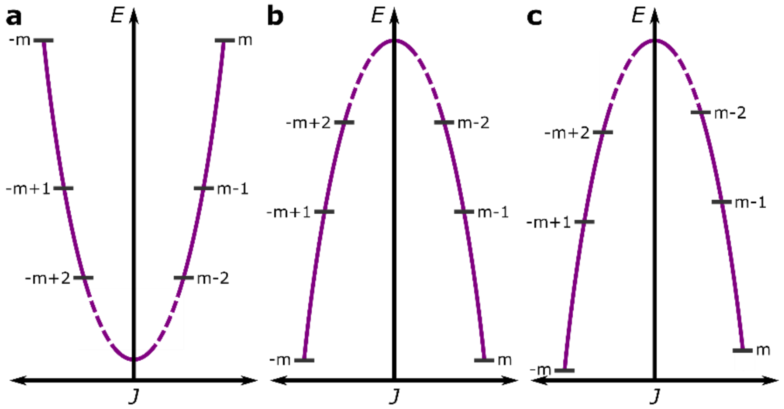

Figure 2.4 Schematic of anisotropic spin states for a magnetic atom in a ligand field. (a) Easy-plane and (b) out-of-plane uniaxial anisotropy. (c) The states shift linearly with additional external magnetic field applied in the out-of-plane case.

The ligand field acting on a magnetic ion results in the introduction of anisotropy to otherwise degenerate spin states. The ligand field can have one of two dominating anisotropies: easy-plane (Fig. 2.4a) or out-of-plane (Fig. 2.4b). They both show an energy separation between ground states which must be overcome in order to switch the magnetization direction. Introduction of an external magnetic field causes the states to shift according to the Zeeman energy. An example is provided for the out-of-plane case in Fig. 2.4c.

The mechanisms described above can occur for clusters, molecules or simply single atoms adsorbed on a substrate. They often lead to quenching of the spin and as a consequence to the disappearance of the atom's magnetic moment. The only elements for which magnetism remains when they are comprised in a larger assembly of atoms are the 3 *d* transition metals and the rare earth elements: (1) the 3 *d* series of transition metal elements corresponds to a progressive filling of the 3 *d* shell and includes atoms from Scandium to Zinc. The behavior of these atoms depends strictly on the local environment they are in. In insulating systems (*e.g.* oxides) the 3 *d* electrons remain localized. They behave as in an isolated atom and their magnetic moment is defined by the Hund's rules. In metallic systems, on the other hand, they form an energy band and their magnetic moment is created on the larger multi-atom scale. The exchange interaction will favor one of the two sub-bands (spin-up or spin-down) to be of lower energy than the other. The state of the system will therefore be defined by the strength of the exchange interaction. (2) The rare earth series of elements corresponds to a progressive filling of the 4 *f* shell and includes atoms from Cerium to Lutetium. The character of 4 *f* orbitals renders the electrons residing in them to be localized and behaving as in an isolated atom. Therefore, their magnetic moment is defined by the Hund's rules. The strength of magnetic interactions differs for those two groups of elements. The 4 *f* series is much more susceptible to spin-orbit coupling but less prone to interactions with the ligand field due to a much more efficient shielding of that shell by other shells.

More details on the topic of ligand field theory can be found in the book by Bellhausen.[30]

2.3 Superexchange interactions

The basic mechanism of coupling between two magnetic atoms is based on the simple fact that when their wavefunctions overlap, electrons of the same spin cannot occupy the same position due to the Pauli exclusion principle. The direct exchange coupling can be of Coulomb energy origin (basis for Hund's first rule) or kinetic energy origin. However, when the distance between two magnetic atoms is too large, the electrons cannot hop between orbitals of neighboring atoms as their wave functions do not overlap. In such case no direct exchange interaction can take place. Yet, the collective magnetism can be mediated indirectly. The three main indirect magnetic exchange interactions are: RKKY interaction, superexchange interaction and double exchange interaction. Superexchange is a type of exchange interaction which occurs mainly in ionic solids. The exchange between magnetic ions is mediated by the intermediate *p* orbital. The mechanism was first observed and explained for salts by Kanamori[31] in 1958 and its full theoretical concept was described by Anderson[32] in 1959.

There are two main cases for superexchange interaction: 180° case and 90° case. Both are depicted in form of the orbital symmetry and the electron occupation in Fig. 2.5. For clarity the models are simplified here: metal (M) atoms are assumed to be magnetic and have only one unpaired electron, while intermediate atoms (here O) show a tendency to attract two electrons. The 180° case (Fig. 2.5a) is the simpler example where all three atoms are bonded along one axis. The 3*d* orbitals of both of the M atoms overlap with the 2 *p* O orbital. The ground state will have singly occupied *d* orbitals and doubly occupied *p* orbitals, corresponding to an M^+ ion and to an O^{2-} ion, respectively. Analysis of the possible excited states after hopping events leads to the conclusion that the only possible coupling between the metal atoms is antiferromagnetic. The ferromagnetic coupling is excluded by the Pauli principle which suppresses hopping of the second electron. The strength of the interaction depends on the magnitude of the magnetic moments, orbitals overlap and bond angle deviation off the axis.

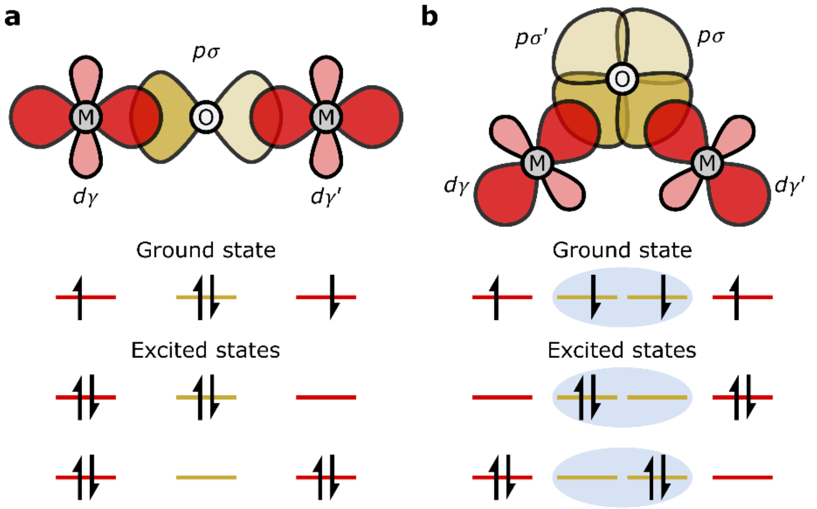

Figure 2.5 Schematic of a superexchange interaction in two cases: (a) 180° and (b) 90°. Orbital symmetry on the top depicts the mutual position of the overlapping orbitals and their electron occupation is presented below for ground state and excited states. The orbitals are depicted as orbital charge densities (wavefunctions squared), where the more color intense part corresponds to the positive and the less color intense part to the negative sign of the wavefunction.

The situation is quite different if the intermediate atom is not positioned in between two metal atoms. In 90° case the intermediate atom creates an off-axis bridge (Fig 2.5b). By symmetry the only possible hopping is between the *d* and the *p* orbitals that point towards each other, *i.e.* $d\gamma \leftrightharpoons p\sigma$ and $d\gamma' \leftrightharpoons p\sigma'$. The two sites are thus separated and each involves only a d orbital and one of the p orbitals on each side (p_x or p_y). The interaction between the two sides is mediated by the Coulomb exchange between the orbitals within the intermediate atom. Following the Hund's first rule, the Coulomb exchange prefers a triplet for two electrons in different orbitals on the same site. Hence, the ground state of this case contains all orbitals involved being singly occupied. Two mirror excited states are possible: when the electrons hop from the d-orbital to the p-orbital the entanglement of the spins is transferred to the remaining electron on the other d orbital. The 90° case can also be considered as a manifestation of the double exchange mechanism as it combines Coulomb and kinetic exchange.

The antiferromagnetic 180° superexchange interaction is significantly stronger than the ferromagnetic 90° coupling. In some cases, the angle of the M-O-M group falls in the 90-180° range. In such scenario the antiferromagnetic superexchange competes with the ferromagnetic superexchange due to a possibility of electron hopping between p-orbitals according to the Slater-Koster rules.

2.4 Molecules' interactions with substrates

For most experimental techniques used for studies of electronic and magnetic properties of nanoscale objects it is essential to have a substrate as a support for those objects. This results in an influence on the probed properties by the very existence of that substrate and its type. For some purposes and applications this influence is desirable while for others it is unwanted. Studies of a variety of single atoms adsorbed on different substrates led to an understanding of the phenomena occurring in such systems[33-35]. However, the smaller the adsorbed nanoobject one wishes to investigate and understand, the bigger the problem of understanding its own behavior and exclude the influence of the substrate. For small molecules adsorbed on supporting substrates their orbitals strongly hybridize with the substrates' electronic states[36-38]. (More details about investigations of magnetic molecules are provided in Chapter 5.) Based on this fact, there have been concerns about how to separate contributions of the molecules and the substrate to the measured electronic and magnetic signal.

The best visualization of this problem was presented by Brede *et al.*[37] Their work revealed what happens to the molecule's electronic states while it gets closer to the substrate and further to the point when the molecule adsorbs on the substrate and their states hybridize. This is presented in Fig. 2.6 (adapted from that work). When the molecule is far away from the substrate (Fig. 2.6a) it has a magnetic moment and defined energy levels for its orbitals. The origin of the total molecular spin S=1/2 is an unpaired electron of the Co atom's d_{z^2} orbital contributing to the molecular orbital. While approaching the substrate charge is transferred to the molecule and the energy levels shift and broaden. In Fig. 2.6b one can see a situation when the molecule is very close to the surface but cannot yet be considered adsorbed. In this situation the spin-polarized local density of states (SP-LDOS) shows a significant hybridization of the molecule's and the substrate's states. The strongest hybridization is observed for the molecular orbitals extending perpendicular to the molecule plane, *i.e.* the ones containing p_z, d_π and d_{z^2} Co atom orbitals. Due to the transfer of an electron from the substrate to the molecule the d_{z^2} type molecular orbital becomes occupied and the magnetic moment of the molecule is quenched. The hybrid obtained upon molecular adsorption is magnetic but its properties are dictated by the substrate. Its band structure is presented in Fig. 2.6c. Due to the molecule's deformation in this adsorption geometry the hybridization is even stronger and now involves d_σ type molecular orbitals. The magnetism of this hybrid arises from an unbalanced, locally varying electronic charge in the spin-up and spin-down channels.

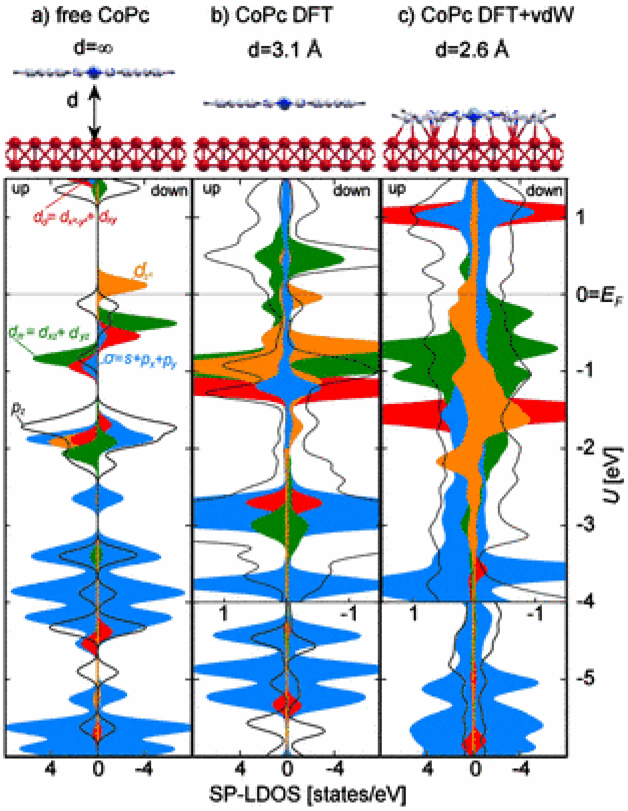

Figure 2.6 Change of electronic structure of a molecule with increasing molecule-substrate interaction. (a) Free standing molecule far away from the substrate, (b) molecule close to the substrate and influenced by it, (c) relaxed molecule adsorbed on the substrate with van der Waals forces included. (Reprinted with permission from Ref. 37. Copyright 2010 by the American Physical Society.)

It is therefore clear that there is a need to separate the molecule from the substrate and prevent it from hybridization which would alter the molecule's magnetic properties. Molecule's hybridization can be prevented by the deposition of molecules on substrates held at low temperatures: 78 K for semiconductor substrates[39] and 20 - 25 K for metal substrates[40-41]. It renders molecules to be only physisorbed on the metallic substrate due to the lack of energy for chemical bond formation. A spatially averaged study presented by Javaid *et al.*[38] shows that molecules can be physisorbed even at room temperature and keep their magnetic properties. This situation is explained by the small hybridization due to the lack of out-of-plane bonds between the molecule and the substrate, and the absence of charge transfer to the molecule. Other studies suggested that a single molecule adsorbed on a thin layer of an insulating material is efficiently decoupled from the metallic substrate leading to low hybridization.[42-45]

3 SPIN-BASED LOGIC DEVICE

Within this chapter I focus on describing concepts of spintronics and logic operations performed using spins, instead of electron charge, with a specific execution example. After providing all the background information I turn to the presentation of molecule-based all-spin logic devices and challenges for their successful realization.

3.1 Spintronics

The technology in which the electron charge is used as a carrier of information is widely known as electronics. Spintronics (a name first proposed by Wolf *et al.*[46]), is a concept in which information is carried and processed by either the combination of the electric charge and the electron's intrinsic spin (spin-polarized current) or using the spin alone. The main advantages of this approach are higher speeds of operation, increased integration density (ultimately small size) and higher energy efficiency compared to traditional semiconductor-based electronics. As in case of current information processing technology, a spin-based analogue must incorporate bi-stability, means of changing the input and read-out of the output. Employing the spin degree of freedom not only meets those requirements but exceeds them. It can provide more than two stable states, *e.g.* when using spins as qubits in quantum computing.

Spintronics emerged from observations of spin-polarized electron injection from ferromagnet to a non-magnetic metal[47] and the discovery of giant magnetoresistance[48-49]. In that phenomenon, the device resistance can be either small or large depending on the relative orientation of the magnetizations in the magnetic layers. This concept led to the development of non-volatile memory devices which are widely used today. However, spintronics has much more potential for growth, especially if one considers application in information processing with single atom spins as bits or qubits. The latter opens the possibility to carry out radically new quantum computations, in addition to all previously mentioned advantages. In 1999 the first realizations of charge independent manipulation of electron spins in semiconductors by laser pulses were presented by Gupta *et. al.*[50-51] opening a path for incorporating the spin-degree of freedom in semiconductor electronics and its possible use for logic operations. However, the first spin-based logic operations based on spin-spin interactions of single adsorbed metal atoms were presented in 2011 by Khajetoorians *et al.*[52] That concept is described in more detail in the next section.

3.2 All-spin logic operations

Spintronics offers great potential for the future development of novel types of logic devices. Currently logic devices are based on transistors and other passive electronic components. Such transistor-based logic device cannot be smaller than 200 nm (in 5 nm node available today).[53] Spintronics may lead to logic gates to be as small as a couple of nanometers. The experimental realization of such logic device is presented by Khajetoorians *et al.*[52] The device is based on single atoms aligned using atom manipulation with an STM probe tip and small ferromagnetic islands as input gates. The distinct adsorption geometry of the atoms provides coupling *via* distance-dependent RKKY magnetic exchange mediated by the conduction electrons.[54] The whole concept is presented in Fig. 3.1. Two ferromagnetic islands of different size are used as a signal input which is further transmitted by antiferromagnetically coupled spin leads to the gate area. The gate consists of three antiferromagnetically coupled atoms – two are the ends of each spin lead while one is an output atom. All the logic operations are performed in the gate region. In the whole concept there is no flow of electric charge and the device functions are based solely on spin interactions.

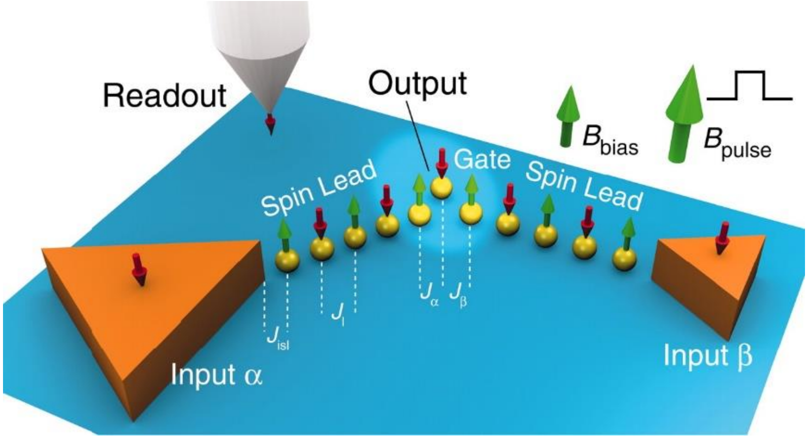

Figure 3.1 Concept of an atomic spin logic device. (From Ref. 52. Reprinted with permission from AAAS.)

For this concept to work a special case regarding the interplay of the exchange interactions of the two input islands with the output atom (J_α and J_β) and the spin lead exchange interaction (J_l) must be met: $J_l > J_\alpha = J_\beta$. It means that if the input states are equal, the output atom will align antiparallel to that state and if the inputs are of opposite orientation, the output will be magnetically frustrated. In order to break that frustration and make the device operation possible, a small biasing magnetic field is applied (B_{bias} = 0.25 T). This field is small enough not to interfere with the state of either spin lead but sufficient to make one of the inputs energetically favorable. The state of the device can be changed by application of out-of-plane external magnetic field pulses (B_{pulse}) of different magnitude and direction. The bigger the input islands, the stronger magnetic field is needed to change their state. The magnitude needed to align input α island with the external magnetic field is B = |1.75 T| while for the smaller input β island it is B = |0.4 T|. The STM topography images (side view in 3D) of the experimental realization is presented in Fig. 3.2. The four different states obtained prove this all-spin based operation behaves like an OR logic gate.

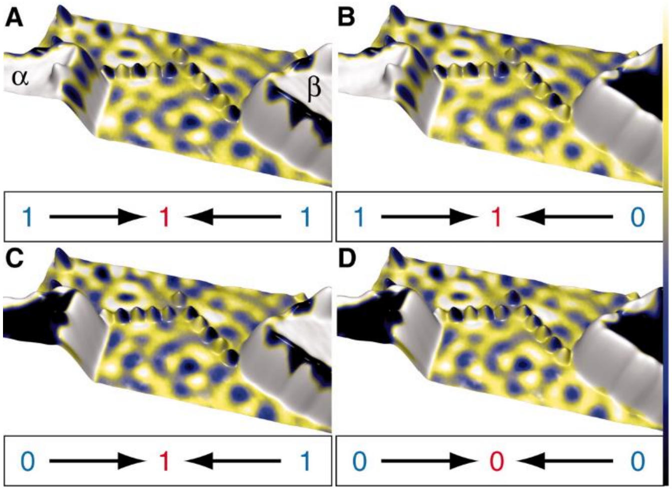

Figure 3.2 Experimental realization of an OR gate. Magnetic field pulses used between the steps: A to B - B_{pulse} = - 0.39 T; B to C - B_{pulse} = - 2 T & + 0.75 T; C to D - B_{pulse} = -0.39 T (From Ref. 52. Reprinted with permission from AAAS.)

The proposed approach can as well be used to create other logic gates by simply changing the parity of each spin lead. It is important for the spin leads to be of equal length. Otherwise, the magnetic stability of the shorter spin lead will be higher than for the longer one (the strength of the RKKY interaction decreases with increased atomic chain length) and the gate operation will be governed only by its input. For the odd spin lead length an OR gate will be obtained (Fig. 3.3a) while for an even spin lead length it will be a NAND gate (Fig. 3.3b). Extending the output by another atom (green) will lead to a negation of the operation result and consequently to NOR and AND logic gates, respectively.

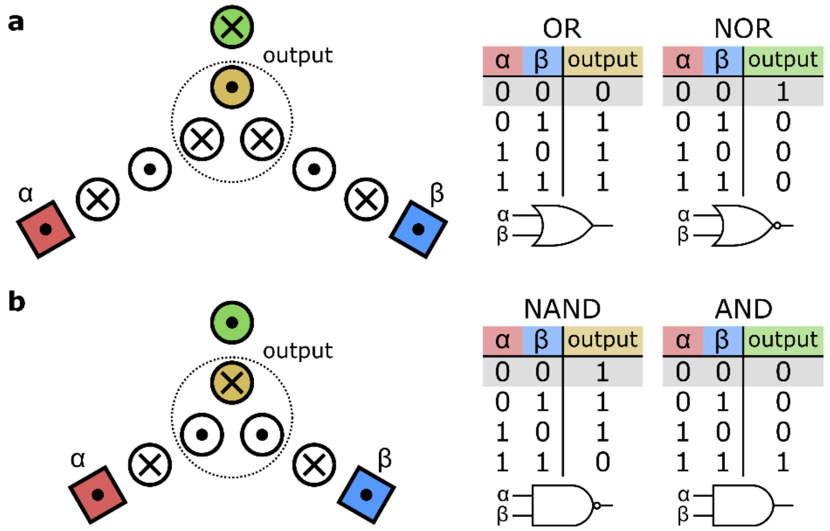

OR

α	β	output
0	0	0
0	1	1
1	0	1
1	1	1

NOR

α	β	output
0	0	1
0	1	0
1	0	0
1	1	0

NAND

α	β	output
0	0	1
0	1	1
1	0	1
1	1	0

AND

α	β	output
0	0	0
0	1	0
1	0	0
1	1	1

Figure 3.3 Possible configurations for different logical gates. (a) Odd and (b) even length of spin leads. Two inputs are marked with red (α) and blue (β) colors while the main output atom is marked with a yellow color and a secondary – extended output is marked with a green color. The gray underline marks configurations visible in the schematics.

The device operation presented here is based on the classical model of magnetic moments pointing in only two directions: up or down with respect to the surface plane, therefore, allowing only for binary operations. However, the use of magnetic atoms with a larger number of quantum states (qubits) available would allow for novel directions in quantum computing.

Despite all its advantages the concept as presented above cannot be scaled to larger architectures because the magnetic stability of the spin lead decreases with its length for RKKY interactions. Moreover, the operating temperature of $T = 0.3$ K (needed for the used antiferromagnetic RKKY interactions) and the assembly of the device atom-by-atom are not ideal for applications either. Some solutions for those problems had been suggested in the original paper, however, employment of covalently bonded molecular networks promises to lead to a more stable spin logic device.

3.3 Molecule-based spin logic device

This scheme is based on the use of molecules with magnetic atoms as spin centers for all-spin based operations. The covalent bonds make the whole device mechanically robust and thermally stable. The presence of a molecular structure effectively renders the device's operation possible, as it provides a strong through-bond magnetic coupling between magnetic metal centers due to superexchange interactions.[31,55-56] The knowledge about chemical reactions and structure of molecules is so advanced today that the design of such molecular spintronic devices is feasible. However, in order to demonstrate their operation, the molecules need to be transferred, after chemical synthesis, from a solution to a substrate. Unfortunately, deposition of large nanostructures is difficult[11] if at all possible and another approach must be employed. Separate parts – building blocks – of the final device can be synthesized, and deposited on the surface separately. Models of various molecules are presented in Fig. 3.4.

Subsequently after deposition, the building blocks must be assembled into a device using either an STM probe tip to connect the molecules to one another[57] or by utilizing an on-surface chemical reaction[58-61] and self-assembly[62]. The latter is the approach of choice as it is easier and much faster. Grill *et al.*[62] proposed a way to control the growth of molecular nanostructures using the same molecule with one, two or four reactive ends to create dimers, chains or grids, respectively. In this case the chemical reaction is the Ullmann coupling[63]. It is a heterogeneously catalyzed reaction in which two aryl halides are coupled to form a biaryl in the presence of a coinage metal. In the on-surface version of this reaction the surface acts as a catalyst.[55,56,59,60,62,64-75]

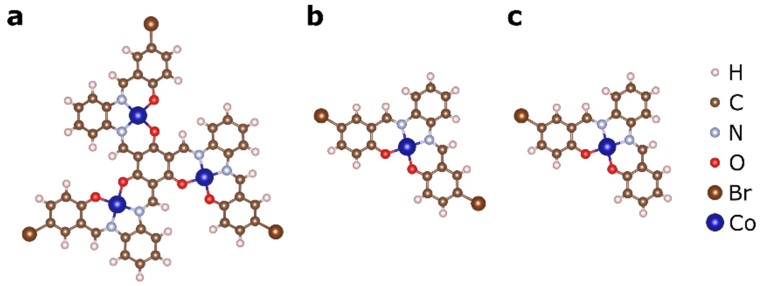

Figure 3.4 Ball-and-stick models of molecules used to build a molecular spintronic device. (a) A junction molecule: tribromo-triplecobaltosalophene, (b) chain link molecule: 5,5'-dibromosalophenatocobalt(II) and (c) chain terminator molecule: 5-bromosalophenatocobalt(II). Atom representations are labelled on the right of the image.

As a junction molecule, the tribromo-triplecobaltosalophene molecule (Fig. 3.4a) was designed and synthesized[56]. This molecule exhibits C_3 symmetry and is nearly planar. The Co atoms embedded in the molecule form an equilateral triangle with distances of about 730 pm. Three bromine atoms at the outermost sites of the molecule are a prerequisite for the selective Ullmann coupling. The building block of a molecular chain – the spin lead – is intended to be a 5,5'-dibromosalophenatocobalt(II) molecule[55] (Fig. 3.4b). This molecule exhibits C_{2v} symmetry, hence, it is planar. Similar to the junction molecule, the Co atom is embedded in the N_2O_2 entity but only two Br atoms are present here on the two outermost sites. Lastly, a 5-bromosalophenatocobalt(II) molecule (Fig. 3.4c) was designed and synthesized[56] as a terminator of molecular chains to optimize their length. It renders the chain end inert and stops chain growth by having only one Br atom. All of those molecules are paramagnetic, the Co atoms are in the second oxidation state with a located unpaired spin S=1/2. Their planar geometries allow for a flat adsorption after deposition on a substrate and easy access by an STM probe tip.

The final product of an on-surface Ullmann reaction of subsequently deposited tribromo-triplecobaltosalophene, 5,5'-dibromosalophenatocobalt(II) and 5-bromosalophenatocobalt(II) molecules in a 1:6:3 ratio is presented in Fig. 3.5. The obtained structure is similar to the design described in section 3.2 and consists of a junction connecting three chains: three mers long on the left, four mers long on the right and two mers long on the top. By changing the ratio of the used molecules, it is possible to tailor the chains to the preferred length. Such kind of study had also been performed and presented.[74]

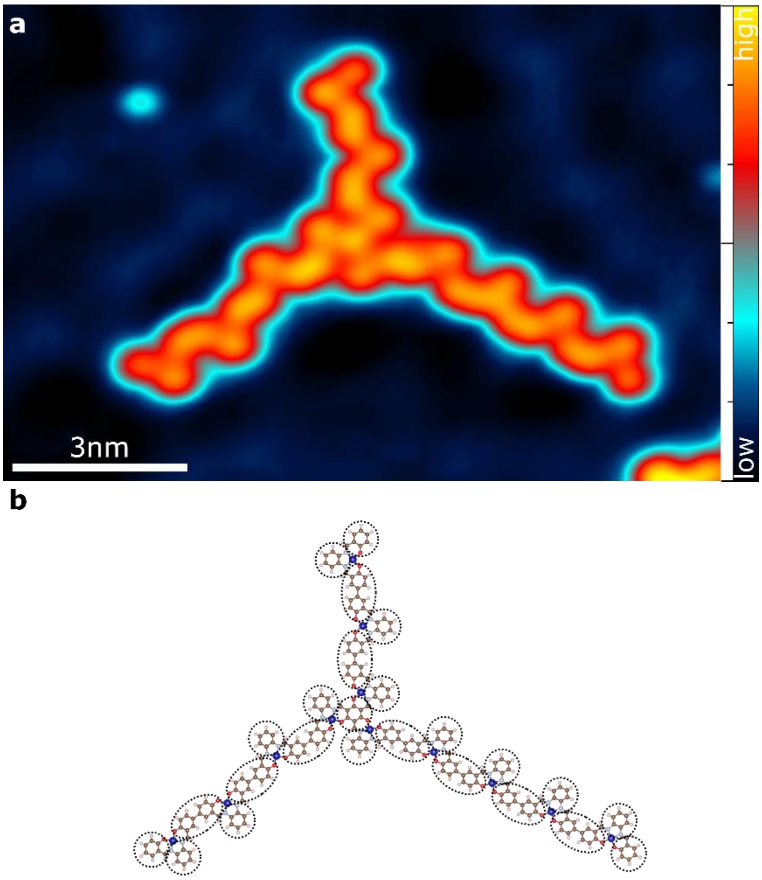

Figure 3.5 Design of a molecule-based spin logic device. The STM topography image (a) and a corresponding model representation (b). Dotted circles and ellipses in the model depict parts of molecules from which high intensities in the STM image arise. (Adapted with permission from Ref. 56. Copyright 2016 American Chemical Society.)

According to studies on different types of organic oligomers, the ones build of 5,5'-dibromosalophenatocobalt(II) molecules transfer electronic charge very inefficiently along the chain due to the interruption of conjugation by the Co atoms[75]. However, those chains were never meant to be used as electron current carriers. Density functional theory (DFT) calculations presented by DiLullo *et al.*[55] reveal an antiferromagnetic coupling between the spins localized on the Co atoms (see Fig. 3.6a). A mechanism behind that coupling is a superexchange interaction (explained in detail in the previous chapter). For such molecular chains, the strength of ferromagnetic and antiferromagnetic coupling between spin centers increases with the chain length (see graph in Fig. 3.6b).

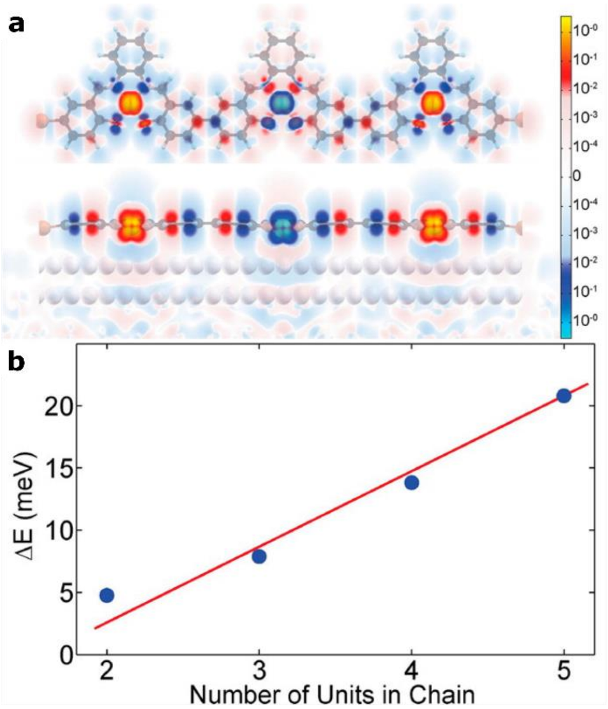

Figure 3.6 DFT calculations of magnetic interactions within the spin lead. (a) Spin density distribution in top (top) and side view (bottom). (b) Coupling energy (ΔE) as a function of mers in a spin chain. (Reprinted with permission from Ref. 55. Copyright 2012 American Chemical Society.)

Antiferromagnetic coupling between the spin chain mers was confirmed by separate calculations[56] with an exchange interaction J = - 7.9 meV, while the interactions within the junction molecule were determined to be ferromagnetic with J = + 4.6 meV. The spatial distribution of the spin densities is presented in Fig. 3.7. It visualizes how the ferromagnetic and antiferromagnetic arrangements are achieved *via* indirect superexchange interaction through neighboring C atoms.

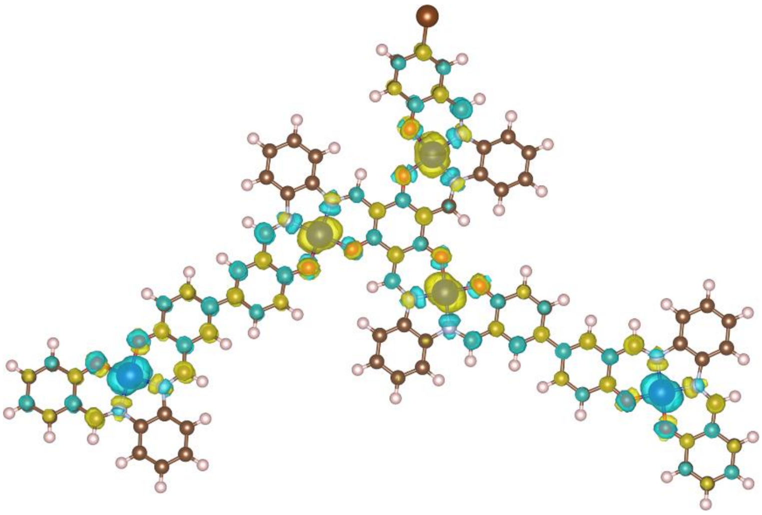

Figure 3.7 Model of the molecular structure with calculated spin densities. Blue and yellow colors represent opposite spin directions. (Reprinted with permission from Ref. 56. Copyright 2016 American Chemical Society.)

The obtained molecule based spintronic device has an advantage over the atomic spin logic device because of an order of magnitude higher exchange energy, and therefore stronger spin coupling. This, together with a rigid covalently bonded structure, promises enhanced thermal stability. Finally, this scheme relies on spin information transfer entirely within the molecular structure, therefore, it does not interfere with any other spin logic devices, unlike in the case of atomic logic devices driven by RKKY interactions (RKKY is an indirect magnetic exchange interaction mediated by conduction electrons, and thus cross-talk can be expected between spin devices or spin leads in proximity).

4 EXPERIMENTAL METHODS

This chapter provides a short introduction to scanning tunneling microscopy and its implementation. The first section focuses on the theory behind STM operation, the description of important phenomena and STM modes of operation. Next, the low-temperature ultra-high vacuum experimental setup is described, as used in my investigations.

4.1 Scanning Tunneling Microscopy

The scanning tunneling microscope (STM) was invented by Binnig and Rohrer in 1982.[76] The invention was so groundbreaking, that it earned them a Nobel prize a few years later. Its operation is based on the quantum tunneling effect. For it to take place the sample and the probe tip must be brought together to a distance below one nanometer. This is achieved by use of piezoelectric materials which expand or contract upon applying a voltage. There are a number of different STM designs *e.g.* tripod, slider, Besocke[77], or Pan[78]. A schematic of the STM the setup is presented in Fig. 4.1. The probe tip is attached to a piezoelectric tube scanner with four outer electrodes and an inner electrode allowing for x, y and z movements. The probe tip movement is achieved by combining piezo-stacks for coarse approach and the z movement of the tube scanner for very fine tip-sample distance adjustment. The x and y movements of the tube scanner are used for raster scanning of the sample plane. At a tip-surface distance of a few tenths of a nanometer, the electron wavefunctions of the probe tip and of the sample overlap. By applying a bias voltage (U) between them, a tunneling current (I), exponentially dependent on the distance, is generated. The tunneling current is then amplified and converted to a voltage by a current amplifier with a specific gain value. The signal is received by the STM electronics and, depending on the selected mode of operation, can be used to image the sample or to control the tip-sample separation by stabilizing it at a desired current set point (I_{SP}) using a feedback loop. If the latter mode is chosen, the input current is compared with the reference value and the difference is used as a measure to adjust the z position of the tip. The feedback loop consists of a comparator and an integrator characterized by their proportional gain (p) and time constant (t)

values, respectively. The comparator, based on an operational amplifier, amplifies the input signal with a magnitude defined by the p value and sums it with the set point. The new signal – proportional to the difference between them – is integrated for a time defined by the t value. The output signal is used to drive the piezo tube scanner and compensate for the difference between I and I_{SP} by increasing the tip-sample distance for $I > I_{SP}$ or decreasing it if $I < I_{SP}$. As the probe tip scans over the surface plane, a topographic map of the tip's z-positions as a function of spatial coordinates (x, y) is obtained.

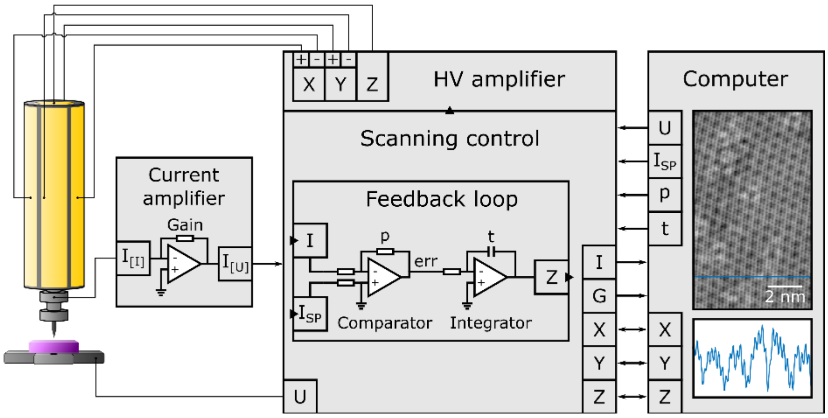

Figure 4.1 Basic STM setup. A simplified schematic with the main components of the microscope visualized: a sample, a probe tip and a piezoelectric tube scanner as well as the main electronic components. The current amplifier converts the current signal to make it less susceptible to noise. The STM electronics consists mainly of a scanning control unit and a high voltage amplifier. The former controls all the signals, handles their processing and provides communication with a computer – user input/output.

The STM electronics consists of a scanning control unit for signal processing and a high voltage amplifier for moving the probe tip in all three directions: x, y, and z. The scanning control unit communicates in full-duplex with the computer. The computer provides operation values – inputs from the user – such as bias voltage (U), current set point (I_{SP}), initial scanning coordinates (x and y) and the probe's z-distance (if the feedback loop is not used) or proportional gain (p) and time constant (t) (while the feedback loop is used). At the same time the scanning control unit delivers the output signals to store: tunneling current (I), actual position of the probe (x, y and z) and differential tunneling conductance signal (G). The computer displays the registered signals (I, z, G) as a contour intensity plot of xy-coordinates. For a quantitative analysis, a line profile can also be displayed.

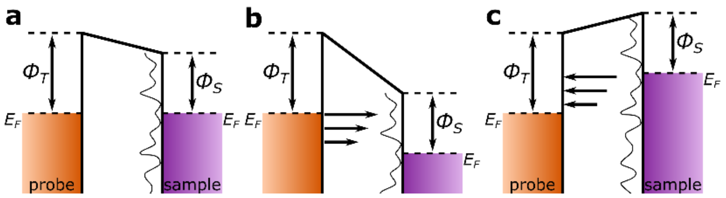

Figure 4.2 Tunneling scenarios for different bias voltages applied to the sample. (a) An equilibrium state with no bias voltage applied. (b) With a positive bias voltage applied the sample's unoccupied states are probed. (c) With a negative bias voltage applied the sample's occupied states are probed. E_F – Fermi energy, ϕ_T – probe tip work function, ϕ_S - sample work function.

In the most STM setups the probe tip is grounded and the bias voltage is applied to the sample. Fig. 4.2 presents three scenarios for different bias voltages applied. If no voltage is applied the Fermi energies of the probe tip and the sample are aligned (Fig. 4.2a). With a positive sample bias voltage, the electrons are tunneling from the occupied states of the probe tip into the unoccupied states of the sample (Fig. 4.2b). With a negative sample bias voltage applied, the electrons are tunneling in opposite direction: from the occupied states of the sample into unoccupied probe tip states (Fig. 4.2c).

4.1.1 Quantum tunneling

The STM got its name from the quantum-mechanical phenomenon stating that a particle has a non-zero probability to cross a potential barrier U_0 which is higher than the particle's energy - a situation impossible in classical physics.

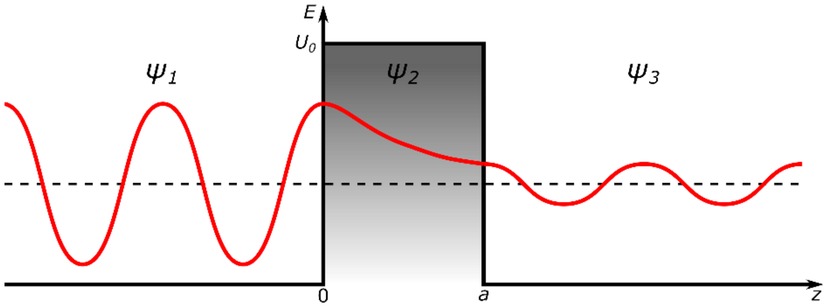

Figure 4.3 One-dimensional tunneling through a potential barrier. A propagating particle wave function Ψ_1 decays exponentially inside the potential barrier of height U_0 (Ψ_2). When the barrier width a is small enough and U_0 finite, part of the wave function is preserved after the barrier and the wave function Ψ_3 continues propagating.

In quantum physics every particle is described by a wavefunction Ψ which satisfies the one-dimensional time-independent Schrödinger equation,

$$-\frac{\hbar^2}{2m}\frac{d^2}{dz^2}\,\Psi(z) + U(z)\,\Psi(z) = E\,\Psi(z) \qquad (4.1)$$

In the situation mentioned above, and visualized in Fig. 4.3, there are effectively three areas in which such wavefunction can exist: before the potential barrier (1), inside it (2) and after crossing it (3). The solutions for Schrödinger equation in the three described areas are:

$$\Psi(z) = \begin{cases} e^{ikz} + Ae^{-ikz} & \text{for} \quad z < 0 \quad (1) \\ B_+e^{\kappa z} + B_-e^{-\kappa z} & \text{for} \quad 0 < z < a \quad (2) \\ Ce^{ikz} & \text{for} \quad z > a \quad (3) \end{cases} \qquad (4.2)$$

where $k = \frac{\sqrt{2m_eE}}{\hbar}$ is the wave vector and $\kappa = \frac{\sqrt{2m_e(U_0-E)}}{\hbar}$ is the decay constant in the barrier, *i.e.* the region forbidden in classical physics. Before encountering the potential barrier, an electron is moving as in the classical case, with a constant momentum $p = \hbar k$ or a constant velocity $v = p/m$. In the classically forbidden region (2) the wave function decays exponentially as characterized by κ. The probability density of observing an electron near a point z is proportional to $|\Psi(0)|^2e^{-2\kappa z}$, which has a non-zero value rendering the tunneling process possible. An electron can move in either positive or negative direction since part of the wave is reflected at the points of potential discontinuity. The transmission through the barrier is defined by the ratio between the probability currents of incoming and transmitted wave,

$$T = \frac{j_3}{j_1} = \frac{|A|^2}{|C|^2} = \left[\left(\frac{k^2+\kappa^2}{2k\kappa}\right)^2 sinh(\kappa z)\right]^{-1} \qquad (4.3)$$

The transmission coefficient is proportional to the experimentally observed tunneling current I. For barriers of a strongly attenuating medium, *i.e.* $\kappa z \ll 1$ (*e.g.* vacuum), Eq. 4.3 can be simplified to:

$$I \propto T \approx \frac{4k^2\kappa^2}{(k^2+\kappa^2)^2}e^{-2\kappa z} \qquad (4.4)$$

and further to:

$$I \propto e^{-2\kappa z} \qquad (4.5)$$

This result reflects the experimentally observed strong distance dependence of the tunneling current. However, it fails to address other key experimental observations, *e.g.* tunneling into localized states, *i.e.* surface states.

4.1.2 The Bardeen tunneling theory

To correctly describe electron tunneling for a real STM tunnel junction the simple 1D model described above is not sufficient. Understanding the dependency of the tunneling current on the sample's and probe tip's electronic states is of key importance. In 1961 Bardeen[79] proposed a treatment of electron tunneling based on time-dependent first-order perturbation theory. The approach, despite its simplicity, describes accurately much of the physics involved in tunneling experiments and provides quantitative agreement with experimental data.

The theory describes the tunneling junction as two weakly interacting sub-systems (probe and sample). The electron tunneling probability is determined by the overlap of the two wave functions describing probe tip and sample (Ψ_T and Ψ_S). As a consequence, the Schrödinger equation must not be solved for the system as a whole but rather individually for the two sub-systems. Inside the potential barrier wave functions can overlap and the tunneling probability is described by the tunneling matrix element

$$M_{TS} = \frac{\hbar^2}{2m_e} \iint_S \left(\Psi_T^* \nabla \Psi_S - \Psi_S^* \nabla \Psi_T\right) dS \tag{4.6}$$

The integral is taken over a surface S between the electrodes located inside the tunneling barrier. The tunneling current depends on how many occupied states of the sample Ψ_s can effectively tunnel into the unoccupied states of the probe tip Ψ_t or *vice versa*. It is given as:

$$I = \frac{4\pi e}{\hbar} \int_0^{eU} \rho_T(E_F - eU + \epsilon) \rho_S(E_F + \epsilon) |M|^2 d\epsilon \tag{4.7}$$

By making a further assumption that the magnitude of the tunneling matrix element $|M|$ does not change significantly in the energy interval of interest, *i.e.* $|M|^2 = const.$, the tunneling current is determined by a convolution of the density of states (DOS) of the probe tip and the sample:

$$I \propto \int_0^{eU} \rho_T(E_F - eU + \epsilon) \rho_S(E_F + \epsilon) d\epsilon \tag{4.8}$$

If one also assumes that the probe tip DOS does not change significantly as a function of energy, the tunneling conductance is proportional to the sample DOS:

$$G \equiv \frac{dI}{dU} \propto \rho_S(E_F + eU) \tag{4.9}$$

In a real experiment the probe tip DOS is not always constant. In general, by using a positive sample bias voltage U the tunneling current and the tunneling conductance will reflect the sample DOS. When using a negative sample bias, the two measured values are also influenced by the occupied DOS of the probe tip. Therefore, one must ensure that the probe tip DOS is flat or employ methods of normalization (see sub-section 4.1.9).

4.1.3 Tersoff-Hamann model

In the early years of the STM, Tersoff and Hamann proposed a theoretical model accounting for the non-planar probe tip geometry.[80-81] In this model the STM probe tip apex is a locally approximated by spherical potential well with radius R centered at $\overrightarrow{r_0}$, as presented in Fig. 4.4.

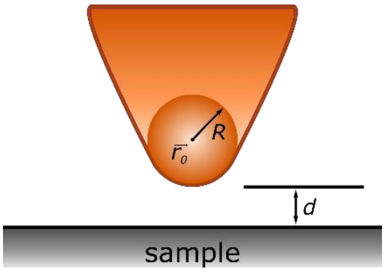

Figure 4.4 Geometry of the tunneling junction in the Tersoff-Hamann model. The probe tip apex of radius R and position r_o forms a vacuum barrier at the tip-sample separation d. Image based on Ref. 80.

Tersoff and Hamann represented the sample wave functions using Fourier series and the tip wavefunction by an *s*-type electronic state to evaluate Bardeen's tunneling matrix element. The main result of the derivation in the limit of small applied bias voltages is:

$$I \propto U\rho_S(E_F, \overrightarrow{r_0}) \tag{4.10}$$

The tunneling current is proportional to the DOS of the sample at the center of the tip's curvature. The general conclusion agrees with Eq. 4.9 from Bardeen's theory. However, the model is only valid for an *s*-wave probe tip and neglects all other probe tip wavefunctions which can be relevant for W and PtIr probe tips.

The theory is valuable for the interpretation of STM images and yields good agreement with experimental results when the feature size is around 1 nm and above. Tersoff and Hamman made an estimation of their model validity and found out that the contributions of non-spherical probe tip wavefunctions can be neglected only when the feature size is much greater than 0.3 nm. For atomic corrugations and for studies of some surface states, tip states other than s-wave states must be included.

4.1.4 Chen's derivative rule

The biggest shortcoming of the Tersoff-Hamann model, *i.e.* not including wave functions other than *s*-wave, had been addressed by Chen[82-84]. In his theory, he presented a systematic derivation of the various contributions of different probe tip states to the measured signal using a Green's function method. Chen found that the tunneling matrix elements are related to the derivatives of the sample wave functions at the tip apex atom's center $\overrightarrow{r_0}$. The results were also derived using the sum rule for both spherical and parabolic coordinate systems, which can be more convenient for STM applications. Furthermore, Chen provided an analysis of STM imaging effects caused by different tip states. The s tip state behavior coincides with the Tersoff-Hamann model. The p_z tip state leads to a corrugation amplitude enhancement by $\left(1+\frac{1}{4}q^2/\kappa^2\right)$ and the d_{z^2} tip state leads to an enhancement by $\left(1+\frac{3}{8}q^2/\kappa^2\right)^2$. In other words, for densely packed metal surfaces, an eleven-fold enhancement can be expected for a d_{z^2} tip state when compared to an s tip state.

4.1.5 Spin-polarized tunneling

All of the above considerations had assumed that all the electrons are simple charged particles. In reality, electrons have another degree of freedom (which was not included in previous sub-sections) – a spin carrying magnetic information. In a magnetic material, the exchange interaction induces a spin-splitting of the DOS, thereby lowering the spin-majority and rising the spin-minority states in energy. The first spin-sensitive STM measurements were demonstrated by Wiesendanger *et al.*[85] on alternately magnetized terraces of a Cr(001) surface separated by monoatomic steps. Since then, the method has matured and it became possible to observe magnetic structures on the atomic level.[52,86]

In a spin-polarized scanning tunneling microscope (SP-STM) the tunneling current depends on the magnitude of probe and sample polarization (P_T and P_S, respectively) and the relative orientation of their magnetization directions $\vec{m}_T$ and $\vec{m}_S$:[87-88]

$$I_{SP} \propto I_0[1 + P_T \cdot P_S \cdot cos(\vec{m}_T, \vec{m}_S)] \tag{4.11}$$

A schematic one-dimensional representation of spin-polarized tunneling is presented in Fig. 4.5. The DOS of both the sample and the probe are split into two distinct sub-states of electrons with spin-down and spin-up orientation (caused by the exchange interactions). When the magnetization directions of probe and sample are parallel (Fig. 4.5a), many electrons are able to tunnel from occupied sample spin-down states into empty probe spin-down states leading to high tunneling current, while significantly less electrons are able to tunnel from occupied sample spin-up states into empty probe spin-down states. When magnetization direction of one electrode (in this case probe) is inverted (Fig. 4.5b), the number of available probe spin-down states is significantly reduced, and therefore the corresponding tunneling current is also significantly lower. This mechanism is widely known as spin-valve effect or tunneling magnetoresistance (TMR). The resistance in the described junction is much lower in the parallel alignment.

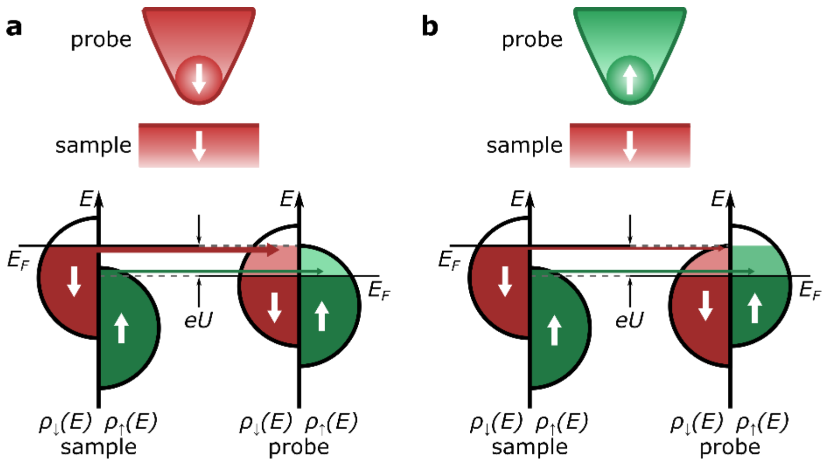
a
probe
sample
E
E
E_F
E_F
eU
$\rho_\downarrow(E)$ $\rho_\uparrow(E)$
sample
$\rho_\downarrow(E)$ $\rho_\uparrow(E)$
probe
b
probe
sample
E
E
E_F
E_F
eU
$\rho_\downarrow(E)$ $\rho_\uparrow(E)$
sample
$\rho_\downarrow(E)$ $\rho_\uparrow(E)$
probe

Figure 4.5 Schematic of spin-polarized tunneling. The DOS is presented for parallel (a) and antiparallel (b) alignment of probe and sample magnetizations. In the parallel configuration a high tunneling current is observed tunneling of spin-down electrons mainly. In the antiparallel configuration the spin-down electron tunneling channel is drastically reduced. Image based on Ref. 88.

The spin polarization is defined as the difference of spin-up ($\rho_\uparrow$) and spin-down ($\rho_\downarrow$) states divided by the sum:

$$P = \frac{\rho_\uparrow - \rho_\downarrow}{\rho_\uparrow + \rho_\downarrow} \tag{4.12}$$

According to Bardeen's theory (sub-section 4.1.2), the tunneling conductance is proportional to the sample DOS. By taking the tip DOS additionally into account, Heinze *et al.*[89-90] derived an expression for the conductance of a magnetic STM junction:

$$G \equiv \frac{dI}{dU} \propto \rho_T \cdot \rho_S(E_F + eU) \cdot [1 + P_T \cdot P_S(E_F + eU) \cdot cos(\vec{m}_T, \vec{m}_S)] \tag{4.13}$$

The differential conductance signals in the case of parallel and antiparallel magnetization directions of both electrodes can be used to calculate a spin asymmetry of the tunnel junction and gain information about its spatial and energy dependence. It is defined as:

$$A(U) = \frac{\frac{dI(U)}{dU}_{\downarrow\downarrow} - \frac{dI(U)}{dU}_{\downarrow\uparrow}}{\frac{dI(U)}{dU}_{\downarrow\downarrow} + \frac{dI(U)}{dU}_{\downarrow\uparrow}} \tag{4.14}$$

The spin asymmetry should be derived from STS measurements performed at constant tip-sample separation, otherwise corrections are necessary in order to extract useful information.

4.1.6 Elastic tunneling to molecules

When considering tunneling to a molecule adsorbed on a surface, two different mechanisms should be distinguished[91]: first, a multi-step tunneling process involving electron tunneling in two stages: from the probe tip to the molecule and subsequently to the substrate. Second, a direct tunneling from the tip into the substrate with a modified tunneling barrier due to the presence of the molecule, *i.e.* the molecule effectively changes the dielectric constant and lowers the tunneling barrier. Both of these cases are presented in the work of Repp *et al.*[42] from which the Fig. 4.6 is taken. There one can see the STM images involving two molecular states at negative and positive sample bias which resemble the distributions of the molecule's HOMO and LUMO states, respectively, and a comparison with DFT calculations. For a multi-step tunneling process to occur, the energy of the electrons must be equal or higher than that of a molecular state. On the other hand, when tunneling within the HOMO-LUMO gap, the STM image of the molecule resembles the modification of the effective tunnel barrier by the presence of the molecule.

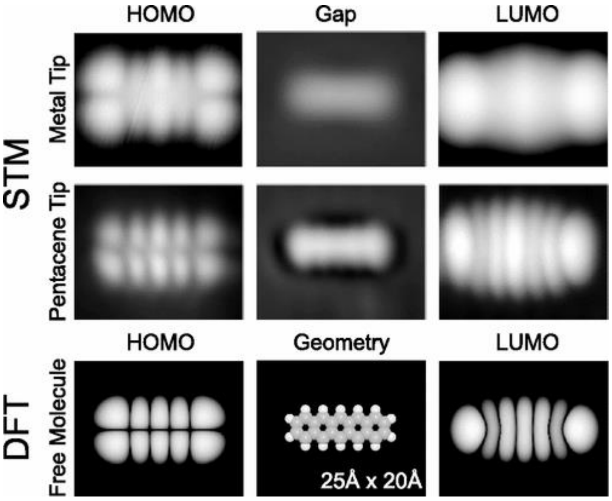

Figure 4.6 Example of tunneling in the presence of a molecule. Multi-step tunneling occurs for the left and right columns, while single-step tunneling is presented in the middle one. The images presented in the top row are acquired using a metal probe, the ones in the middle row using a molecule (pentacene) terminated probe. In the bottom row DFT calculations are presented for a free molecule. (Reproduced with permission from Ref. 42. Copyright 2005 American Physical Society.)

Multi-step tunneling only occurs when the molecule is electronically partially decoupled from the metallic substrate. The lifetime of an electron or a hole in the molecule must be sufficiently long before it tunnels further into the substrate. For example, a NaCl multilayer can be used to decouple molecules from the substrate. In this case, the lifetime of an electron/hole increases with the number of NaCl layers. Decoupling can also be achieved by other materials such as hexagonal boron nitride[43] or graphene[92].

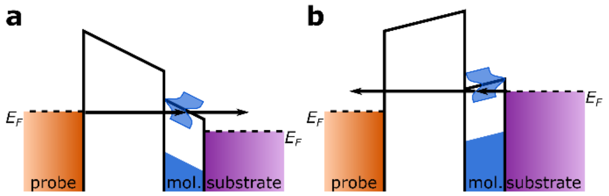

Figure 4.7 Schematics of multi-step tunneling *via* molecular states. (a) With a positive bias voltage applied (to the substrate) electrons are tunneling from the probe through a molecular state to the substrate, (b) with a negative bias voltage applied electrons are tunneling from the substrate through a molecular state to the probe. Image based on Ref. 93.

A schematic picture of a two-step tunneling process is presented in Fig. 4.7. While probing the unoccupied sample states (Fig. 4.7a), electrons tunnel from the probe tip to a molecular state and subsequently into the substrate. While probing the occupied sample states (Fig. 4.7b), electrons tunnel from the substrate to a molecular state and subsequently into the probe tip. Despite many attempts to derive a master equation for this phenomenon a clear and straightforward approach is yet to be formulated.[93] The ones derived till now are based on many assumptions which limit their applicability.

4.1.7 Lock-in amplifier

In the theoretical discussion presented in previous sub-sections it was shown, that the measured tunneling current is always integrated over states from the Fermi energy (E_F) up to the energy set by the applied bias voltage (eU). In order to probe the DOS at a specific energy one needs to measure the differential tunneling conductance G. This can be easily achieved by measuring the derivative of the tunneling current at a specific energy using a lock-in amplifier.

A lock-in amplifier is a frequency and phase sensitive device which is able to extract and amplify the signal of a known reference carrier wave, virtually without any loss.[94] It is very useful in cases when the signal is lower than the base noise level. In some situations (depending on the dynamic reserve of the instrument and the quality of the reference signal) it can detect signals being many thousand times smaller than the noise level. The input signal is multiplied by the reference signal and integrated over a specified time interval. As a result, any signal with a different frequency or phase shift is strongly attenuated and the output signal is solely corresponding to the one carried by the modulation signal. In STM applications, however, a lock-in amplifier is not only used as a signal recovery device. Since the dependence of the tunneling current I on the bias voltage U is not linear (see graph in Fig. 4.8), the output is proportional to the derivative of the tunneling current with respect to the bias voltage. By pre-adjusting the phase difference to 0° one can extract the dI/dU signal, in other words, the differential tunneling conductance G. A phase difference set to 90°, on the other hand, provides a quadratic signal which is proportional to the tunneling junction's capacitance. In modern lock-in amplifiers both can be extracted simultaneously. Additionally, by using a second harmonic of the modulation signal for demodulation, the output signal will be proportional to the second derivative d^2I/dU^2, which provides information about inelastic electron tunneling processes.

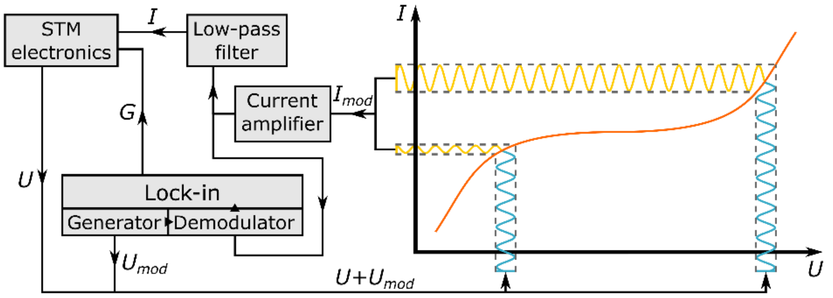

Figure 4.8 Lock-in technique working principle. Block diagram with all the main components and a plot schematically showing the signal extraction from the $I(U)$ curve. The bias voltage U set by the STM electronics is modulated with a high-frequency voltage U_{mod} coming from the generator. The obtained current signal I_{mod} is split into two parts: one portion travels through the low-pas filter to remove the AC part, while the other goes to the Lock-in demodulator unit. The STM electronics obtains two signals, the tunneling current and its derivative, at the same time.

The integration of a lock-in amplifier into the STM setup is presented in Fig. 4.8. Initially the bias voltage U from the STM electronics (DC) is summed with an alternating modulation voltage U_{mod} supplied by the lock-in amplifier's generator unit (AC). The modulation signal is of small amplitude U_{mod} (typically 100 µV ÷ 100 mV) and high frequency f_{mod} (typically 1kHz ÷ 50kHz). The summed AC/DC voltage is applied to the STM tunneling junction. The measured tunneling current signal I_{mod} is affected by the AC part of the bias voltage signal, thus carrying the information about the modulation. The signal is then processed twofold: (1) by going through a low-pass filter and entering the STM electronics as standard tunneling current signal I; (2) in the lock-in amplifier unit using the reference signal from the generator as described before. The measured signal is effectively integrated in the lock-in amplifier in the limits set by U_{mod}. Hence, by varying this amplitude one can determine the range of integration. Lowering it will cause the obtained signal to be more energy specific (less averaging), but it will cause the signal intensity to decrease. The obtained differential tunneling conductance signal G is sent to the STM electronics and registered there. The lock-in technique is used for two of the modes described next, *i.e.* the spectroscopy mode and the differential tunneling conductance mapping.

4.1.8 Modes of operation

Any STM can be employed in a variety of modes of operation. The main modes are used to visualize the sample's approximated topography, to perform the point spectroscopy registering the bias-dependence of the current and its derivative(s) or to visualize the spatial distribution of the local density of states (LDOS) by differential conductance mapping. In the raster scanning modes the direction along the scanning line (x) is called fast-scan direction, while the perpendicular one (y) is called slow-scan direction.

Constant-height mode

The simplest mode of STM operation is the constant-height mode, where the tip is held at a constant height z during scanning, while recording the tunneling current (Fig. 4.9). For this mode the measurement conditions have to be properly set in order to prevent tip and sample from contacting. One has to make sure that the temperature of the STM is constant and stable, the local slope of the sample is electronically corrected and the scanning area is close to the center to avoid scanner non-linearity and creep effects.

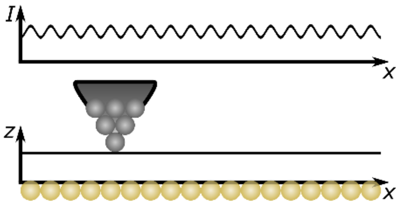

Figure 4.9 Constant-height mode of STM operation. Schematics of a line scan profile over an atomically flat surface. The z position stays constant while I is recorded reflecting the atomic surface corrugation.

Here, the tunneling current I is recorded as a function of lateral probe tip position (x, y). There are two main advantages of this mode. First, the scanning speed can be much higher compared to the constant-current mode (described next). Second, the signal directly reflects the sample's LDOS which allows for a direct comparison with results of first principles calculations (*e.g.* DFT). The disadvantage is that it can only be used on smooth surfaces. Even when applied to planar adsorbed molecules it can prove to be difficult. The exponential distance dependence of the tunneling current can result in very high currents over the molecule or, when the distance is adjusted accordingly, very small currents over the substrate surface.

Constant-current mode

In the constant-current mode, the tip – sample separation is governed by the feedback loop. It makes it the easiest to use, and thus the most popular mode of STM operation. Based on the exponential distance dependence of the tunneling current (Eq. 4.5) the feedback loop allows the tip to follow the surface contours with great accuracy. A schematics of a line scan obtained in this mode is presented in Fig. 4.10.

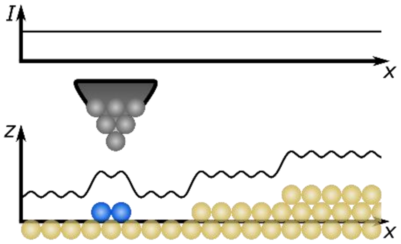

Figure 4.10 Constant-current mode of STM operation. Schematics of a line scan over a surface with monoatomic steps and an adsorbate (blue). The feedback loop keeps the tunneling current I constant by adjusting the tip position z during scanning. As a result, a topographic map $z(x, y)$ is obtained

The feedback loop responds to very small variations in the tunneling current by approaching the tip closer to the sample when the tunneling current drops, or withdrawing away from the sample when the tunneling current rises. The tip position z is recorded as a function of its lateral position (x, y). The advantage of this mode is the possibility to scan on non-planar surfaces with a high corrugation. However, the use of a feedback loop makes the scanning process much slower compared to the constant height mode. Though this mode is often referred to as topography mode, sometimes it does not reflect the true sample's topography, as the tunneling current depends on the tip-sample separation as well as on the electronic properties of both electrodes.

Spectroscopy mode

In this mode of STM operation the tip is placed above a position of interest based on previously obtained topography map. The tip's z position is defined by the applied bias voltage (U_{stab}) and the setpoint current (I_{stab}). Next, the feedback loop is switched off to stabilize the tip's position at a constant height and the bias voltage is swept over the desired range. While the bias voltage changes, the response of the tunneling current $I(U)$ is registered. By using the lock-in technique it is also possible to record the tunneling current derivative $\mathrm{d}I(U)/\mathrm{d}U$ or the second derivative $\mathrm{d}^2I(U)/\mathrm{d}U^2$. The derivative could, in principle, be calculated numerically from the $I(U)$ curve after the experiment. However, using the lock-in provides significantly higher signal-to-noise ratio (discussed in more detail in sub-section 4.1.7). This mode is often referred to as scanning tunneling spectroscopy (STS).

While performing STS measurements on systems expected to be spin-polarized one has to remember that the tip height for the two spin channels will differ in constant-current mode (see the discussion in sub-section 4.1.6). At the same time the evaluation of the SP-STS data relies on a comparison of the $I(U)$ curves obtained for the two spin-channels at constant tip-sample separation.[95] Therefore, to assure identical tip height in SP-STM studies, one of the following approaches must be adopted: (1) the tip has to be stabilized at a specific bias voltage at which the magnitude of spin polarization for both channels is equal; or (2) the tip has to be stabilized at a position not exhibiting magnetic properties and moved to the area of interest with predefined height after the feedback loop is switched off. The latter approach had been used in experiments presented in Chapter 6.

Differential tunneling conductance mapping

By combining the high spatial resolution of the STM in the raster scanning mode and the high energy resolution of the spectroscopy mode, it is possible to obtain the spatial distribution of electronic states at a given energy. It is essential for this mode of operation to use the lock-in technique in order to obtain energy selectivity. The differential tunneling conductance map (also called $\mathrm{d}I/\mathrm{d}U$ map) provides information about the LDOS distribution at the chosen bias voltage and the height of the scanning tip. The map can be obtained together with topography images in either constant-current or constant-height mode, both with their drawbacks. One of them is directly linked to the limited scanning speed in of the conductance mapping mode. This limitation is caused by the dependence of scanning speed on the lock-in settings: the time constant and the frequency. Moreover, if the map is obtained in constant-current mode, the plane of the scanning tip is determined by the DOS from the Fermi energy to the energy corresponding to the applied bias voltage of the measured sample and it does not resemble the LDOS in full. By recording the conductance maps in very small energy steps one can visualize the spatial distribution of the spectroscopy curves described previously.

4.1.9 Normalization

In the previous sections it has been pointed out that in the measured tunneling current signal is not always solely dependent on the sample DOS, as the tip DOS is not always constant. In order to extract the sample DOS and rule out unwanted tip effects, various approaches have been proposed by different groups over the years. Those yielding best results, and thus being widely used, are presented in this chapter. It is important to note that no normalization technique is universally applicable. Their usefulness varies for the different types of experiments one can perform with the STM. Moreover, none of the normalization techniques to date provides quantitative results and should be used only to highlight qualitative effects.

Feenstra parameter

In the sub-section 4.1.2 the assumption was made that the tunneling matrix M does not change significantly in the energy interval of interest. However, that is only true for very small bias voltage intervals. In real experiments where the energy scale can be as large as ±2 eV, the energy dependence cannot be ignored. Though the differential tunneling conductance does highlight some of the DOS features, its exponential divergence at higher energies masks the rest of the DOS features. In order to compensate for these divergences, a very simple normalization had been proposed by Feenstra *et. al.*[96] It introduces a parameter, the normalized tunneling conductance:

$$g_N = \frac{dI/dU}{I/U} \tag{4.15}$$

The so-called Feenstra parameter g_N is a dimensionless quantity. In essence it is the differential tunneling conductance divided by the total conductance of the tunnel junction. The approach is motivated by the fact that the energy dependence of the tunneling matrix element influences $\mathrm{d}I/\mathrm{d}U$ and I/U similarly. Hence, in the Feenstra parameter matrix element effects are canceled out. Therefore, it provides a cleaner spectrum in which the DOS features are more clearly visible.

Marching method

This method aims at deconvoluting the tip DOS from the tunneling spectra. The approach has been presented by Chen[84] and is based on the use of the second kind

Volterra equations[97] to extract the DOS of the tip from the STS data. The best results are obtained when using the Feenstra parameter in advance. The method provides a way of determining the nature of the tip apex and, more importantly, allows for subtracting the tip DOS from the measured differential tunneling conductance data.

Comparative scanning tunneling spectroscopy method

As mentioned in sub-section 4.1.2, the tunneling current and the tunneling conductance are predominantly proportional to the sample's DOS at positive bias voltages, but contain effects of the tip DOS at negative bias voltages. For sample DOS recovery, the comparative scanning tunneling spectroscopy method was proposed by Ukraintsev[98]. This method is based on a differential tunneling conductance normalization by fitting the differential conductance to the tunneling probability function. The method does not use unconstrained parameters and provides the best DOS deconvolution as claimed by the author. The key ingredient of this approach is the use of an asymmetric tunneling probability function which accounts for the inadequate fitting of the DOS using Bardeen's tunneling theory when the sample's Fermi level is located inside the band gap.

Tunneling current compensation method

While taking several STS curves of the same type of feature at different locations of interest, the registered tunneling current may differ slightly (*e.g.* due to probe tip drift or creep). To compensate for those differences an approach had been proposed by Yayon *et al.*[99] This normalization method is based on choosing one spectrum remaining unchanged and calculating a normalization for the other ones by multiplying them by the quotient of the tunneling current of the unchanged spectrum and the tunneling current of the normalized spectrum.

$$\left(\frac{dI}{dU}\right)_{norm} = \left(\frac{dI}{dU}\right)_{const} \frac{I(U)_{const}}{I(U)_{norm}} \tag{4.16}$$

After this procedure, the resulting spectra can be compared with one another provided they are addressing the same type of feature on the sample.

Constant-current dI/dU map normalization

A natural way to avoid topographic effects is to obtain the differential tunneling conductance maps in constant-height mode. However, for reasons described in the previous sub-section this is not always possible. While obtaining the differential tunneling conductance maps in constant-current mode the topography is simultaneously recorded. It means that the map is affected by the feedback loop which constantly compensates for the changes in tunneling current by changing the tip height. As a consequence, the tip does not move on a plane. Li *et al.*[100] presented a way to recover the real contours of the measured LDOS by using the tip height change extracted from the topography maps to normalize the differential conductance map using the following formula:

$$LDOS = \frac{G}{exp\left[-z\sqrt{\frac{4m}{\hbar^2}(\phi_T+\phi_S+eV-2E)}\right]} \tag{4.17}$$

As the study presented in Chapter 6 does not focus on low energies close to the Fermi level but rather on molecular orbitals and corresponding DOS features in a wide energy region, the most suitable and straightforward way to normalize the obtained STS curves was the use of the Feenstra parameter method

4.2 Experimental setup

All experiments were performed in an experimental setup providing ultra-high vacuum (UHV) conditions and cryogenic temperatures of $T \approx 6.5$ K. In this section a short overview of that system is provided. It includes a description of the base system and its different parts along with all modifications which were necessary for successful experiments.

4.2.1 Low-Temperature UHV System

The original version of the ultra-high vacuum (UHV) system[101] had been used to study and characterize III-V semiconductor samples. Later it had been updated with *e.g.* evaporators to study metallic thin films and single molecules adsorbed on them.[102] For the studies presented in this dissertation the setup needed to be further updated and improved (details in the next sub-section).

The whole system was built up on a separate foundation which decouples it from the vibrations of the building. The foundation has a pit which is big enough to accommodate a specially designed table supporting the cryostat – the main component of the system. It is situated partially above the floor level and partially in the pit (see Fig. 4.11). The cryostat is surrounded by quartz sand while the table is supported by pneumatic legs. Both, the sand and the pneumatic legs, are parts of a multi-stage damping system to provide optimum isolation from the environment. The cryostat contains a tank holding up ~ 90 l of liquid helium (LHe) surrounded by a superinsulation shield instead of a widely used liquid nitrogen (LN_2) one. This solution provides means of avoiding additional vibrations coming from LN_2 boil off. The overall cryostat design allows maintaining its operational temperature for 48 to 72 hours (depending on the number of transfers and/or magnetic field sweeps). Inside the LHe bath resides the UHV insert. It is separated from the LHe by a double wall. The space in between is used to introduce a thermal coupling medium - He gas. The He exchange gas can be introduced at different pressures, thereby varying the cooling rate. However, the higher the exchange gas pressure the stronger the unwanted mechanical coupling to the He bath *via* the receptacle of conical frustum (which is directly connected with the STM while in operational position).

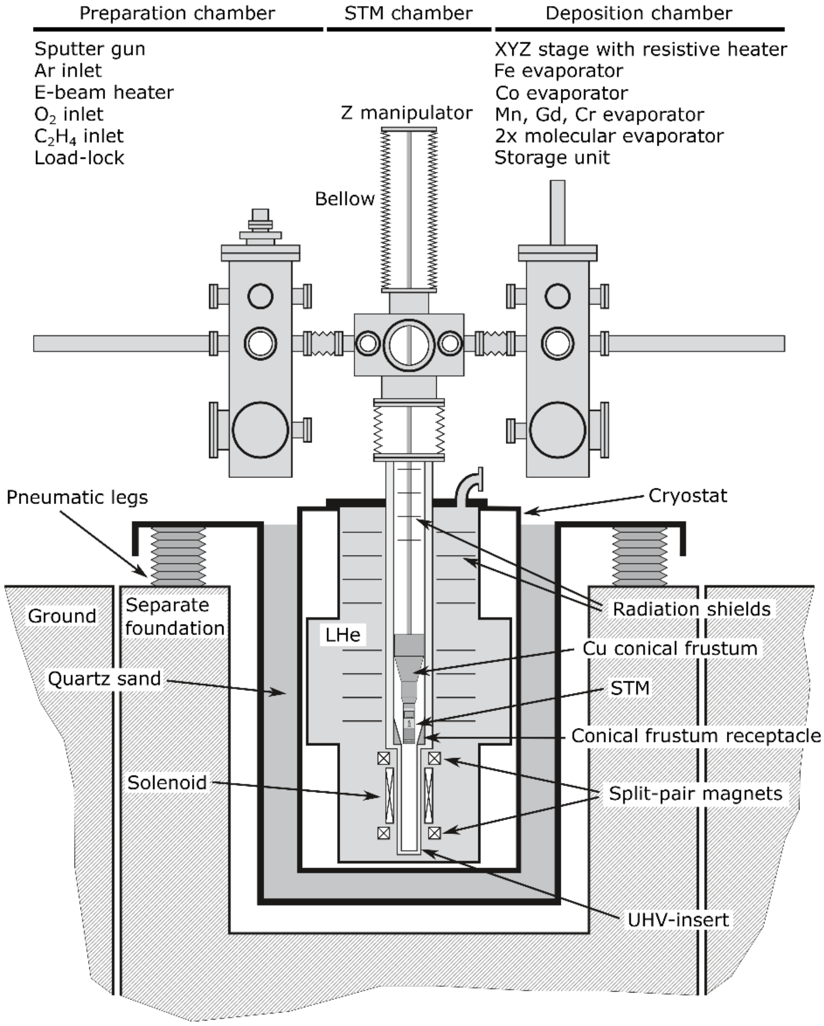
Preparation chamber
STM chamber
Deposition chamber
Sputter gun
Ar inlet
E-beam heater
O_2 inlet
C_2H_4 inlet
Load-lock
Z manipulator
XYZ stage with resistive heater
Fe evaporator
Co evaporator
Mn, Gd, Cr evaporator
2x molecular evaporator
Storage unit
Bellow
Pneumatic legs
Cryostat
Ground
Separate foundation
LHe
Radiation shields
Cu conical frustum
Quartz sand
STM
Conical frustum receptacle
Solenoid
Split-pair magnets
UHV-insert

Figure 4.11 Side view schematics of the UHV system with cryostat part in cross-section. All the important parts are labelled or listed. Image based on Ref. 101.

The system is equipped with two superconducting magnets. They provide a magnetic field along two axes: normal to the sample plane (z-direction) and parallel to it (x-direction). In the z-direction the solenoid magnet generates a magnetic field of up to $B = 6.25$ T and in the x-direction the split pair magnet generates a magnetic field of up to $B = 2$ T. The two can operate simultaneously generating a magnetic vector field of up to $B = 1$ T in the zx-plane.

Above the cryostat there are three UHV chambers mounted along the preparation/transfer-axis. Each of them serves a different purpose and is essential for the operation of this system. A top view sketch with all essential components is provided in Fig. 4.12. The preparation chamber is used for the preparation of samples and tips, *e.g.* by sputtering, high temperature annealing, annealing in oxygen atmosphere and for graphene growth. It has a sputter gun with its Ar gas inlet, an e-beam heating stage, an O_2 gas inlet, ethylene (C_2H_4) gas inlet and a load-lock sub-chamber for sample transfer. The chamber is equipped with a pumping system consisting of an ion-getter pump, a titanium-sublimation pump (with an additional shield increasing the active surface area) and a turbomolecular pump which is used during sample preparation. The base pressure is at the level of p = 1E-10 mbar. A wobble stick manipulator provides the possibility to transfer the sample *in vacuo* from a linear and rotary manipulator to the e-beam heating stage. The linear and rotary manipulator is also used to transfer samples from the preparation chamber to the STM chamber. It can additionally store up to three different samples or tips.

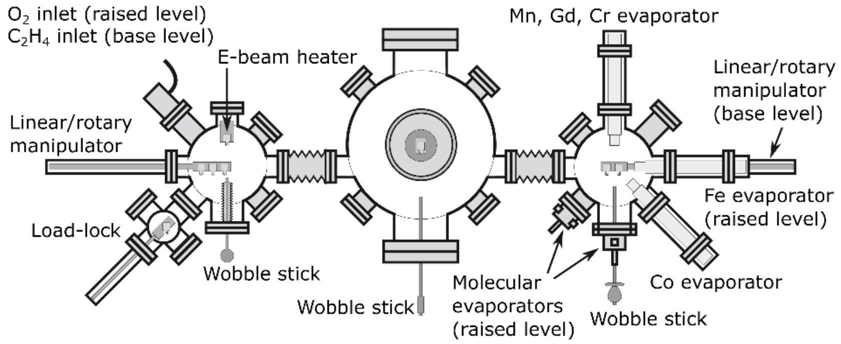
O_2 inlet (raised level)
C_2H_4 inlet (base level)
E-beam heater
Linear/rotary manipulator
Load-lock
Wobble stick
Wobble stick
Mn, Gd, Cr evaporator
Linear/rotary manipulator (base level)
Fe evaporator (raised level)
Molecular evaporators (raised level)
Co evaporator
Wobble stick

Figure 4.12 Top view schematics of the UHV system. All the important parts are labelled. Image based on Ref. 101.

The deposition chamber is used for the evaporation of various elements and molecules onto previously prepared samples or tips, transferred from preparation chamber. It has a XYZα stage with resistive heater for bringing the sample to desired locations within the chamber and for offering the possibility of raising the substrate's temperature during deposition. The sources available in the chamber are: an e-beam Fe evaporator, an e-beam Co evaporator, a triple-cell e-beam evaporator containing Mn, Gd and Cr and two custom-made triple-cell molecular evaporators (their description is provided in the next sub-section). The chamber is equipped with a pumping system consisting of an ion-getter pump and a titanium-sublimation pump. There is a possibility of connecting this chamber to the turbomolecular pump using a bypass. The base pressure is at the level of p = 1E-10 mbar. A rotatable wobble stick manipulator provides the possibility to transfer the sample *in vacuo* from a linear and rotary manipulator into the XYZα stage. The linear and rotary manipulator is used to transfer samples from the deposition chamber to the STM chamber. It can additionally store up to two different samples or tips. This chamber also has a storage unit which can store up to six different samples or tips.

The STM chamber has a dual role. It allows the transfer of samples from the preparation chamber to the deposition chamber. More importantly, it provides a means of transferring the sample to the STM. UHV conditions are provided by an ion-getter pump, a titanium-sublimation pump (with additional shield to increase the active surface area) and a non-evaporable getter (NEG) pump which is extremely efficient for pumping hydrogen. The base pressure in this chamber is below 1E-10 mbar. A rotatable and precise wobble stick is used here for *in vacuo* handling of the sample. The STM microscope is mounted on a manipulator moving along the z-axis with a maximum extension of 1400 mm. At its upper position easy access for the transfer of a sample in and out of the STM is provided. During this process the temperature of the previously cooled insert remains below 45 K. The temperature is measured on the top of a copper cone frustum. At the lowest position of the manipulator the cone frustum firmly fits into its receptacle providing a way of cooling down the STM to T ≈ 6.5 K. The process takes from 3 to 4 hours.

The STM head used in this system is a home built one. Its original design is by Pan[78] with further improvements made in successive years[103]. The main features are its simplicity and rigidity making it insensitive to mechanical vibrations while providing a way for an *in-situ* tip exchange. A photo of the STM is presented in Fig. 4.13. The microscope body (1) is made of gold-plated phosphorus bronze, an alloy which is hard, nonmagnetic and UHV-compatible. A macor plug (2) provides a means for a quick exchange of the head as it encloses all electrical connections. The tip exchange is made possible by using a so-called walker motor which allows for a movement of the assembly of the tip with its holder (3) and a tube scanner (4) being enclosed in a sapphire prism (5). The walker motor consists of six piezoelectric stacks clamping the sapphire prism by using a spring plate (6). The movement in stick-slip mode is induced by applying a high voltage sawtooth waveform to the stacks (7).[104] At the base temperature the tube scanner can provide a maximum scan range area of 3 x 3 µm^2 and a z-range of maximum 500 nm.

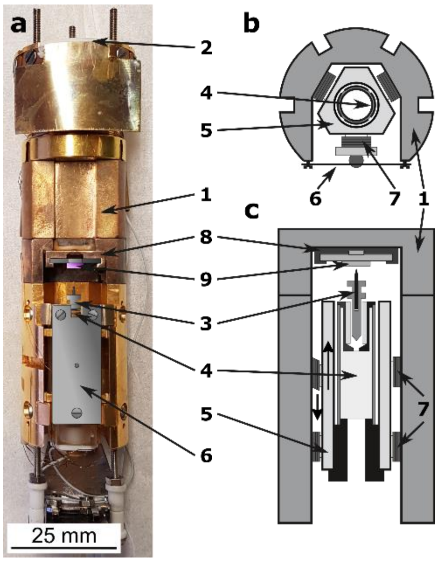

Figure 4.13 Design of the STM. A photo along with a top view and cross section schematics showing all key components marked with numbers: (1) STM body, (2) macor plug with electrical connections, (3) tip holder with a tip, (4) tube scanner, (5) sapphire prism, (6) spring plate, (7) walker stack, (8) sample stage, (9) sample. Image based on Ref. 103.

4.2.2 Modifications

Performing measurements on the sample of interest proved to be challenging while using the original system setup. The main problems were connected to the experimental setup's high susceptibility to audio noise and the necessity to use very low tunneling currents due to the molecule's low interaction with the substrate.

Measurement room

The setup of the system, mainly its long vertical manipulator, plus insert, works as an acoustic antenna for any movement, speech or artificial sound. In order to minimize the possibility of such interference it was necessary to move the measurement equipment (electronics and computer station) to a separate room. The room is located directly above the laboratory. Moving all possible electronic components outside the laboratory also resulted in a lower heat output, therefore, minimizing thermal fluctuations inside the room. Additionally, part of the electronics which needs to be close to the UHV system (including the magnet power supply) was enclosed in a server grade silenced rack for better acoustic isolation.

Current amplifier

For the studied sample system of molecules adsorbed on graphene very low tunneling currents had to be used in order to avoid electric field induced movement of molecules. The Femto DLPCA-200 current amplifier is a very powerful and versatile device allowing most of the standard STM experiments. However, at the low current level which is needed for the experiments of this dissertation, the signal-to-noise ratio is not acceptable. To improve it the Femto LCA-1K-5G current amplifier was incorporated into the experimental setup. A comparison of the two amplifiers is presented in Tab. 4.1. The main advantages of the LCA-1K-5G are the fivefold higher gain with a lower input noise. This provides a significant increase in signal-to-noise ratio of the recorded signal. The only drawbacks are a lower upper cut-off frequency with a higher rise-/fall-time and a maximum tunneling current of 2 nA. However, these are not important for the present experiments.

Table 4.1 Comparison of the amplifiers' main features (old and new).

	DLPCA-200*	LCA-1K-5G
Transimpedance (gain)	$1 \cdot 10^9 \frac{V}{A}$	$5 \cdot 10^9 \frac{V}{A}$
Input noise current density	$4.3 \frac{fA}{\sqrt{Hz}}$	$3 \frac{fA}{\sqrt{Hz}}$
Upper cut-off frequency	$1.1\ kHz\ (-3\ dB)$	$1\ kHz\ (-3\ dB)$
Rise-/Fall-time	$300\ \mu s$	$400\ \mu s$
Max input current	$\pm 10\ nA$	$\pm 2\ nA$

*DLPCA at low noise 10^9 setting

Lock-in amplifier

The amplifier unit formerly used in this setup was a Stanford Research Systems SR830. However, it needed to be upgraded in order to obtain the best possible differential conductance signal at low tunneling currents. The amplifier of choice is a Zurich Instruments MFLI 500kHz unit. A comparison of the two is presented in Tab. 4.2 which summarizes the main advantages of the new amplifier.

Table 4.2 Comparison of the lock-in amplifiers' main features (old and new).

	SR830	MFLI
Frequency range	$1mHz - 102.4\,kHz$	$0 - 500\,kHz$
Frequency resolution	$0.1\,mHz$	$1\,uHz$
Amplitude	$0.004^{*} - 5\,V_{rms}$ $(\approx 130\,mV_{pk-pk})$	$0 - 200\,mV_{pk-pk}$
Dynamic reserve	$> 100\,dB$	$120\,dB$
Phase resolution	$0.01\,deg$	$0.00001\,deg$
Time constants	$10\,us - 30\,ks$	$336\,ns - 83\,s$
Roll-off	$6, 12, 18, 24\ \frac{dB}{oct}$	$6, 12, 18, 24, 30, 36, 42, 48$
A/D inputs	$16\,bit$	$16\,bit$
Input full range sensitivity	$\pm 5\,V$	$\pm 3\,V$
Input noise**	$130\ \frac{fA}{\sqrt{Hz}}$	$20\ \frac{fA}{\sqrt{Hz}}$
D/A outputs	$16\,bit, \pm 10\,V$	$18\,bit, \pm 10\,V$
Number of oscillators/demodulators	$1/1$	4^{***}
Other features		Fully remote control Internal signal mixer Oscilloscope Signal analyzer

* modulation cannot be switched off
** for settings used
*** can be combined in different configurations

The main outstanding features having great impact on the measurement conditions are as follows: the modulation amplitude range is now bigger, but most importantly, the modulation can now be completely switched off. The signal outside of a set frequency can be attenuated with a roll-off slope of up to 48 dB per octave. The output digital-analog converter features 18-bit resolution. The new lock-in amplifier has 4 internal channels which can be set up by the user to be employed as oscillators or demodulators. This provides the possibility for different configurations: modulation with one frequency and demodulation with three different time constants or simultaneous modulation/demodulation with two separate frequencies.

Very important for the current laboratory setup was a full remote-control possibility. The amplifier is fully controlled using a web server-based software accessed by the computer's internet browser. The software allows for mixing the signals internally and features internal oscilloscope and signal analyzer. The latter two let us resign from using an external oscilloscope unit as well.

STM electronics

One of the main drawbacks of the formerly used STM control electronics (Createc) was a lack of full tip control. The default position of the tip could be set to only three places: upper-left corner, middle top or center of the currently chosen scanning area. Needless to say, there was no possibility to freely manipulate the position of the tip, a feature which is invaluable while performing STS experiments on a complex substrate, like the one studied in this dissertation. Another shortcoming has been the limitation to change the offset for the x, y and z scanning directions only locally using knobs directly on the high-voltage amplifier.

The decision to switch to a new control electronics (Nanonis) came with numerous benefits in addition to fixing the above-mentioned problems. The Nanonis system provides a full remote-control possibility *via* a computer-based interface. Moreover, any setting can be changed and adjusted separately at any time, including the x, y and z position of the tip. The software provides the possibility for further improvements and expansion *via* a programming interface. Any extension of the Nanonis software can be prepared based on the LabVIEW programming platform. Hardware-wise, the new real time controller v5 (RC5) provides a slightly better performance with higher analog signal sampling of 500 kHz (compared to 250 kHz). The innovative hrDAC feature can also increase the output signal resolution to 22 bit. The high-voltage amplifier (HVA4) is more stable than the one from Createc and provides a lower base noise level. The modular structure of the Nanonis system also provides an integrated high-frequency high-voltage ramp generator (PMD4) for coarse approach, automated *via* software or operated manually *via* remote, avoiding the need for auxiliary generator (PMC 100 from RHK).

Molecular evaporator

A custom-made triple cell molecular evaporator was used for generating a pure beam of molecules. It allows for precise control of deposition rate with temperature feedback on each molecular source. A photo of the evaporator is presented in Fig. 4.14.

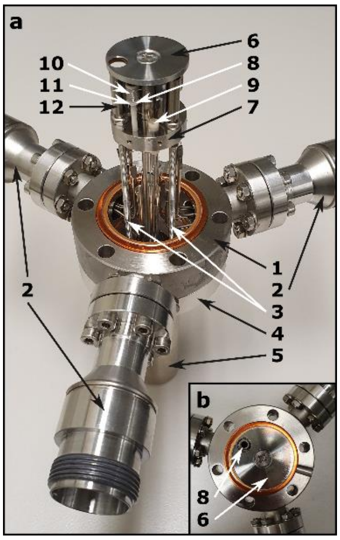

Figure 4.14 Molecular evaporator. (a) side and (b) top view of one of the crucibles. All components are marked with numbers: (1) CF40 double-sided flange with three radial CF16 ports, (2) feedthroughs, (3) tapped rods, (4) reducer flange, (5) rotational feedthrough, (6) shutter, (7) head plate, (8) crucible, (9) ceramic passthrough, (10) heater, (11) thermocouple, (12) radiation shield.

The evaporator is built on a CF40 double-sided flange with three radial CF16 ports (1) hosting four-pins feedthroughs (2). The head of the evaporator is mounted on 3 tapped rods (3) which are mounted on a zero-length CF40/CF16 reducer flange (4). A rotational feedthrough (5) is attached to that flange. The rotational feedthrough goes through the assembly in the middle all the way to the top where a shutter plate is mounted (6). The head plate of the evaporator (7) consists of six holes for the sources and a central one for the rotating rod. For each source one of the holes is meant for a crucible (8) leg mount and another for a ceramic passthrough (9) piece with four smaller holes. Each of the elements mounted in the holes (crucibles and ceramic passthroughs) is supported by a screw coming from the side of the plate. The crucible is manufactured from aluminum nitride. A hollow cup meant for molecules is at the top, a heater wound from molybdenum wire (10) resides in a grove around the cup and a mounting leg protrudes downwards. A type K (chromel-alumel) thermocouple (11) is mounted in a hole in the cup bottom below the heater to provide the most precise control of temperature. The assembly with the leg in the hole provides a way to set the direction of a molecular beam parallel to the evaporator’s main axis. Electrical connections of the heater and the thermocouple are fed through the ceramic passthrough to connect to the feedthrough pins. Separation of each source is provided by the thermal radiation shielding plates (12). The shutter mounted on a rotating rod above the crucibles provides a way of opening and closing a line of sight to the sample.

5 STM INVESTIGATIONS OF MAGNETIC MOLECULES

The importance and potential of introducing single molecules as building blocks in the field of spintronics had been highlighted in a progress article by Bogani *et al.*[105] where the authors discuss the advantages over other approaches to spintronics. The concept of using so called single molecular magnets (SMM) for advancing science and technology sparked interest of many groups working in the new field of spintronics. Here, I am going to focus on observations of magnetic molecules using SP-STM as it is the most direct way to measure spin-dependent properties on the atomic scale.

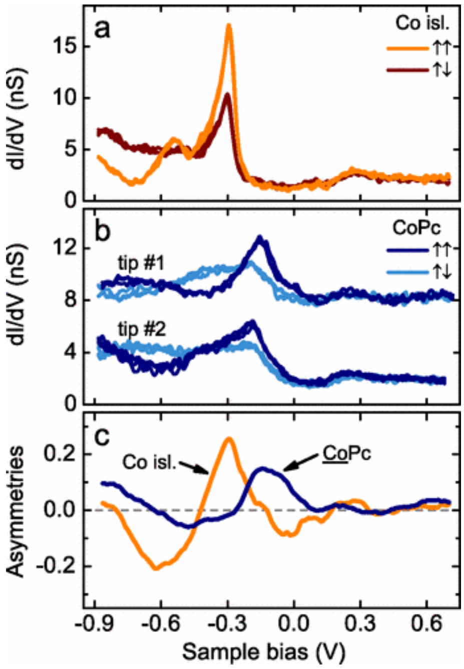

Figure 5.1 Spin-polarized point spectroscopy on (a) the cobalt islands and (b) cobalto-phtalocyanine molecules adsorbed on them. There are two sets of spectra obtained on the molecule with two distinct probe tips (tip #1 and tip #2). (c) Spin asymetries arising from opposite magnetizations extracted from (a) for Co isl. and (b) for CoPc. (Reprinted with permission from Ref. 106. Copyright 2008 by the American Physical Society.)

The first results by Iacovita *et al.*[106] revealed that an adsorbed cobalt-phthalocyanine molecule is ferromagnetically coupled to a Co/Cu(111) substrate. This is clearly visible in Fig. 5.1b, where STS curves obtained with parallel (↑↑) and antiparallel (↑↓) orientations of probe and sample magnetizations are different. The quantitative difference is presented as a spin asymmetry curve in Fig. 5.1c together with a spin asymmetry reference from the substrate (from Fig. 3.8a). Two different mechanisms were proposed: direct exchange coupling between the molecule's Co atom and the underlying island's Co atoms and a 90° superexchange mechanism which additionally involves the molecular N atoms.

This experiment together with others which followed soon after revealed that any molecule adsorbed on a magnetic metal substrate forms a new hybrid state which determines the spin-polarized current flowing through that molecule.[37,107-112] The hybridization between the molecular and substrate states can cause the molecule to manifest amplified or inverted spin-polarization with respect to the bare substrate.[37] The molecule can also gain a delocalized net magnetic moment when interacting with a magnetic substrate despite being nonmagnetic itself.[107] The latter case is presented in Fig. 5.2 where nonmagnetic (metal free) phthalocyanine molecules are adsorbed on a Fe/W(110) substrate. Fig. 5.2a and Fig 5.2b present SP-STM images obtained with different tip magnetization directions. It is clearly visible in Fig 5.2c (spin-polarization image calculated using Eq. 4.14) that the molecule shows locally varying spin-polarization which ranges from attenuation at the edges of the molecule to inversion with maxima at the molecule's C rings.

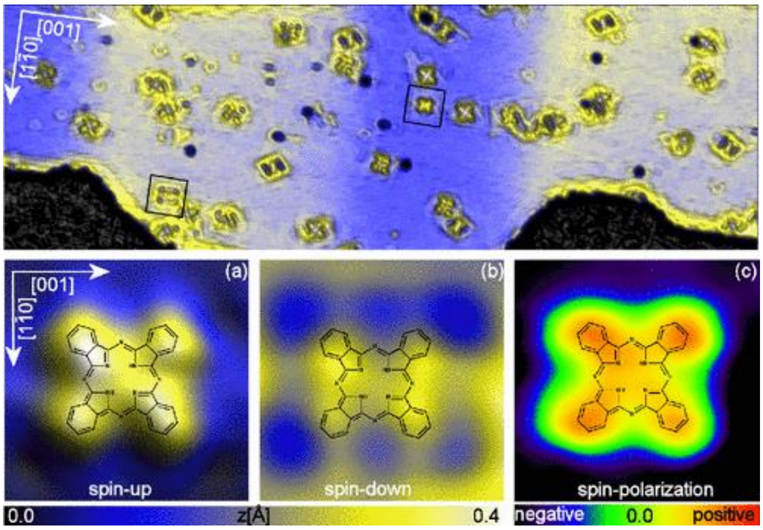

Figure 5.2 Overview SP-STM image of metal free phthalocyanine molecules adsorbed on a multidomain Fe stripe on a W (110) substrate. (a) Spin-up channel and (b) spin-down channel maps had been used to calculate (c) the spin-polarization map. (Reprinted with permission from Ref. 107. Copyright 2010 by the American Physical Society.)

The hybridization of molecule and substrate states can lead to amazingly complex and originally unpredicted long-range magnetic coupling mediated by a skyrmion lattice,[112] which is desirable for certain applications. On the other hand, however, the effects of hybridization are mostly so strong that the molecule's electronic states are severely modified (as discussed in Chapter 2, section 2.4). Based on this fact, there have been concerns about how to separate contributions of the molecules and the substrate to the measured magnetic signal. As an attempt to reduce effects of hybridization, there have been investigations on single molecular magnets adsorbed on insulating surfaces: boron nitride[43] or graphene[44,92,113]. The former study found that such insulating layers preserve the electronic states of adsorbed single molecular magnets. That was proven by using inelastic spin-flip tunneling spectroscopy data which is provided in Fig. 5.3. The tunneling mechanism is presented in the schematics of Fig. 5.3c. It is an indirect multi-step tunneling process which is described in detail in Chapter 4, sub-section 4.1.6. The tunneling conductance ($\mathrm{d}I/\mathrm{d}V$) data presented in Fig. 5.3d exhibit pronounced changes in the measured signal. Those changes are a footprint of an excitation and are better seen in the second derivative ($\mathrm{d}^2I/\mathrm{d}V^2$) as clear maxima at positive bias and minima at negative bias. The color-coded arrows correspond to transitions visualized in Fig. 5.3b. Here, three excitations are visible in zero field. The first observed at 1.4 meV (blue) corresponds to a change of quantum number m preserving the total spin S = 10. The two other excitations observed at higher energies (8.5 meV, red and 15.8 meV, orange) are due to an additional change of the total spin to $S = 9$. Upon applying the external magnetic field of $B = 10$T the excitations shift. The excitation attributed to a change in quantum number shifts to a higher energy of 1.7 meV while the excitations attributed to a simultaneous change in total spin to 5.6 meV and 11.8 meV, respectively. Those spectroscopic features and their behavior in an external magnetic field represent a direct confirmation that the molecules' magnetic states are preserved. However, when comparing the experimental results to the simulated spectra from Fig. 5.3e one can see that the energy states do not directly correspond to one another. The authors claim that the energy positions in the experimental data can change slightly due to the various Mn_{12} molecule conformations when adsorbed in different geometries.

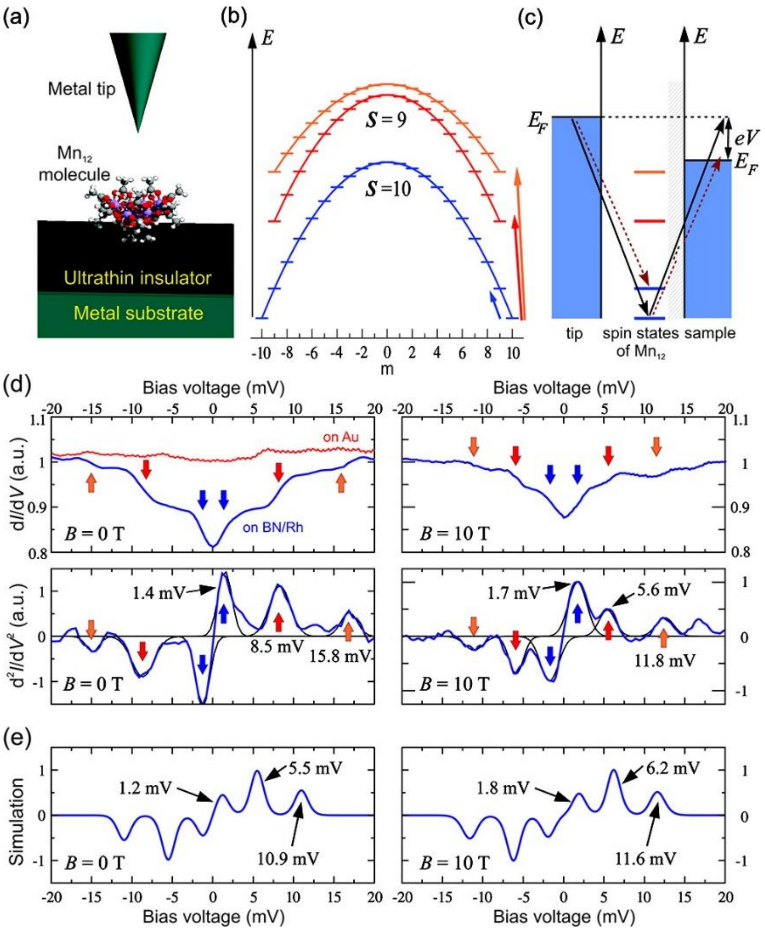

Figure 5.3 Inelastic electron tunneling spectroscopy on isolated Mn_{12} molecule adsorbed on boron nitride. (a) Schematic of the tunneling junction. (b) Energy diagram of the Mn_{12} molecule calculated using the giant spin approximation. (c) Multistep tunneling process via the Mn_{12} states. (d) Tunneling spectra in first (dI/dV) and second (d^2I/dV^2) derivative. (e) Simulated second derivative spectra. (Reprinted with permission from Ref. 43. Copyright 2011 American Chemical Society.)

All of the above described examples of previous studies present unique approaches to single molecule magnetism. However, there are no studies up until now which would combine the different approaches. To address the spatial distribution of spin-polarized states of single adsorbed molecules one must apply the approach of Kahle *et al.*[43] and use ultrathin insulator films as a substrate for the molecules while addressing their magnetic properties in a fashion presented by Iacovita *et al.*[106] and Atodiresei *et al.*[107].

6 RESULTS AND DISCUSSION

"(...) they say a man who never makes mistakes never makes anything else."

~ G. K. Chesterton

Spin-sensitive investigations on CoSal molecules are in the focus of this chapter. Preparation procedures of the probe tip and the investigated sample are provided in the first two sections. Next, the observation of many molecules in an external magnetic field allows for revealing their distinct behavior in different adsorption geometries on the GR/Fe moiré structure. Some of the molecules are ferromagnetically coupled to the substrate while others exhibit an antiferromagnetic alignment with the underlying substrate. Further, some of the molecules in the former case are sensitive to the external magnetic field changes, and therefore the molecule's magnetization direction can be manipulated independent from the substrate – an effect which can be clearly seen in SP-STM data provided in the later part of the chapter. The detection and manipulation of the direction of the magnetic moment of individual CoSal molecules, based on the low level of hybridization with a GR/Fe substrate, is an important milestone towards planar, molecule based all-spin logic devices. The results have been published in the following paper[114]:

E. Sierda, M. Elsebach, R. Wiesendanger, M. Bazarnik
Probing Weakly Hybridized Magnetic Molecules by Single-Atom Magnetometry.
Nano Lett. **19**, 9013-9018 (2019)

6.1 Probe tip preparation

The probe used in this work is an iron coated tungsten tip. First a polycrystalline tungsten wire has been chemically etched in a NaOH solution, rinsed with distilled water and isopropanol, and introduced to the UHV system. Since the process is performed *ex situ*, the tip is covered with an oxide. In order to remove it, the tip is initially annealed in UHV at a temperature of $T \cong 900\text{K}$ in the presence of O_2 (at a pressure of p = 5E-8 mbar) for the duration of t = 30 min and then repeatedly flash annealed *in vacuo* to a temperature of $T \cong 2500$ K for the duration of $t = 15$ s. As a consequence of such a high temperature the apex of the tip is melted and becomes blunt and clean, exhibiting a well-defined (110) surface – a perfect substrate for the growth of thin magnetic films which are required to obtain spin sensitivity. Here ~ 50 mono layers (ML) of Fe have been deposited onto the tip while annealing at 500 K. This procedure leads to a ferromagnetic coating with an in-plane easy axis. Small anisotropy energy renders the probe magnetically soft, hence, its magnetization direction can be easily aligned with an external magnetic field. The presence of a significant stray field at the probe tip's apex can alter the magnetic structure of the sample. Another drawback is the fact that a blunt tip can hardly be used for investigations on highly corrugated surfaces. The blunt tip is prone to accommodate multiple apexes which can simultaneously take part in the tunneling process.

The quality of prepared probe tips, in terms of spatial resolution and spin sensitivity, was assured by measurements on a well-defined and pre-characterized substrate: Co/Ir(111) with Co islands being hard magnets (magnitude of magnetic anisotropy depends on their size).[115]

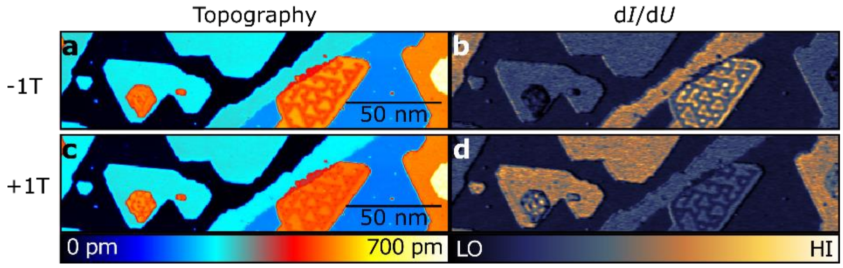

Figure 6.1 Determination of magnetic contrast of a Fe/W probe tip. (a, c) STM topography images and (b, d) differential tunneling conductance (dI/dU) maps of Co islands on Ir(111) obtained in two different external magnetic fields: B = - 1 T (a, b) and B = + 1 T (c, d). Tunneling parameters: U = - 200 mV, I_t = 100 pA, U_{mod} = 50 mV$_{\mathrm{rms}}$, f_{mod} = 971 Hz.

In Fig. 6.1 topography images (Fig. 6.1a,c) as well as differential tunneling conductance maps (Fig. 6.1b,d) are presented for two external magnetic fields of the same magnitude with opposite directions, *i.e.* B = - 1 T (Fig. 6.1a,b) and B = + 1 T (Fig. 6.1c,d). The change in the differential conductance signal visible on all Co islands is a consequence of the probe's inversion of spin-polarization caused by the external magnetic field. Such difference in appearance establishes the magnetic contrast based on the Fe/W probe tip.

6.2 Sample preparation

In this dissertation magnetic properties of 5,5'-dibromocobaltosalophene (CoSal) molecule will be addressed. For the SP-STM experiments, molecules must be adsorbed on a substrate which satisfies specific requirements. First, it must be inert to allow the molecule to preserve its electronic states and magnetic properties (as discussed in Chapter 2, section 2.4). Second, it must stabilize the magnetic moment of the paramagnetic molecule. Third, it must provide both magnetic and non-magnetic reference for SP-STM measurements. No single substrate can satisfy all of the above requirements. However, a combination of pristine graphene and graphene intercalated with magnetic element is suitable.

The procedure of preparing a sample of choice is complex and takes significant time. All of the parameters needed to be precisely adjusted beforehand. The necessary steps are as follows:

1. An Ir single crystal in (111) orientation was cleaned *in vacuo* by repeated cycles of argon sputtering at E = 800 V for t = 30 min (p = 5E-6 mbar), annealing at temperatures ranging from T = 900 K to T = 1500 K in the presence of oxygen (p = 1E-8 mbar) for t = 20 min and a flash annealing at $T \cong$ 1500 K for t = 3 min.
2. A graphene layer was grown on the clean Ir(111) substrate by decomposition of ethylene molecules following the procedure described in Ref. 116, *i.e.* by introducing ethylene gas (p = 3E-8 mbar) for t = 7 min while annealing the iridium crystal to T = 900 K. The crystal was additionally flash annealed at $T \approx$ 1500 K to merge small graphene patches and to make their rotational domains uniform.
3. The crystal was subsequently transferred to the deposition chamber and placed in the XYZα stage. The intercalation process was performed following the procedure described in Ref. 117. Iron was evaporated from an e-beam evaporator with a high rate (I_{flux} = 20 nA) and deposited onto the sample held at an elevated temperature of T = 613 K for t = 12 min. Subsequently it was quickly cooled down to room temperature to avoid alloying.[117-118]
4. The 5,5'-dibromocobaltosalophene (CoSal) molecules were deposited from the molecular evaporator (described in Chapter 4, sub-section 4.2.2) onto the surface held at a temperature of T = 298 K for t = 20 min.

The prepared samples were transferred *in vacuo* into the STM and subsequently cooled down to the measurement temperature of T = 6.5 K.

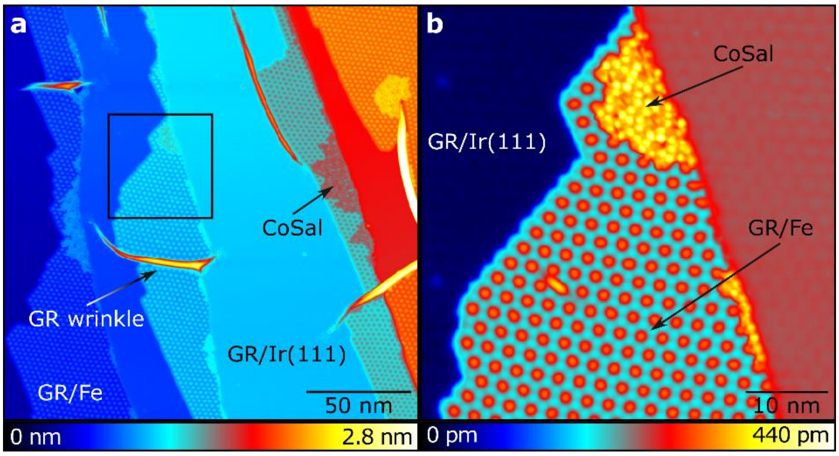

Figure 6.2 STM topography image of a sample containing of CoSal molecules on GR/Fe. (a) A large-scale overview image and (b) a zoom-in on the area marked with a square on (a). Labelled are the following areas: clean graphene adsorbed on the Ir(111) surface (GR/Ir(111)), graphene intercalated with Fe (GR/Fe), an assembly of 5,5'-dibromocobaltosalophene molecules (CoSal) and a special feature, *i.e.* a graphene wrinkle (GR wrinkle). Tunneling parameters: $U = +\ 450$ mV, $I_t = 50$ pA.

An overview STM topography image is presented in Fig. 6.2a with all the characteristic features marked. On this large-scale topography one can observe a non-uniform sample system which consists of distinct areas and irregularities. The main areas to mention are: the pristine graphene on Ir(111) surface (GR/Ir(111)), Fe-intercalated graphene (GR/Fe) and assemblies of CoSal molecules adsorbed solely on GR/Fe areas. As one can observe the CoSal assemblies are always present near surface irregularities, *e.g.* Ir(111) surface terraces or GR wrinkles, and follow a step-flow growth leading to molecular assemblies. The GR wrinkles are created as a consequence of a rapid sample cooling after the final flash during the graphene growth process. However, their presence is desirable as they allow Fe atoms to penetrate the graphene layer and form islands below.[117] Indeed the sample exhibit GR/Fe areas not only near edges of the graphene layer but also close to the GR wrinkles. A zoom-in on the area which is suitable for measurements on adsorbed molecules is presented in Fig. 6.2b. The sample was intentionally prepared to be spatially heterogeneous because each of the areas plays a significant role. The GR/Ir(111) area provides a non-magnetic reference, while the GR/Fe area serves as a magnetic reference[119] and allows the molecules to adsorb there and create an assembly. Additionally, the magnetic character of GR/Fe causes the molecules' magnetic moments to be stabilized for spin-polarized measurements.

6.3 Adsorption geometry of CoSal molecules

All STM images presented in this section were obtained with a functionalized probe tip, to enhance the spatial resolution. The tip functionalization is achieved by intentionally picking up a CoSal molecule.

For the sample system presented in Fig. 6.2 molecules can be adsorbed on two distinct surface areas: GR/Ir(111) and GR/Fe. Both of them are surfaces with a corrugation induced by a moiré pattern. As a consequence of stronger interactions with the substrate, in case of GR/Fe, the moiré pattern and its corrugation are much more pronounced. This can be clearly seen in the Fig. 6.2 where GR/Ir(111) areas appear almost flat. This difference highly influences the molecular adsorption behavior. CoSal molecules adsorbed on GR/Ir(111) are presented in Fig. 6.3. Contours of a few of the molecules are overlaid in the image for easy identification. The low corrugation of the GR/Ir(111) and the weak interaction of the molecules with the substrate allow for a close packed highly ordered arrangement of the molecular assembly.[120-121] The growth is driven by molecule-molecule interactions and follows the main crystallographic directions of the substrate. No other influence of the graphene moiré is observable.

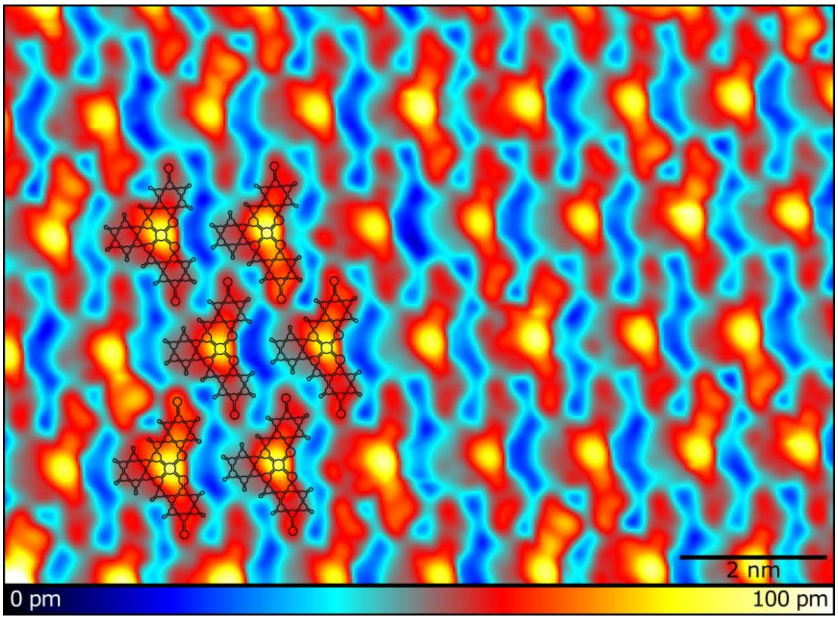

Figure 6.3 An STM image of a close-packed assembly of CoSal molecules adsorbed on pristine GR/Ir(111) obtained with a functionalized probe tip. The contour of a molecule is overlaid in the left part of the image for ease of identification of the adsorbed molecules. Tunneling parameters: $U = +1.5$ V, $I_t = 20$ pA.

For the GR/Fe areas, which will be in the focus of the next sections, the arrangement of the molecular assembly is somewhat different. Such an assembly is presented in Fig. 6.4a. By tunneling at a low bias within the HOMO-LUMO gap of the molecule with such a probe tip, one can obtain intramolecular spatial resolution.[42] Therefore, one can easily identify the protrusion in the middle of each molecule originating from the center Co atom, two protrusions arising from the Br end atoms and the molecular backbone formed by the rest of the atoms.

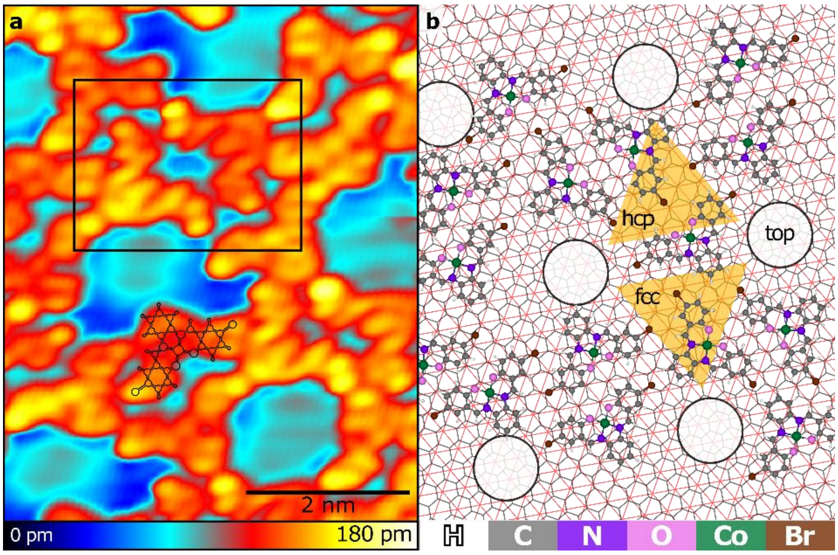

Figure 6.4 : STM topograph of CoSal molecules adsorbed on GR/Fe and corresponding structure model of the imaged area. (a) High resolution STM image of a CoSal molecular assembly obtained with a functionalized probe tip. A contour of a molecule is overlaid for ease of identification. (b) Ball-and-stick models of the molecules overlaid on the atomic lattice of the GR/Fe substrate (GR: black, Fe: red) as deduced from (a). The individual atomic species within the CoSal molecule as well as the specific regions of the GR/Fe moiré structure are labelled. Tunneling parameters: U = + 50 mV, I_t = 50 pA.

For a better understanding of the whole sample system, a schematic drawing of the same area is shown in Fig. 6.4b. Ball-and-stick models of the molecules are depicted on top of a model of the GR/Fe substrate's atomic structure. CoSal molecules are composed of three carbon rings surrounding the central N_2-Co-O_2 entity and two Br atom at each end. Black and red lines represent the substrate: the GR and Fe lattices, respectively. Lattice constants have been extracted from Ref. 122. The moiré structure of the GR/Fe substrate leads to an additional preferential adsorption of the CoSal molecules away from the moiré's top sites. This behavior can be explained by the combined action of intermolecular van-der-Waals forces and repulsive dipolar interactions between molecules and the substrate which drive the molecules away from the moiré's top sites and influence their arrangement relative to one another.[123] Due to the mismatch of the molecule's structure and the moiré pattern of GR/Fe, and in contrast to CoSal adsorbed on pristine GR/Ir(111) as presented in Fig. 6.3, no long-range order of the molecular assembly is observed.

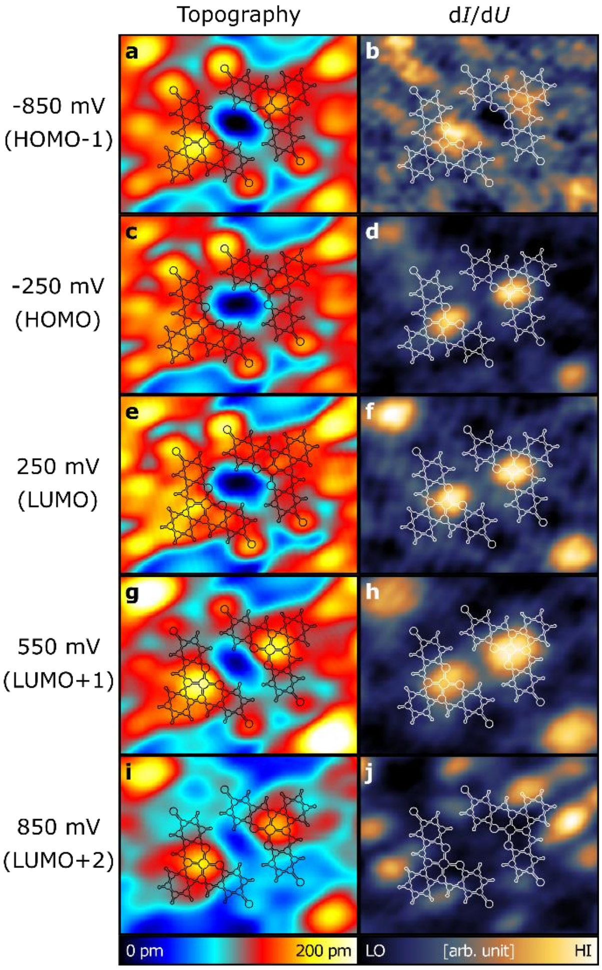

Figure 6.5 High-resolution spatially resolved STS data obtained with a functionalized probe tip. (a, c, e, g, i) STM topography images and (b, d, f, h, j) simultaneously recorded differential tunneling conductance (dI/dU) maps corresponding to molecular states from HOMO-1 to LUMO+2. Contours of the molecules are overlaid for ease of identification. Tunneling parameters: I_t = 50 pA, f_{mod} = 1111.1 Hz, U_{mod} = 50 $\mathrm{mV_{pk\text{-}pk}}$.

Next, I focus on an area around two molecules, as marked with a black square in Fig. 6.4a. Fig. 6.5 shows high-resolution topographic STM images along with the respective differential conductance maps at five different sample bias voltages: U = - 850 mV, U = - 250 mV, U = + 250 mV, U = + 550 mV, and U = + 850 mV, corresponding to states from HOMO-1 to LUMO+2. The two HOMO states and the LUMO state are localized mainly on the Co center and do not extend towards the surrounding atoms. Therefore, their origin is assumed to be of the Co atom. The HOMO-1 state is of significantly lower intensity compared to the other two states mentioned. The LUMO+1 state appears as a protrusion located at the same place but expanding further towards the nitrogen and oxygen atom sites. The LUMO+2 state, on the other hand, originates from the ligand and appears as two oval features on the sides of the molecule's top ring. The identification of those spectroscopic features together with their spatial distribution allows for a recognition of the molecules' positions, even without the use of a functionalized probe tip.

6.4 Single atom magnetometry on CoSal metal center

An area of focus for the spin-polarized tunneling studies consisting of a molecular assembly of 28 individual molecules (in the center), an area of GR/Fe (on the left side) and, separated by an upward step-edge, an area of GR/Ir(111) (on the right side) is presented in Fig. 6.6a. For better visualization a modelled vertical cross-section is provided in Fig. 6.6b. Its location is marked in Fig. 6.6a by a white dashed line. Structural models of the molecules and the positions of the moiré top sites are superimposed onto the STM topography image. The positions were identified based on spatially resolved bias-dependent differential tunneling conductance ($\mathrm{d}I/\mathrm{d}U$) maps as discussed in the previous section.

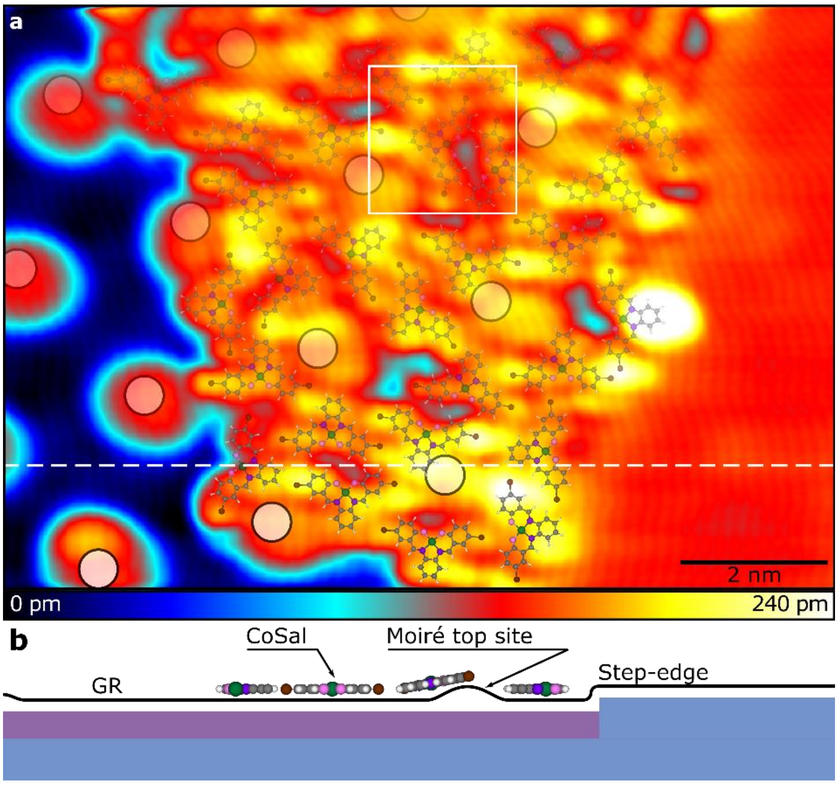

Figure 6.6 (a) STM overview image of the molecular assembly used for subsequent measurements. Ball-and-stick models of the molecules within the assembly are superimposed on the measured STM data, while the positions of the circles represent top sites of the moiré pattern originating from the Fe-intercalated GR layer. (b) A schematic cross-section along the white dashed line in the STM image shown in (a). Tunneling parameters: U = + 50 mV, I_t = 55 pA.

Based on the spatially resolved STS data it is concluded that the maximum signal at the Co-centers for most of the molecules within the assembly is observed at U = + 450 mV. It appears round in shape and is mostly symmetric around the middle of the Co atoms. This particular bias voltage is selected to study the spin-resolved dI/dU signal as a function of an externally applied magnetic field by using a magnetic SP-STM probe tip (preparation is described in section 6.1). The data set consists of a series of dI/dU maps obtained with different externally applied magnetic fields (B = 0.75 T → 5.25 T → - 5.25 T → 0.75 T) in steps of 0.75 T. The field sweep was accompanied by a drift in the xy-plane on the order of a few nanometers, therefore, the scanning area had to be adjusted accordingly. In order to compensate for the drift and small displacement errors, I used an automated algorithm to find the maxima in the dI/dU map of the molecules. The STM image of Fig. 6.7 provided a position reference for the dI/dU maps of the CoSal area (Fig. 6.7b) and the GR/Fe hcp area (Fig. 6.7c). Those areas are further used for spin-resolved differential tunneling conductance signal (G) analysis. Fig. 6.7b presents a slightly larger area than used by the algorithm for the purpose of demonstrating how close signals of neighboring molecules can be.

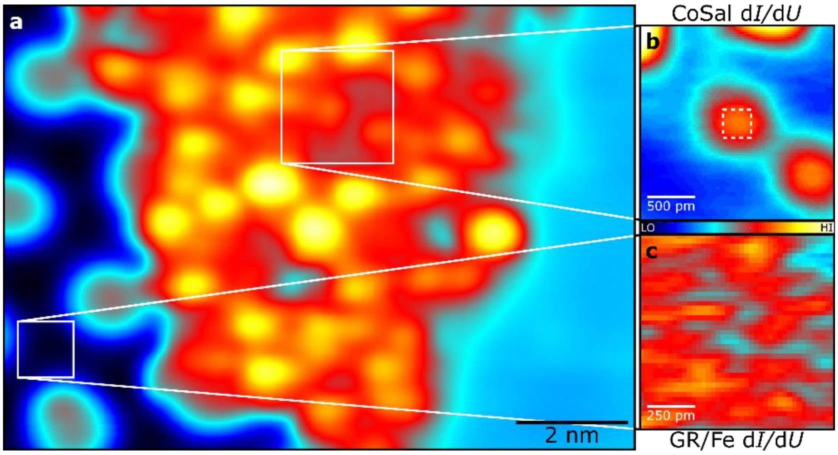

Figure 6.7 Areas for the data extraction for the magnetometry graph. (a) STM overview image of the molecular assembly, (b) spatial distribution of the recorded spin-resolved dI/dU signal of a CoSal molecule, (c) spatial distribution of the recorded spin-resolved dI/dU signal of the hcp area of the GR/Fe substrate. Tunneling parameters: U = + 450 mV, I_t = 55 pA, U_{mod} = 50 mV$_{\mathrm{rms}}$, f_{mod} = 971 Hz.

The average G-values for the two areas were obtained following the procedure:

1. User inputs of coarse coordinates for the CoSal molecule for each dI/dU map (*i.e.* each $\vec{B}$-field).
2. An algorithm finds the maximum value of the dI/dU signal within an area of ~0.2 nm^2 around these coordinates.
3. The G-value for the CoSal molecule is obtained by averaging the dI/dU signal over an area of ~0.1 nm^2 around the maximum dI/dU value (area of dotted square in Fig. 6.7b).
4. The G-value for the GR/Fe region is averaged over a molecule-free area of ~0.7 nm^2 around a point defined by a fixed vector from the CoSal center (whole area depicted in Fig. 6.7c).
5. The error for each G-value is given by the standard deviation of the average.

For the purpose of visualization of the graphs obtaining process as well as presenting all raw data which make it up, I composed a movie which is published as supplementary information to the paper and can be accessed using the in Ref. 124. The first frames of the movie present the exact areas of interest as shown in Fig 6.7. In the following frames, the process of obtaining the magnetization curves is presented.

Following this approach, it was possible to extract local magnetization curves[125] for each of the CoSal molecules in the assembly. However, I will focus on three molecules as examples of different molecule's interaction with the substrate. The first molecule of focus is marked by a white square in Fig. 6.6a and the corresponding magnetization curve is presented in Fig. 6.8a. The CoSal molecule is adsorbed in between the hcp and fcc areas of the GR/Fe moiré structure. This area appears slightly protruded, creating a saddle-type line from one top-site of the moiré to another[119]. The center of the molecule adsorption site is located slightly off the saddle line towards the hcp region. It is of central importance for the discussion later that this position exhibits a lower spin polarization of the electronic states than neighboring hcp and fcc regions.

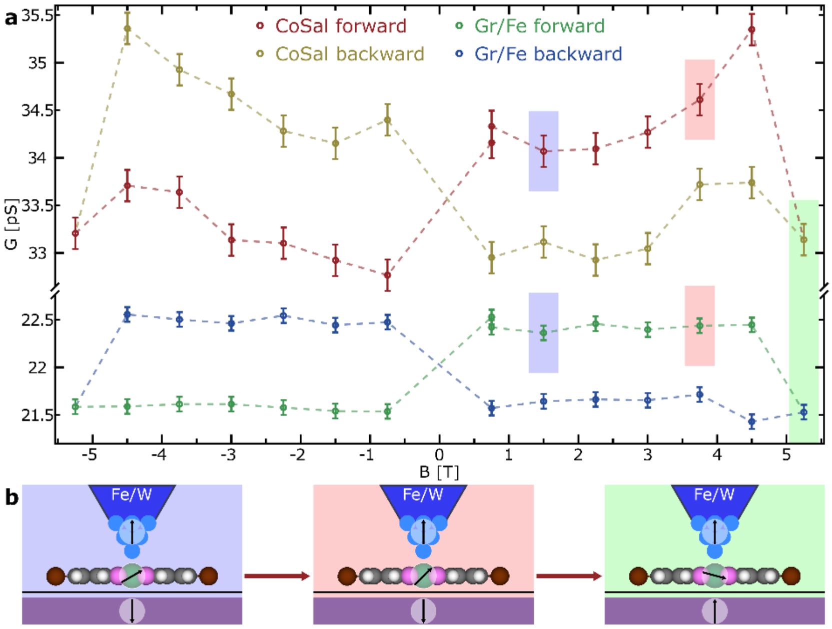

Figure 6.8 Magnetic response of a single adsorbed CoSal molecule's metal center and of the bare GR/Fe substrate (as imaged in the square marked area of Fig. 6.7a) in $\vec{B}$-field range of [-5.25 T, 5.25 T]. (a) Spin-resolved differential tunneling conductance G extracted from the measured dI/dU signal as a function of external out-of-plane magnetic field $\vec{B}$. The error bars correspond to the highest standard deviation of the spatially averaged dI/dU signals. (b) Schematic drawings indicating the magnetization directions of the Fe-coated W-probe tip, the Co-center of the CoSal molecule and the GR/Fe layer for three different B-field values as color coded in (b): 1.50 T (blue), 3.75 T (red), and 5.25 T (green).

For the interpretation of the measured data, it is important to note that the SP-STM probe tip used for these experiments is magnetically soft and requires only B = 0.2 T in order to fully align its magnetization direction with the $\vec{B}$-field. Therefore, while crossing B = 0 T one will always observe a change in the spin-resolved G-signal intensity due to a change of the SP-STM probe magnetization direction. The measured values of G obtained for GR/Fe as a function of $\vec{B}$-field reveal a characteristic magnetic hysteresis. There are two changes of the substrate's magnetization direction occurring: after increasing the $\vec{B}$-field from 4.5 T to 5.25 T and upon decreasing it from -4.5 T to -5.25 T. This behavior is expected for these $\vec{B}$-field values as reported by Decker *et al.*[119]. The GR/Fe loop is inverted here due to the different sample bias voltage used to obtain the data (U = + 450 mV instead of U = + 250 mV at which the main spin-polarized state of GR/Fe is located). The deduced GR/Fe magnetization directions are ↓ for forward [-5.25 T, 4.5 T] and ↑ for backward [-4.5 T, 5.25 T] $\vec{B}$-field sweeps. In contrast, the CoSal response to the $\vec{B}$-field variation is markedly different. It is still mirror-symmetric with respect to B = 0 T and is affected by the above-mentioned changes of the GR/Fe magnetization direction. The very pronounced increase in G-signal as the $\vec{B}$-field rises from 1.5 T to 3.75 T suggests that the z-component of the magnetic moment μ_z of the molecule's Co-center is aligning with the $\vec{B}$-field. Upon reaching the value of the $\vec{B}$-field for which the GR/Fe magnetization direction changes, the magnetic moment of the CoSal molecule follows and its z-component changes direction. A drop in G-signal intensity is strictly connected to changes of the substrate's magnetization. Upon the SP-STM tip's magnetization reversal the behavior described above is repeated for the opposite $\vec{B}$-field direction. Schematic drawings indicating the magnetization directions of all parts of the magnetic tunnel junction for B = 1.5 T, 3.75 T, and 5.25 T are provided in Fig. 6.8b.

The single-molecule magnetization curve of Fig. 6.8a is only part of a full hysteresis loop, *i.e.* magnetic saturation is not yet reached. This is caused by two factors. On the one hand, the GR/Fe magnetization direction changes in relatively low $\vec{B}$-fields and CoSal follows this behavior. On the other hand, using a Brillouin function we have estimated that the $\vec{B}$-field needed to fully align the molecule's magnetic moment (assuming it preserves spin ½), at our measurement temperature of 6.5 K, would be as high as 29 T.

By limiting the magnetic loop to B = 0.75 T → 3.75 T → 0.75 T, the loop of Fig. 6.9 is obtained. In this case the external magnetic field has no influence on the GR/Fe, *i.e.* the substrate's magnetization direction does not change. The change in G-signal recorded for the CoSal molecule is reversable in this case, as opposed to the wider $\vec{B}$-field range loop of Fig. 6.8a.

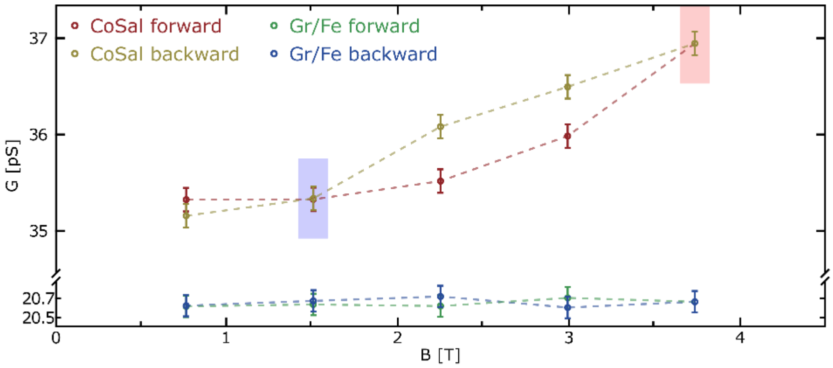

Figure 6.9 Spin-resolved differential tunneling conductance G extracted from the measured $\mathrm{d}I/\mathrm{d}U$ signal averaged over the molecule's Co-metal center and over a bare GR/Fe area next to the molecular assembly in the $\vec{B}$-field range of [0.75 T, 3.75 T]. The error bars correspond to the highest standard deviation of the spatially averaged $\mathrm{d}I/\mathrm{d}U$ signals.

The molecules adsorbed in different parts of the moiré (fcc or hcp) having a stronger interaction with the substrate, show a collinear alignment of their magnetic moment with the underlying substrate. The parallel or antiparallel orientations of the molecules' magnetic moments have been deduced from the behavior of the magnetometry curves recorded on other molecules at higher external magnetic fields of up to 6T. Parallelly oriented molecules lead to a lower conductance when the GR/Fe magnetic moment (and that of the molecule) is antiparallel to that of the SP-STM tip (Fig. 6.10a). After the GR/Fe switches, the molecule switches as well. It is the only change observed in the curve. The antiparallelly oriented molecules start with a higher conductance when the GR/Fe magnetic moment is antiparallel to that of the SP-STM tip (Fig. 6.10b). When the GR/Fe switches at B = 5.25 T the molecule switches as well and the conductance drops. When the field strength increases by additional 0.75 T the conductance starts to rise again. It means that after the switch the magnetic moment of the molecule is being influenced by the external magnetic field and is being aligned with $\vec{B}$ as in case of the molecule discussed earlier (Fig 6.8a).

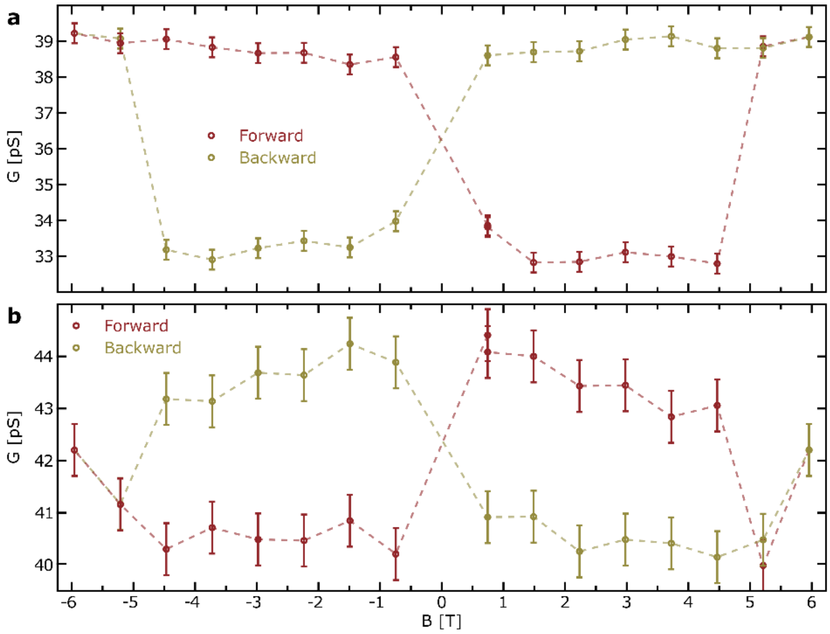

Figure 6.10 Spin-resolved differential tunneling conductance *G* extracted from the measured d*I*/d*U* signal averaged over the molecule's Co-metal center showing two different responses suggesting parallel (a) and antiparallel (b) alignment of the molecule's magnetic moment with respect to the GR/Fe substrate magnetization. The error bars correspond to the highest standard deviation of the spatially averaged d*I*/d*U* signals.

The molecules exhibiting either parallel (P) or antiparallel (A) oriented magnetic moments are marked in the STM topography image (Fig. 6.11). Among the 28 molecules, 16 molecules are magnetically parallel oriented with respect to the substrate and 5 are antiparallel oriented. For the 7 molecules which are not marked in the image, the signal-to-noise ratio in the magnetization curve data is not sufficient to make a clear assignment. The three molecules color-marked in Fig. 6.11 are the ones for which the magnetization curves were presented previously: orange is the first one presented in Fig. 6.8 with weak interaction and antiparallel alignment with respect to the substrate, purple is the one presented in Fig. 6.10a with parallel alignment and green is the one presented in Fig. 6.10b with antiparallel alignment.

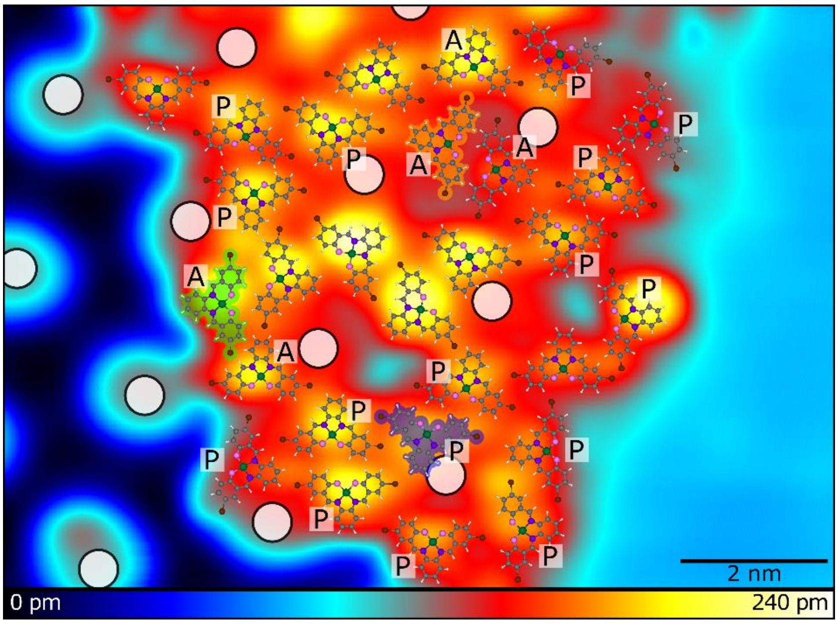

Figure 6.11 An STM overview image of the molecular assembly adsorbed on GR/Fe with overlaid models of molecules. Labels next to the molecules indicate parallel (P) or antiparallel (A) alignment of their magnetic moments with respect to the substrate magnetization direction. Molecules for which the magnetization curves presented in Fig. 5.8a (also 5.9), Fig. 5.10a and Fig. 5.10b were obtained are marked with orange, purple and green colors, respectively. Tunneling parameters: $U = +450$ mV, $I_t = 55$ pA.

6.5 Field dependent spectroscopy investigations

As is apparent from the magnetometry data presented in the previous section, a sufficiently strong $\vec{B}$-field can align the magnetization of the GR/Fe substrate along its direction. Such a change significantly influences the substrate's spin-resolved LDOS and therefore the recorded point-spectroscopy data. The spectra presented in Fig. 6.12 aim to visualize this. They were obtained at the same two places, *i.e.* one at the Co center of the CoSal molecule (Fig. 6.12a) and one at an hcp site of the GR/Fe substrate (Fig. 6.12b), both in the same $\vec{B}$-field. The second set of spectra were obtained after magnetizing the sample with $B = 6$ T, thus, after changing the magnetization direction of the GR/Fe substrate. One can observe that the differences are visible on both occupied and unoccupied states of the normalized spectra. The changes are clearly visible in a spin-asymmetry plot (Fig. 6.12c). The spin-asymmetry was calculated using the Eq. 4.14. The change of the GR/Fe magnetization direction and its spin-polarized LDOS influences the SP-STS of the adsorbed CoSal molecule (see Fig. 6.12a). Therefore, in order to visualize the changes in the SP-STS of a CoSal molecule responding to the applied $\vec{B}$-field, it is important to prevent a change of the substrate's magnetization and perform the experiments within B = [- 4.5 T, 4.5 T].

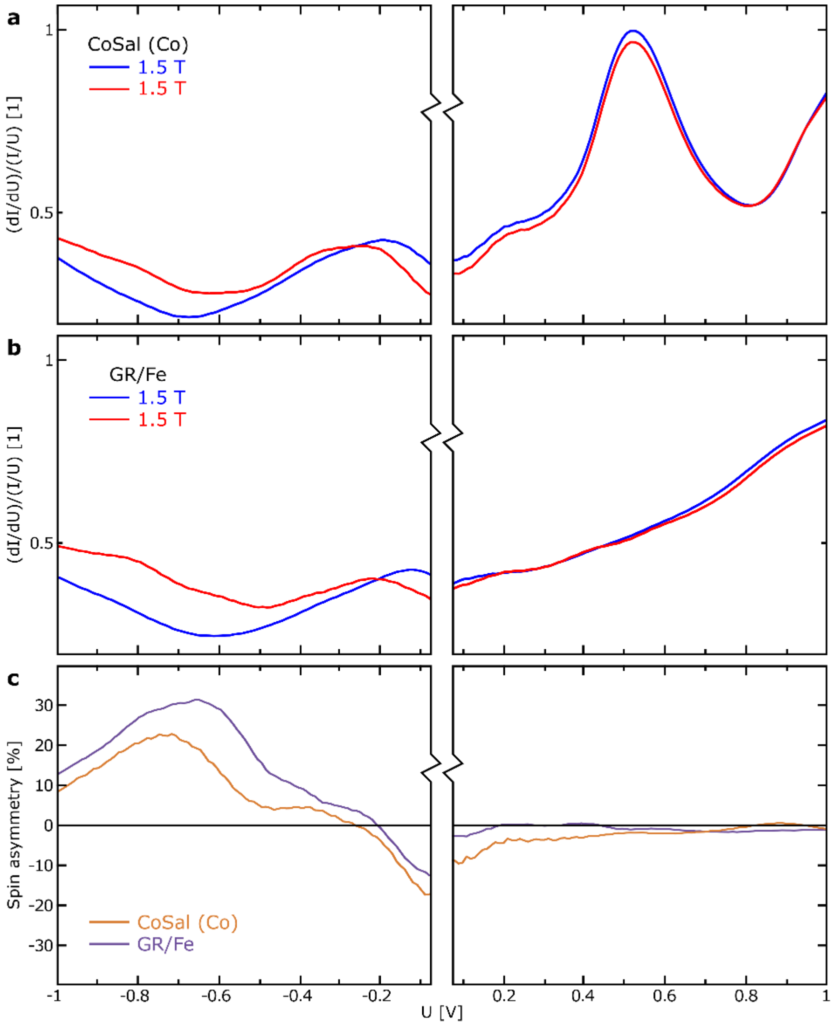

Figure 6.12 Normalized SP-STS data obtained on (a) the CoSal molecule's Co-center and on (b) the bare GR/Fe area next to the molecular assembly at B = 1.5 T and again in the same field after magnetizing the sample in B = 6 T. (c) Spin asymmetry of the CoSal and GR/Fe spectra from (a) and (b), respectively. The measured spin-resolved differential tunneling conductance dI/dU has been divided by I/U and plotted as a function of bias voltage U. Tunneling parameters: U_{stab} = + 1 V, I_{stab} = 55 pA, U_{mod} = 50 mV$_{\mathrm{rms}}$, f_{mod} = 971 Hz, (a) z_{off} = + 100 pm, (b) z_{off} = 0 pm. Every line represents an average over five individual spectra.

Two spin configurations, as outlined in Fig. 6.8b (for B = 1.5 T and B = 3.75 T), have been used for SP-STS experiments in order to visualize the spin-dependent LDOS distributions and the differences between them. Before each SP-STS curve has been recorded, the SP-STM probe was stabilized above a non-magnetic part of the substrate, *i.e.* GR/Ir(111), in order to guarantee a constant and spin-polarization independent sample–tip separation (as discussed in Chapter 4, sub-section 4.1.8). The SP-STS data presented in Fig. 6.13a was measured on the Co center of the CoSal molecule marked in Fig. 6.8a at $B = 1.5$ T, $B = 4.5$ T and again at $B = 1.5$ T. The last measurement is performed to exclude a possibility of the probe tip change as it may be otherwise a source of additional tip-related effects. The changes in the measured spectra obtained in the two different $\vec{B}$-fields reflect the behavior observed for the magnetization curves in Fig. 6.8a, and one can clearly distinguish three bias regions for which spin-dependent tunneling effects are most pronounced: one around U = - 250 mV, one around the peak at U = + 500 mV, and another around U = + 1 V. It is important to note that at the same time, the SP-STS data on bare GR/Ir(111) (see Fig. 6.13b) does not show any changes when comparing the curves acquired at different $\vec{B}$-fields. The spin asymmetry plots in Fig. 6.13c show that the influence of the GR/Fe substrate's spin polarization can be excluded and one can conclude that the changes observed for the CoSal molecule originate purely from its response to the external $\vec{B}$-field. At the same time, the change in the spectra of CoSal does not induce any change in the spectra of GR/Fe. The small spin asymmetry of GR/Fe (0.5 - 1 %) can be caused by a 100 % alignment of the probe tip magnetization in a higher external magnetic field or a slight change of probe's DOS (most of the changes are on the negative bias side) due to, *e.g.*, hydrogen adsorption. It is not, however, comparable to a change originating from the tip remagnetization (see Fig. 6.12). The difference in the Zeeman energy for $B = 1.5$ T and $B = 4.5$ T, *i.e.* $\vec{B}$-fields for which the SP-STS data of Fig. 6.13a have been obtained, equals 0.3 meV and since it is comparable to the thermal broadening, no spin splitting is expected nor observed.

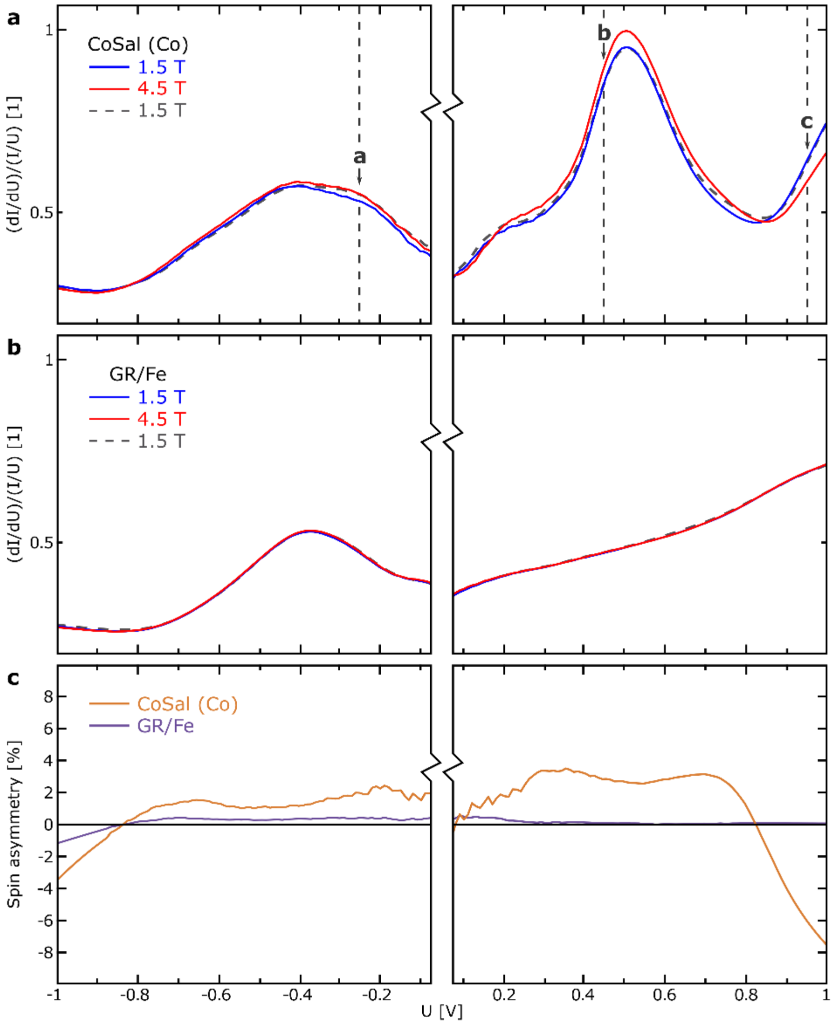

Figure 6.13 Normalized SP-STS data obtained on (a) the CoSal molecule's Co-center and on (b) the bare GR/Fe area next to the molecular assembly at B = 1.5 T, B = 4.5 T and again at B = 1.5 T. (c) Spin asymmetry of the CoSal and GR/Fe spectra from (a) and (b), respectively. The measured spin-resolved differential tunneling conductance dI/dU has been divided by I/U and plotted as a function of bias voltage U. Tunneling parameters: U_{stab} = + 1 V, I_{stab} = 55 pA, U_{mod} = 50 mV$_{\mathrm{rms}}$, f_{mod} = 971 Hz, (a) z_{off} = + 100 pm, (b) z_{off} = 0 pm. Every line represents an average over five individual spectra.

The spatial distributions of the three spin-polarized states revealed by the SP-STS data (Fig. 6.13a) are presented in Fig. 6.14a-c (HOMO at U = - 250 mV, LUMO+1 at U = + 450 mV, and LUMO+2 at U = + 950 mV, respectively) as spin-resolved dI/dU maps. Their corresponding spin asymmetry maps are presented in Fig. 6.14d-f. The spin asymmetry distribution for U = - 250 mV is close to zero, for U = + 450 mV it is of positive sign and particularly strong over the molecule's center atoms, while for U = + 950 mV it is of negative sign and localized in the same area. The additional intensities and asymmetries close to the borders of the selected area originate from neighboring molecules. The reason for the spin asymmetry observed in Fig. 6.14d-f being low is that the magnetic moment of the CoSal molecule aligns only partly with the $\vec{B}$-field. In Fig. 6.14d an almost vanishing spin asymmetry is observed, caused by a low spin polarization of the electronic states at that particular bias voltage. The signs of the spin asymmetries observed in Fig. 6.14e and Fig. 6.14f agree with the SP-STS differences as revealed in Fig. 6.13a. They indicate that the two spin-polarized molecular orbitals located on the N, O and Co atoms of CoSal exhibit two directions with respect to GR/Fe: parallel and antiparallel, depending on the applied sample bias *U*.

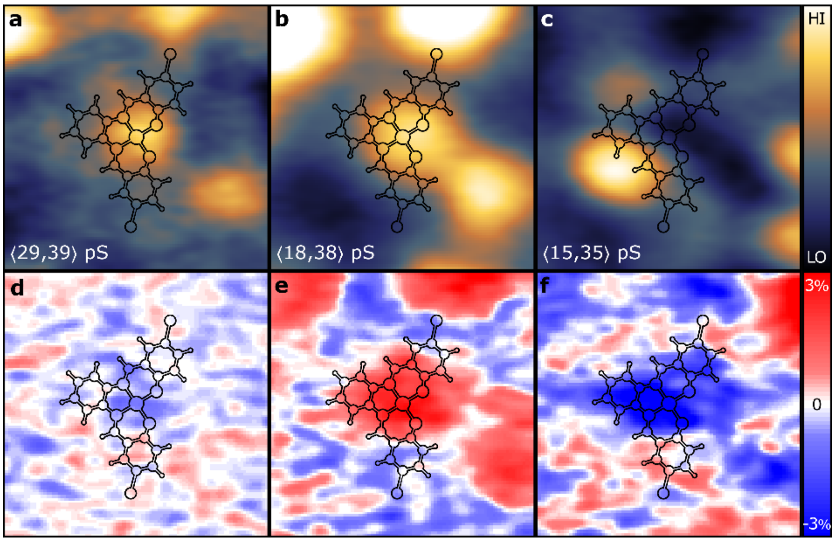

Figure 6.14 (a-c) Spatially and spin-resolved dI/dU maps for three different bias voltages: (a) U = - 250 mV, (b) U = + 450 mV and (c) U = + 950 mV as marked in Fig. 5.13a by dashed lines. (d-e) Spin asymmetry maps for the bias voltages as presented above in (a-c). All maps have been superimposed with the contour of the molecule. Tunneling parameters: I_t = 55 pA, U_{mod} = 50 mV$_{\text{rms}}$, f_{mod} = 971 Hz.

In Chapter 4 sub-section 4.1.6, I discussed the two mechanisms possible in case of elastic tunneling through molecules: *via* molecular state and directly into the substrate. In the case of the experiment discussed here, it is a combination of the two. Tunneling *via* the LUMO+1 state can be observed in STS data (see Fig. 6.13a). The state is short lived as it is very broad in the tunneling spectrum. The tunneling from the state to the substrate is very efficient, and therefore no charging effects are observed. Tunneling also occurs between the probe and the substrate as evident by the non-zero conductance in the HOMO-LUMO gap. As far as spin-polarized tunneling is concerned, the tunnel junction is composed of two magnetic electrodes with a magnetic molecule in-between. The CoSal molecule is coupled to one of the electrodes – the GR/Fe substrate.

6.6 Influence of the adsorption geometry on the magnetic state of CoSal

At low $\vec{B}$-field the molecule's magnetic moment is stabilized by superexchange interactions with the substrate. The same explanation has also been proposed for the similar system of phthalocyanine molecules adsorbed on a Co-intercalated graphene substrate by Avvisati *et al.*[126-127] The spatially averaging techniques used in those two reports suggested either ferro- or antiferromagnetic interactions of the molecule with the substrate, depending on the metal centers of different molecules. The molecules exhibit a significant hybridization of orbitals with the substrate and the interaction between them is driven by a superexchange mechanism. However, in the present study the use of local probe techniques on a different molecule with a different geometry than in the case of Avvisati *et al.* allows the determination of the different adsorption sites which are non-equivalent and exhibit different degrees of magnetic interaction strengths between the molecule and the substrate. Adsorption positions within the GR/Fe moiré unit cell of all molecules which have been studied with respect to their interactions with the substrate are presented in Fig. 6.15b. The reduction of hcp and fcc sites presented in Fig. 6.15c and Fig. 6.15d, respectively, has been possible due to their three-fold symmetry. Thus, all three sub-units of either hcp or fcc sites are equivalent. As it was already evident from Fig. 6.11, all molecules are adsorbed away from the moiré top sites. Most of the molecules (15) are adsorbed at places leading to relatively strong interaction with the substrate, and therefore show a collinear parallel alignment (red) of their magnetic moment with the underlying substrate, in line with the work by Avvisati *et al.* However, some of the molecules (5) with only slightly different adsorption geometry express a weaker interaction with the substrate, and their magnetic alignment is identified as anti-parallel (blue). Even weaker interaction with the substrate allows for the possibility that for some (3) of the anti-parallelly aligned molecules their magnetic moment can be manipulated by an external $\vec{B}$-field.

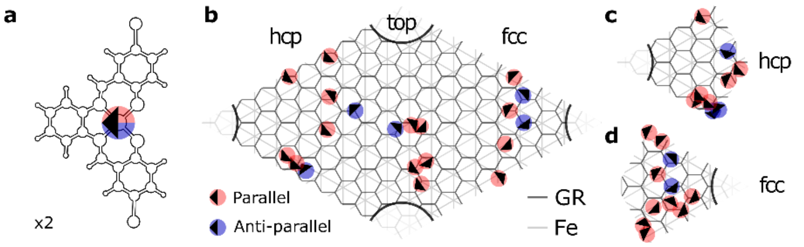

Figure 6.15 Distribution and orientation of all identified molecules within the GR/Fe unit cell. (a) Contour of a molecule and its representation by a simplified dot-arrow symbol. (b) A full GR/Fe moiré unit cell, (c) reduced hcp sub-unit and (d) reduced fcc sub-unit with all molecular positions marked. The scale of the molecule model is twice as big as the scale of the moiré unit cells.

The only possible interaction between the GR/Fe substrate and the CoSal molecule is through the superexchange mechanism described in Chapter 2, section 2.3. Based on previously reported DFT calculations for CoSal molecules the d_{xz} orbital is expected to carry a non-paired electron.[55-56] Its geometry can lead to both ferro- and antiferromagnetic superexchange interaction between the GR/Fe substrate and the CoSal molecule. The strength of the interaction depends on the number of CoSal π-orbitals effectively interacting with the GR π-system (π orbitals are extending far out of molecule's plane). That is the reason why a sufficiently strong $\vec{B}$-field can overcome this interaction and act on the molecule's magnetic moment in some of the adsorption configurations where the molecule interacts with the substrate only weakly. Based on that interpretation even a very small difference in molecule's lateral position or rotation with respect to the GR/Fe moiré unit cell can cause a very significant change of its magnetic interaction with the substrate.

7 CONCLUSIONS AND OUTLOOK

7.1 Main results

In this dissertation I presented the study of a paramagnetic CoSal molecule adsorbed on a ferromagnetic GR/Fe substrate based on spin-polarized tunneling to molecular orbitals. The particular substrate was chosen to separate the substrate's influence on the magnetic state of the molecules. I showed how the adsorption geometry of CoSal molecules on the GR/Fe substrate influences the interaction between them. Depending on the level of hybridization between the molecule's orbitals and the substrate one can expect to probe the molecule in three different states. Relatively strong hybridization will lead to a parallel, while weak hybridization will lead to an anti-parallel orientation of the molecule's and substrate's magnetic moments. If the interaction is weak enough, the molecule's magnetic moment can be manipulated with an external magnetic field, and therefore can respond independently from the substrate. It proves that the molecule upon adsorption preserves its magnetic properties, and therefore such molecules can potentially be used for the design and realization of molecular spintronic devices. The magnetic response of the CoSal molecule was studied by means of single-atom magnetometry and bias-dependent SP-STS experiments. The latter allowed for an unprecedented study of the magnetism of individual molecules including the spatial mapping of three molecular orbitals together with their spin polarization distribution.

7.2 Future prospects

Any measurement performed with scanning probe techniques on a sample system as the one presented here has its limitations. The sole fact that the molecules are adsorbed on inert graphene manifests as the biggest problem. As already mentioned in Chapter 6, section 6.2, the molecules preferentially adsorb on the intercalated areas of the graphene substrate. The interaction between the molecules and the substrate is relatively weak. Therefore, even weak perturbations by the scanning STM probe make the molecule move or even desorb. This requires the use of very small tunneling currents, leading to a weak signal with significant noise. One solution to that problem could be the use of other magnetic molecules as magnetic sensors adsorbed on the tip apex. This approach was recently proposed as a way to increase the spin-polarized signal and sensitivity.[128-129] Further improvements could be made by lowering the base temperature of the experiments. As discussed before the single-molecule magnetization curves presented in Chapter 6, section 6.4, are only part of a full hysteresis loop. One could observe the full hysteresis loop if the measurement temperature would be below 1 K. Such low temperatures would allow for additional experiments based on inelastic electron tunneling and the observation of spin-flip excitations.

One could also think about molecules with a different metal center instead of Co to achieve a higher magnetic moment. Incorporation of Cr would lead to a magnetic moment of 4 μ_B.[25] Unfortunately metalation of salophene molecules by traditional chemical synthesis often leads to solvent contaminations or the product is unstable and either reacts with ambient gases or breaks at elevated temperatures needed for the deposition in UHV. A promising solution to overcome these difficulties is on-surface metalation. This process is performed under UHV conditions on the surface of the sample and is very clean. A recent article reports on an in-depth study of the reaction performed on Co-intercalated graphene.[130] Such in-situ metalated molecules can be studied by the same methods as demonstrated in this dissertation.

The ultimate goal of the investigations on CoSal and similar molecules is the creation of a working molecule-based spin logic device. As discussed in Chapter 3, section 3.3, the prototype of such a device had already been assembled on a Au(111) substrate. However, that prototype could never work due to the fact that the spin of the molecule's Co metal center is Kondo screened on the Au(111) substrate.[55] An inert substrate (as GR used here) seems to be a logical substitution but the substrate would have to allow for an Ullmann reaction to take place. This is necessary because the molecular building blocks must be deposited separately on the substrate and only then react to create the final product (as discussed in Chapter 3, section 3.3). A solution for that problem has been established by our group based on a new approach to the Ullmann reaction. Instead of relying on a substrate catalyzed reaction, we induced the reaction by dosing minute amounts of coinage atoms onto a sample with the molecules being adsorbed on intercalated graphene.[131] the molecular assembly can be then manipulated with an STM probe tip away from the intercalated graphene towards pristine graphene to lower the interaction with the substrate and allow for an intra-chain spin coupling. In this case the magnetic reference needed for spin-polarized STM measurements is still provided by the nearby intercalated graphene.

REFERENCES

[1] G. E. Moore, Cramming more components onto integrated circuits. *Electronics* **38**, 114-117 (1965)

[2] G. E. Moore, Progress In Digital Integrated Electronics. *IEDM Tech. Digest,* 11-13 (1975)

[3] P. S. Chakraborty, A. S. Cardoso, B. R. Wier, A. P. Omprakash, J. D. Cressler, M. Kaynak, B. Tillack, A 0.8 THz f_{MAX} SiGe HBT Operating at 4.3 K. *IEEE Electron Device Lett.* **35**, 151-153 (2014)

[4] M. M. Waldrop, The chips are down for Moore's law. *Nature* **530**, 145-147 (2016)

[5] C. Joachim, J. K. Gimzewski, A. Aviram, Electronics using hybrid-molecular and mono-molecular devices. *Nature* **408**, 541-548 (2000)

[6] L. Lafferentz, F. Ample, H. Yu, S. Hecht, C. Joachim, L. Grill, Conductance of a Single Conjugated Polymer as a Continuous Function of Its Length. *Science* **323**, 1193-1197 (2009)

[7] C. Nacci, F. Ample, D. Bleger, S. Hecht, C. Joachim, L. Grill, Conductance of a single flexible molecular wire composed of alternating donor and acceptor units. *Nat. Commun.* **6**, 7397, doi:10.1038/ncomms8397 (2015)

[8] M. N. Leuenberger, D. Loss, Quantum computing in molecular magnets. *Nature* **410**, 789-793 (2001)

[9] F. A. Zwanenburg, A. S. Dzurak, A. Morello, M. Y. Simmons, L. C. L. Hollenberg, G. Klimeck, S. Rogge, S. N. Coppersmith, M. A. Eriksson, Silicon quantum electronics. *Rev. Mod. Phys.* **85**, 961-1019 (2013)

[10] J. F. Gregg, I. Petej, E. Jouguelet, C. Dennis, Spin electronics—a review. *J. Phys. D: Appl. Phys.* **35**, R121–R155 (2002)

[11] S. Sanvito, Molecular spintronics. *Chem. Soc. Rev.* **40**, 3336–3355 (2011)

[12] A. Candini, S. Klyatskaya, M. Ruben, W. Wernsdorfer, M. Affronte, Graphene Spintronic Devices with Molecular Nanomagnets. *Nano Lett.* **11**, 2634-2639 (2011)

[13] M. Urdampilleta, S. Klyatskaya, J. P. Cleuziou, M. Ruben, W. Wernsdorfer, Supramolecular spin valves. *Nature Mater.* **10**, 502–506 (2011)

[14] S. Delprat, M. Galbiati, S. Tatay, B. Quinard, C. Barraud, F. Petroff, P. Seneor, R. Mattana, Molecular spintronics: the role of spin-dependent hybridization. *J. Phys. D: Appl. Phys.* **51**, 473001 (2018)

[15] L. Bocklage, Coherent THz Transient Spin Currents by Spin Pumping. *Phys Rev. Lett.* **118**, 257202 (2017)

[16] S. V. Vonsovskii, Magnetism. *John Wiley & Sons*, USA, ISBN: 978-0-470-91193-8 (1974)

[17] E. Trémolet de Lacheisserie, D. Gignoux, M. Schlenker, (Eds.) Magnetism: Fundamentals. *Springer*, USA, ISBN: 0-387-22967-1 (2005)

[18] W. Demtröder, Atoms, Molecules and Photons: An Introduction to Atomic-Molecular- and Quantum Physics. *Springer*, Germany, ISBN: 978-3-540-20631-6 (2006)

[19] J. Stöhr, H.C. Siegmann, Magnetism: From Fundamentals to Nanoscale Dynamics. *Springer*, Germany, ISBN: 978-3-540-30282-7 (2006)

[20] D. C. Mattis, The Theory of Magnetism Made Simple. *World Scientific Publishing*, USA, ISBN: 981-238-671-8 (2006)

[21] C. Bréchignac, P. Houdy, M. Lahmani, (Eds.) Nanomaterials and Nanochemistry. *Springer*, Germany, ISBN: 978-3-540-72992-1 (2007)

[22] M. Getzlaff, Fundamentals of Magnetism. *Springer*, Germany, ISBN: 978-3-540-31150-8 (2008)

[23] https://chem.libretexts.org/

[24] I. G. Rau, S. Baumann, S. Rusponi, F. Donati, S. Stepanow, L. Gragnaniello, J. Dreiser, C. Piamonteze, F. Nolting, S. Gangopadhyay, O. R. Albertini, R. M. Macfarlane, C. P. Lutz, B. A. Jones, P. Gambardella, A. J. Heinrich, H. Brune, Reaching the magnetic anisotropy limit of a 3d metal atom. *Science* **344**, 988-992 (2014)

[25] Spin-polarized DFT calculations with double-zeta basis set plus polarization orbitals as implemented in Siesta. Structural relaxation with conjugate gradients (force criterion: 0.04 eV/Å) and electronic structure calculations were performed at the Γ point within generalized gradient approximation (GGA). The magnetic moments per atom are derived from Mulliken population analysis and should be considered a first approximation. Calculations performed by M. Hermanowicz.

[26] H. Bethe, Termaufspaltung in Kristallen. *Ann. Phys.* **3**, 133-208 (1929)

[27] J. H. Van Vleck, Theory of the Variations in Paramagnetic Anisotropy Among Different Salts of the Iron Group. *J. Chem. Phys.* **3**, 803-807 (1935)

[28] Y. Tanabe, S. Sugano, On the Absorption Spectra of Complex Ions. I *J. Phys. Soc. Jpn.* **9**, 753-766 (1954)

[29] Y. Tanabe, S. Sugano, On the Absorption Spectra of Complex Ions. II *J. Phys. Soc. Jpn.* **9**, 766-779 (1954)

[30] C. J. Bellhausen, Introduction to Ligand Field Theory. *McGraw-Hill*, USA (1962)

[31] J. Kanamori, Superexchange interaction and symmetry properties of electron orbitals. *J. Phys. Chem. Solids.* **10**, 87-98 (1959)

[32] P. W. Anderson, New Approach to the Theory of Superexchange Interactions. *Phys. Rev.* **115**, 2-13 (1959)

[33] V. S. Stepanyuk, W. Hergert, K. Wildberger, R. Zeller, P. H. Dederichs, Magnetism of 3d, 4d, and 5d transition-metal impurities on Pd(001) and Pt(001) surfaces. *Phys. Rev. B* **53**, 2121-2125 (1996)

[34] H. C. Manoharan, C. P. Lutz, D. M. Eigler, Quantum mirages formed by coherent projection of electronic structure. *Nature* **403**, 512-515 (2000)

[35] A. J. Heinrich, J. A. Gupta, C. P. Lutz, D. M. Eigler, Single-Atom Spin-Flip Spectroscopy. *Science* **306**, 466-469 (2004)

[36] P. Gambardella, S. Stepanow, A. Dmitriev, J. Honolka, F. M. F. de Groot, M. Lingenfelder, S. S. Gupta, D. D. Sarma, P. Bencok, S. Stanescu, S. Clair, S. Pons, N. Lin, A.P. Seitsonen, H. Brune, J. V. Barth, K. Kern, Supramolecular control of the magnetic anisotropy in two-dimensional high-spin Fe arrays at a metal interface. *Nat. Mater.* **8**, 189-193 (2009)

[37] J. Brede, N. Atodiresei, S. Kuck, P. Lazić, V. Caciuc, Y. Morikawa, G. Hoffmann, S. Blügel, R. Wiesendanger, Spin- and Energy-Dependent Tunneling through a Single Molecule with Intramolecular Spatial Resolution. *Phys. Rev. Lett.* **105**, 047204 (2010)

[38] S. Javaid, M. Bowen, S. Boukari, L. Joly, J.-B. Beaufrand, X. Chen, Y. J. Dappe, F. Scheurer, J.-P. Kappler, J. Arabski, W. Wulfhekel, M. Alouani, E. Beaurepaire, Impact on Interface Spin Polarization of Molecular Bonding to Metallic Surfaces. *Phys. Rev. Lett.* **105**, 077201 (2010)

[39] D. E. Brown, D. J. Moffatt, R. A. Wolkow, Isolation of an Intrinsic Precursor to Molecular Chemisorption. *Science* **279**, 542-544 (1998)

[40] J. Brede, M. Linares, R. Lensen, A. E. Rowan, M. Funk, M. Bröring, G. Hoffmann, R. Wiesendanger, Adsorption and conformation of porphyrins on metallic surfaces. *J. Vac. Sci. Technol. B* **27**, 799-804 (2009)

[41] M. Bazarnik, J. Henzl, R. Czajka, K. Morgenstern, Light driven reactions of single physisorbed azobenzenes. *Chem. Commun.* **47**, 7764–7766 (2011)

[42] J. Repp, G. Meyer, Molecules on Insulating Films: Scanning-Tunneling Microscopy Imaging of Individual Molecular Orbitals. *Phys. Rev. Lett.* **94**, 026803 (2005)

[43] S. Kahle, Z. Deng, N. Malinowski, C. Tonnoir, A. Forment-Aliaga, N. Thontasen, G. Rinke, D. Le, V. Turkowski, T. S. Rahman, S. Rauschenbach, M. Ternes, K. Kern, The Quantum Magnetism of Individual Manganese-12-Acetate Molecular Magnets Anchored at Surfaces. *Nano Lett.* **12**, 518-521 (2012)

[44] J. Dreiser, G. E. Pacchioni, F. Donati, L. Gragnaniello, A. Cavallin, K. S. Pedersen, J. Bendix, B. Delley, M. Pivetta, S. Rusponi, H. Brune, Out-of-Plane Alignment of Er(trensal) Easy Magnetization Axes Using Graphene. *ACS Nano* **10**, 2887–2892 (2016)

[45] L. L. Patera, F. Queck, P. Scheuerer, N. Moll, J. Repp, Accessing a Charged Intermediate State Involved in the Excitation of Single Molecules. *Phys Rev. Lett.* **123**, 016001 (2019)

[46] S. A. Wolf, D. D. Awschalom, R. A. Buhrman, J. M. Daughton, S. von Molnár, M. L. Roukes, A. Y. Chtchelkanova, D. M. Treger, Spintronics: A Spin-Based Electronics Vision for the Future. *Science* **294**, 1488-1495 (2001)

[47] M. Johnson, R. H. Silsbee, Interfacial Charge-Spin Coupling: Injection and Detection of Spin Magnetization in Metals. *Phys. Rev. Lett.* **55**, 1790-1793 (1985)

[48] M. N. Baibich, J. M. Broto, A. Fert, F. Nguyen Van Dau, F. Petroff, P. Etienne, G. Creuzet, A. Friederich, J. Chazelas, Giant Magnetoresistance of Fe(001)/Cr(001) Magnetic Superlattices. *Phys. Rev. Lett.* **61**, 2472-2475 (1988)

[49] G. Binasch, P. Grünberg, F. Saurenbach, W. Zinn, Enhanced magnetoresistance in layered magnetic structures with antiferromagnetic interlayer exchange. *Phys. Rev. B* **39**, 4828-4830 (1989)

[50] J. A. Gupta, D. D. Awschalom, X. Peng, A. P. Alivisatos, Spin coherence in semiconductor quantum dots. *Phys. Rev. B* **59**, R10421-R10424 (1999)

[51] J. A. Gupta, R. Knobel, N. Samarth, D. D. Awschalom, Ultrafast Manipulation of Electron Spin Coherence. *Science* **292**, 2458-2461 (2001)

[52] A. A. Khajetoorians, J. Wiebe, B. Chilian, R. Wiesendanger, Realizing All-Spin–Based Logic Operations Atom by Atom. *Science* **332**, 1062-1064 (2011)

[53] The International Roadmap For Devices And Systems: 2018 Update, IEEE (2019)

[54] L. Zhou, J. Wiebe, S. Lounis, E. Vedmedenko, F. Meier, S. Blügel, P. H. Dederichs, R. Wiesendanger, Strength and directionality of surface Ruderman–Kittel–Kasuya–Yosida interaction mapped on the atomic scale. *Nat. Phys.* **6**, 187-191 (2010)

[55] A. DiLullo, S. H. Chang, N. Baadji, K. Clark, J. P. Klöckner, M. H. Prosenc, S. Sanvito, R. Wiesendanger, G. Hoffmann, S. W. Hla, Molecular Kondo chain. *Nano Lett.* **12**, 3174–3179 (2012)

[56] M. Bazarnik, B. Bugenhagen, M. Elsebach, E. Sierda, A. Frank, M. H. Prosenc, R. Wiesendanger, Toward Tailored All-Spin Molecular Devices. *Nano Lett.* **16**, 577–582 (2016)

[57] S. W. Hla, L. Bartels, G. Meyer, K. H. Rieder, Inducing All Steps of a Chemical Reaction with the Scanning Tunneling Microscope Tip: Towards Single Molecule Engineering. *Phys. Rev. Lett.* **85**, 2777-2780 (2000)

[58] M. Xi, B. E. Bent, Iodobenzene on Cu(111): formation and coupling of adsorbed phenyl groups. *Surf. Sci.* **278**, 19-32 (1992)

[59] M. Xi, B. E. Bent, Mechanisms of the Ullmann Coupling Reaction in Adsorbed Monolayers. *J. Am. Chem. Soc.* **115**, 7426-7433 (1993)

[60] M. M. Blake, S. U. Nanayakkara, S. A. Claridge, L. C. Fernández-Torres, E. C. H. Sykes, P. S. Weiss, Identifying Reactive Intermediates in the Ullmann Coupling Reaction by Scanning Tunneling Microscopy and Spectroscopy. *J. Phys. Chem. A* **113**, 13167-13172 (2009)

[61] Y. Q. Zhang, N. Kepčija, M. Kleinschrodt, K. Diller, S. Fischer, A.C. Papageorgiou, A. Allegretti, J. Björk, S. Klyatskaya, F. Klappenberger, M. Ruben, J. V. Barth, Homo-coupling of terminal alkynes on a noble metal surface. *Nat. Commun.* **3**, 1286, doi:10.1038/ncomms2291 (2012)

[62] L. Grill, M. Dyer, L. Lafferentz, M. Persson, M. V. Peters, S. Hecht, Nano-architectures by covalent assembly of molecular building blocks. *Nat. Nano.* **2**, 687-691 (2007)

[63] F. Ullmann, J. Bielecki, Ueber Synthesen in der Biphenylreihe. *Ber. Dtsch. Chem. Ges.* **34**, 2174-2185 (1901)

[64] J. A. Lipton-Duffin, O. Ivasenko, D. F. Perepichka, F. Rosei, Synthesis of Polyphenylene Molecular Wires by Surface-Confined Polymerization. *Small* **5**, 592-597 (2009)

[65] T. Lin, X. S. Shang, J. Adisoejoso, P. N. Liu, N. Lin Steering On-Surface Polymerization with Metal-Directed Template. *J. Am. Chem. Soc.* **135**, 3576-3582 (2013)

[66] K. A. Simonov, N. A. Vinogradov, A. S. Vinogradov, A. V. Generalov, E. M. Zagrebina, N. Mårtensson, A. A. Cafolla, T. Carpy, J. P. Cunniffe, A. B. Preobrajenski, Effect of Substrate Chemistry on the Bottom-Up Fabrication of Graphene Nanoribbons: Combined Core-Level Spectroscopy and STM Study. *J. Phys. Chem. C* **118**, 12532-12540 (2014)

[67] J. Eichhorn, D. Nieckarz, O. Ochs, D. Samanta, M. Schmittel, P. J. Szabelski, M. Lackinger, On-Surface Ullmann Coupling: The Influence of Kinetic Reaction Parameters on the Morphology and Quality of Covalent Networks. *ACS Nano* **8**, 7880-7889 (2014)

[68] P. Han, K. Akagi, F. F. Canova, H. Mutoh, S. Shiraki, K. Iwaya, P. S. Weiss, N. Asao, T. Hitosugi, Bottom-Up Graphene-Nanoribbon Fabrication Reveals Chiral Edges and Enantioselectivity. *ACS Nano* **8**, 9181-9187 (2014)

[69] L. Massimi, O. Ourdjini, L. Lafferentz, M. Koch, L. Grill, E. Cavaliere, L. Gavioli, C. Cardoso, D. Prezzi, E. Molinari, A. Ferretti, C. Mariani, M. G. Betti, Surface-Assisted Reactions toward Formation of Graphene Nanoribbons on Au(110) Surface. *J. Phys. Chem. C* **119**, 2427-2437 (2015)

[70] A. Basagni, F. Sedona, C. A. Pignedoli, M. Cattelan, L. Nicolas, M. Casarin, M. Sambi, Molecules-oligomers-nanowires-graphene nanoribbons: a bottom-up stepwise on-surface covalent synthesis preserving long-range order. *J. Am. Chem. Soc.* **137**, 1802-1808 (2015)

[71] K. A. Simonov, N. A. Vinogradov, A. S. Vinogradov, A. V. Generalov, E. M. Zagrebina, G. I. Svirskiy, A. A. Cafolla, T. Carpy, J. P. Cunniffe, T. Taketsugu, A. Lyalin, N. Mårtensson, A. B. Preobrajenski, From Graphene Nanoribbons on Cu(111) to Nanographene on Cu(110): Critical Role of Substrate Structure in the Bottom-Up Fabrication Strategy. *ACS Nano* **9**, 8997-9011 (2015)

[72] B. Cirera, J. Björk, R. Otero, J. M. Gellego, R. Miranda, D. Ecija, Efficient Lanthanide Catalyzed Debromination and Oligomeric Length-Controlled Ullmann Coupling of Aryl Halides. *J. Phys. Chem. C* **121**, 8033-8041 (2017)

[73] Q. Fan, T. Wang, J. Dai, J. Kuttner, G. Hilt, J. M. Gottfried, J. Zhu, On-Surface Pseudo-High-Dilution Synthesis of Macrocycles: Principle and Mechanism. *ACS Nano* **11**, 5070-5079 (2017)

[74] E. Sierda, M. Abadía, J. Brede, M. Elsebach, B. Bugenhagen, M. H. Prosenc, M. Bazarnik, R. Wiesendanger, On-Surface Oligomerization of SelfoTerminating Molecular Chains for the Design of Spintronic Devices. *ACS Nano* **11**, 9200–9206 (2017)

[75] C. García-Fernández, E. Sierda, M. Abadía, B. Bugenhagen, M. H. Prosenc, R. Wiesendanger, M. Bazarnik, J. E. Ortega, J. Brede, E. Matito, A. Arnau, Exploring the Relation Between Intramolecular Conjugation and Band Dispersion in One-Dimensional Polymers. *J. Phys. Chem. C* **121**, 27118–27125 (2017)

[76] G. Binning, H. Rohrer, Ch. Gerber, E. Weibel, Surface Studies by Scanning Tunneling Microscopy. *Phys. Rev. Lett.* **49**, 57-61 (1982)

[77] K. Besocke, An easily operable scanning tunneling microscope. *Surf. Sci.* **181**, 145-153 (1987)

[78] S. H. Pan, International Patent Publication No. WO 93/19494 (International Bureau, World Intellectual Property Organization), September 30, 1993.

[79] J. Bardeen, Tunneling from a many-body point of view.
Phys. Rev. Lett. **6**, 57-59 (1961)

[80] J. Tersoff, D. R. Hamann, Theory and application for the scanning tunneling microscope. *Phys Rev. Lett.* **50**, 1998-2001 (1983)

[81] J. Tersoff, D. R. Hamann, Theory of scanning tunneling microscope.
Phys. Rev. B **31**, 805-814 (1985)

[82] C. J. Chen, Theory of scanning tunneling spectroscopy.
J. Vac. Sci. Technol. A **6**, 319-322 (1988)

[83] C. J. Chen, Tunneling matrix elements in three-dimensional space: The derivative rule and the sum rule. *Phys. Rev. B* **42**, 8841-8857 (1990)

[84] C. J. Chen, Introduction to Scanning Tunneling Microscopy,
Oxford University Press, USA (1993)

[85] R. Wiesendanger, H. J. Güntherodt, G. Güntherodt, R. J. Gambino, R. Ruf, Observation of Vacuum Tunneling of Spin-Polarized Electrons with the Scanning Tunneling Microscope. *Phys. Rev. Lett.* **65**, 247-250 (1990)

[86] A. A. Khajetoorians, S. Lounis, B. Chilian, A. T. Costa, L. Zhou, D. L. Mills, J. Wiebe, R. Wiesendanger, Itinerant Nature of Atom-Magnetization Excitation by Tunneling Electrons. *Phys. Rev. Lett.* **106**, 037205 (2011)

[87] J. C. Sloncewski, Conductance and exchange coupling of two ferromagnets separated by a tunneling barrier. *Phys. Rev. B* **39**, 6995 (1989)

[88] R. Wiesendanger, Spin mapping at the nanoscale and atomic scale.
Rev. Mod. Phys. **81**, 1495-1550 (2009)

[89] S. Heinze, First-Principles Theory of Scanning Tunneling Microscopy Applied to Transition-Metal Surfaces. Doctoral dissertation, Universität Hamburg (2000)

[90] D. Wortmann, S. Heinze, Ph. Kurz, G. Bihlmayer, S. Blügel, Resolving Complex Atomic-Scale Spin Structures by Spin-Polarized Scanning Tunneling Microscopy. *Phys. Rev. Lett.* **86**, 4132-4135 (2001)

[91] T. L. A. Tran, T. Q. Le, J. G. M. Sanderink, W. G. van der Wiel, M. P. de Jong, The Multistep Tunneling Analogue of Conductivity Mismatch in Organic Spin Valves. *Adv. Funct. Mater.* **22**, 1180–1189 (2012)

[92] L. Gragnaniello, F. Paschke, P. Erler, P. Schmitt, N. Barth, S. Simon, H. Brune, S. Rusponi, M. Fonin, Uniaxial 2D Superlattice of Fe4 Molecular Magnets on Graphene. *Nano Lett.* **17**, 7177–7182 (2017)

[93] C. Timm, Tunneling through molecules and quantum dots: Master-equation approaches. *Phys. Rev. B* **77**, 195416 (2008)

[94] W. C. Michels, N. L. Curtis, A Pentode Lock-In Amplifier of High Frequency Selectivity. *Rev. Sci. Instrum.* **12**, 444 (1941)

[95] A. Kubetzka, O. Pietzsch, M. Bode, R. Wiesendanger, Determining the spin polarization of surfaces by spin-polarized scanning tunneling spectroscopy. *Appl. Phys. A* **76**, 873–877 (2003)

[96] R. M. Feenstra, J. A. Stroscio, A. P. Fein, Tunneling spectroscopy of the Si(111)2x1 surface. *Surf. Sci.* **181**, 295-306 (1987)

[97] H. Brunner, P. J. van der Houwen, The Numerical Solution of Volterra Equations. *North-Holland*, Amsterdam (1986)

[98] V. A. Ukraintsev, Data evaluation technique for electron-tunneling spectroscopy. *Phys. Rev. B* **53**, 11176-11185 (1996)

[99] Y. Yayon, X. Lu, M. F. Crommie, Bimodal electronic structure of isolated Co atoms on Pt(111). *Phys. Rev. B* **73**, 155401 (2006)

[100] J. Li, W. D. Schneider, R. Berndt, Local density of states from spectroscopic scanning-tunneling-microscope images: Ag(111).
Phys. Rev. B **56**, 7656-7659 (1997)

[101] C. Wittneven, R. Dombrowski, S. H. Pan, R. Wiesendanger, A low-temperature ultrahigh-vacuum scanning tunneling microscope with rotatable magnetic field. *Rev. Sci. Instrum.* **68**, 3806 (1997).

[102] J. H. Brede, Spin-Polarized Scanning Tunneling Microscopy and Spectroscopy of Phthalocyanine Molecules on Surfaces.
Doctoral dissertation, Universität Hamburg (2011)

[103] J. Wiebe, A. Wachowiak, F. Meier, D. Haude, T. Foster, M. Morgenstern, R. Wiesendanger, A 300 mK ultra-high vacuum scanning tunneling microscope for spin-resolved spectroscopy at high energy resolution.
Rev. Sci. Instrum. **75**, 4871 (2004).

[104] G. Mariotto, M. D. Angelo, I. V. Shvets, Dynamic behavior of a piezowalker, inertial and frictional configurations. *Rev. Sci. Instrum.* **70**, 3651 (1999).

[105] L. Bogani, W. Wernsdorfer, Molecular spintronics using single-molecule magnets. *Nat. Mater.* 7, 179-186 (2008)

[106] C. Iacovita, M.V. Rastei, B.W. Heinrich, T. Brumme, J. Kortus, L. Limot, J. P. Bucher, Visualizing the Spin of Individual Cobalt-Phthalocyanine Molecules.
Phys. Rrev. Lett. **101**, 116602 (2008)

[107] N. Atodiresei, J. Brede, P. Lazić, V. Caciuc, G. Hoffmann, R. Wiesendanger, S. Blügel, Design of the Local Spin Polarization at the Organic-Ferromagnetic Interface. *Phys. Rev. Lett.* **105**, 066601 (2010)

[108] A. Mugarza, C. Krull, R. Robles, S. Stepanow, G. Ceballos, P. Gambardella, Spin coupling and relaxation inside molecule–metal contacts.
Nat. Commun. **2**, 490, doi: 10.1038/ncomms1497 (2011)

[109] S. L. Kawahara, J. Lagoute, V. Repain, C. Chacon, Y. Girard, S. Rousset, A. Smogunov, C. Barreteau, Large Magnetoresistance through a Single Molecule due to a Spin-Split Hybridized Orbital. *Nano Lett.* **12**, 4558–4563 (2012)

[110] J. Brede, R. Wiesendanger, Spin-resolved characterization of single cobalt phthalocyanine molecules on a ferromagnetic support.
Phys. Rev. B **86**, 184423 (2012)

[111] J. Schwöbel, Y. Fu, J. Brede, A. Dilullo, G. Hoffmann, S. Klyatskaya, M. Ruben, R. Wiesendanger, Real-space observation of spin-split molecular orbitals of adsorbed single-molecule magnets.
Nat. Commun. **3**, 953, doi: 10.1038/ncomms1953 (2012)

[112] J. Brede, N. Atodiresei, V. Caciuc, M. Bazarnik, A. Al-Zubi, S. Blügel, R. Wiesendanger, Long-range magnetic coupling between nanoscale organic–metal hybrids mediated by a nanoskyrmion lattice. *Nat. Nano.* **9**, 1018-1023 (2014)

[113] F. Paschke, P. Erler, V. Enenkel, L. Gragnaniello, M. Fonin, Bulk-Like Magnetic Signature of Individual Fe_4H Molecular Magnets on Graphene.
ACS Nano **13**, 780–785 (2019)

[114] Sierda, E. Elsebach, M. Wiesendanger, R. Bazarnik, M. Probing Weakly Hybridized Magnetic Molecules by Single-Atom Magnetometry. Nano Lett. 19, 9013-9018 (2019)

[115] J. E. Bickel, F. Meier, J.Brede, A. Kubetzka, K. von Bergmann, R. Wiesendanger, Magnetic properties of monolayer Co islands on Ir(111) probed by spin-resolved scanning tunneling microscopy. *Phys. Rev. B* **84**, 054454 (2011)

[116] A. T. N'Diaye, J. Coraux, T. N. Plasa, C. Busseand, T. Michely, Structure of epitaxial graphene on Ir(111). *New Journal of Physics* **10**, 043033 (2008).

[117] M. Bazarnik, R. Decker, J. Brede, R. Wiesendanger, Multi-layer and multi-component intercalation at the graphene/Ir(111) interface.
Surf. Sci. **639**, 70–74 (2015).

[118] J. Brede, J. Sławińska, M. Abadia, C. Rogero, J. E. Ortega, I. Piquero-Zulaica, J. Lobo-Checa, A. Arnau, J. I. Cerdá Tuning the Graphene on Ir(111) adsorption regime by Fe/Ir surface-alloying. *2D Mater.* **4**, 015016 (2016)

[119] R. Decker M. Bazarnik, N. Atodiresei, V. Caciuc, S. Blügel, R. Wiesendanger, Local tunnel magnetoresistance of an iron intercalated graphene-based heterostructure. *J. Phys.: Condens. Matter* **26**, 394004 (2014).

[120] S. Kuck, S. H. Chang. J. P. Klöckner, M. H. Prosenc, G. Hoffmann, R. Wiesendanger, Steering Two-Dimensional Molecular Growth via Dipolar Interaction. *ChemPhysChem* **10**, 2008-2011 (2009)

[121] J. Mao, H. Zhang, Y. Jiang, Y. Pan, M. Gao, W. Xiao, H.-J. Gao, Tunability of Supramolecular Kagome Lattices of Magnetic Phthalocyanines Using Graphene-Based Moiré Patterns as Templates. *J. Am. Chem. Soc.* **131**, 14136-14137 (2009)

[122] P. Zeller, S. Günther, What are the possible moiré patterns of graphene on hexagonally packed surfaces? Universal solution for hexagonal coincidence lattices, derived by a geometric construction.
New Journal of Physics **16**, 083028 (2014)

[123] M. Bazarnik, J. Brede, R. Decker, R. Wiesendanger, Tailoring Molecular Self-Assembly of Magnetic Phthalocyanine Molecules on Fe- and Co-Intercalated Graphene. *ACS Nano* 7, 11341-11349 (2013)

[124] https://pubs.acs.org/doi/suppl/10.1021/acs.nanolett.9b04025/suppl_file/nl9b04025_si_002.mp4

[125] F. Meier, L. Zhou, J. Wiebe, R. Wiesendanger, Revealing Magnetic Interactions from Single-Atom Magnetization Curves. *Science* **320**, 82-86 (2008)

[126] G. Avvisati, P. Gargiani, P. Mondelli, F. Presel, A. Baraldi, M. G. Betti, Superexchange pathways stabilize the magnetic coupling of MnPc with Co in a spin interface mediated by graphene. *Phys. Rev B* **98**, 115412 (2018)

[127] G. Avvisati, C. Cardoso, D. Varsano, A. Ferretti, P. Gargiani, M. G. Betti, Ferromagnetic and Antiferromagnetic Coupling of Spin Molecular Interfaces with High Thermal Stability. *Nano Lett.* **18**, 2268–2273 (2018)

[128] G. Czap, P. J. Wagner, F. Xue, L. Gu, J. Li, J. Yao, R. Wu, W. Ho, Probing and imaging spin interactions with a magnetic single-molecule sensor.
Science **364**, 670–673 (2019)

[129] B. Verlhac, N. Bachellier, L. Garnier, M. Ormaza, P. Abufager, R. Robles, M.-L. Bocquet, M. Ternes, N. Lorente, L. Limot, Atomic-scale spin sensing with a single molecule at the apex of a scanning tunneling microscope.
Science **366**, 623–627 (2019)

[130] M. Elsebach, E. Sierda, J. J. Goedecke, L. Bignardi, M. Hermanowicz, M. Rohde, R. Wiesendanger, M. Bazarnik, In Situ Synthesis of Metal-Salophene Complexes on Intercalated Graphene. *J. Phys. Chem. C* **124**, 4279-4287 (2020)

[131] M. Elsebach, E. Sierda, J. J. Goedecke, L. Bignardi, R. Wiesendanger, M. Bazarnik, Ullmann coupling on graphene. (unpublished)

PUBLICATIONS

1. M. Elsebach, E. Sierda, J. Jirapon Goedecke, L. Bignardi, M. Hermanowicz, M. Rohde, R. Wiesendanger, M. Bazarnik
   In Situ Synthesis of Metal-Salophene Complexes on Intercalated Graphene.
   J. Phys. Chem. C **124**, 4279-4287 (2020)
   DOI: 10.1021/acs.jpcc.9b08943
2. E. Sierda, M. Elsebach, R. Wiesendanger, M. Bazarnik
   Probing weakly hybridized magnetic molecules by single-atom magnetometry.
   Nano Lett. **19**, 9013-9018 (2019)
   DOI: 10.1021/acs.nanolett.9b04025
3. M. Bazarnik, M. Abadia, J. Brede, M. Hermanowicz, E. Sierda, M. Elsebach, T. Hänke, R. Wiesendanger
   Atomically resolved magnetic structure of a Gd-Au surface alloy.
   Phys Rev. B **99**, 174419 (2019)
   DOI: 10.1103/PhysRevB.99.174419
4. C. García-Fernández, E. Sierda, M. Abadia, B. Bugenhagen, M. H. Prosenc, R. Wiesendanger, M. Bazarnik, J. E. Ortega, J. Brede, E. Matito, A. Arnau
   Exploring the relation between intramolecular conjugation and band dispersion in one-dimensional polymers.
   J. Phys. Chem. C **121**, 27118-27125 (2017)
   DOI: 10.1021/acs.jpcc.7b08668
5. E. Sierda, M. Abadia, J. Brede, M. Elsebach, B. Bugenhagen, M. H. Prosenc, M. Bazarnik, R. Wiesendanger
   On-surface oligomerization of self-terminating molecular chains for the design of spintronic devices.
   ACS Nano **11**, 9200-9206 (2017)
   DOI: 10.1021/acsnano.7b04194
6. M. Bazarnik, B. Bugenhagen, M. Elsebach, E. Sierda, A. Frank, M. H. Prosenc, R. Wiesendanger
   Toward Tailored All-Spin Molecular Devices.
   Nano Lett. **16**, 577–582 (2016)
   DOI: 10.1021/acs.nanolett.5b04266

CONFERENCE CONTRIBUTIONS

Invited Talk

1. E. Sierda,
Inżynieria nano-drutów organicznych z atomami magnetycznymi.
VIII Seminarium Badania prowadzone metodami skaningowej mikroskopii bliskich oddziaływań STM/AFM 2016, Zakopane, Poland (domestic) 3 – 7.12.2016

Contributed Talks

1. E. Sierda, M. Elsebach, M. Bazarnik, R. Wiesendanger
Magnetism of adsorbed Co-Salophene molecules revealed by SP-STM.
8th International Conference on Scanning Probe Microscopy and Related Methods SPS'19, Hamburg, Germany (international) 17 – 20.06.2019

2. E. Sierda, M. Elsebach, M. Bazarnik, R. Wiesendanger
Magnetism of Salophene based molecules.
DPG-Frühjahrstagung 2018, Berlin, Germany (international) 11 – 16.03.2018

3. E. Sierda
Self-terminating molecular chains for application in spintronic devices.
VI Kongres Polskiego Towarzystwa Próżniowego, Trzebnica, (domestic) 6 – 9.09.2016

4. E. Sierda, M. Abadia, J. Brede, M. Elsebach, B. Bugenhagen, M. H. Prosenc, M. Bazarnik, R. Wiesendanger
Co-Salophene oligomers growth on Ag(111) and Au(111) surfaces – STM and XPS study.
International Conference and Exhibition NANOTECH POLAND 2016, Poznan (international) 22 – 25.06.2016

5. E. Sierda, M. Bazarnik, B. Bugenhagen, M. H. Prosenc, W. Koczorowski, R. Wiesendanger
On-surface preparation of self-terminating molecular chains.
31st European Conference on Surface Science ECOSS 31, Barcelona (International) 31.08 – 4.09.2015

6. E. Sierda, M. Bazarnik, B. Bugenhagen, M. H. Prosenc, W. Koczorowski, R. Wiesendanger
On-surface preparation of self-terminating molecular chains.
7th International Conference on Scanning Probe Microscopy and Related Methods SPS'15, Poznań, (international) 21 – 24.06.2015

7. E. Sierda, M. Bazarnik, B. Bugenhagen, M. H. Prosenc, W. Koczorowski, R. Wiesendanger
Samoczynnie zwieńczające się łańcuchy molekularne.
VIII Seminarium Badania prowadzone metodami skaningowej mikroskopii bliskich oddziaływań STM/AFM 2014, Zakopane (domestic) 3 – 7.12.2014

Contributed Posters

1. E. Sierda, M. Bazarnik, B. Bugenhagen, M. H. Prosenc, W. Koczorowski, R. Wiesendanger
Covalently bonded molecular chains.
3rd workshop on surface structures Electron Diffraction for Quantitative Surface Structure Determination ICSOS 2015, Łódź (international) 19 – 27.06.2015

2. E. Sierda, M. Bazarnik, B. Bugenhagen, M. H. Prosenc, R. Wiesendanger, W. Koczorowski.
Self-assembly process of cobaltosalophen molecules.
7th National Conference on Nanotechnology Nano Conference 2015, Poznań (international) 24 – 27.06.2015

ACKNOWLEDGMENTS

I would like to thank each and every one who helped and supported me during my work on this dissertation.

First and foremost, Prof. Dr. Roland Wiesendanger and Dr. Maciej Bazarnik for their trust and confidence as well as providing me with the opportunity to make this dissertation in the research group. Prof. Dr. Roland Wiesendanger provided continuous support, knowledge and granted me access to the excellent scientific equipment and experience of the group R. Dr. Maciej Bazarnik was always a source of great assistance and encouragement in the good and the bad times. The years working with him, in and out of the lab, shaped me to be a scientist I am today. My doctorate work could only be completed with all of those things in place.

Next, I want to thank all the co-authors of the publications I am a part of. For all the hard work, valuable input and contribution to the final paper.

I want to express my gratitude to all the colleagues and members of the group R, both former and current, for the friendly and productive atmosphere which I could enjoy over the years. Special thanks go to: Micha Elsebach, Julia Goedecke, Dr. Torben Hänke, Cody Friesen, Dr. Jonas Warmuth, Dr. Manuel Steinbrecher, Dr. Jonas Harm, Dr. Annand Kamlapure, Dr. Jens Wiebe, Lucas Schneider, Dr. Jan Hermanau, Philip Beck, Dr. Lasse Cornils, Dr. Josef Grenz, Dr. Khai Ton That, Howon Kim, Dominik Schreyer, Alexander Schäffer, Dr. Anika Schlenhoff, Dr. Stefan Krause, Hermann Osterhage, Jonas Koch and Dr. Niklas Romming.

My experimental work could not have been done without the support from the technical staff (Helium-team, electronic- and mechanical-workshop), including but not limited to: Michael Langer, Norbert Dix, Dieter Klatt, Michael Brandt and Horst Biedermann.

I would like to gratefully acknowledge financial support for my position, trips and materials from the Office of Naval Research Science and Technology *via* Grant No. N00014-16-1-2900.

I also thank to my former supervisors and colleagues from Poznan, where I started my adventure with science. Special thanks go to: Prof. Dr. hab. Ryszard Czajka, Dr. hab. Wojciech Koczorowski, Marta Przychodnia, Dr. Semir El-Ahmar and Dr. Tomasz Grzela.

Many thanks go also to my colleagues from Interdyscyplinary Doctoral Studies in Nanotechnology: Michał Dudek, Konrad Jaroszewski, Dr. Anna Kondratowicz, Dr. Tomasz Szatkowski and Marek Weiss. We actually shared some good times during the years, especially during our stay in Italy.

Apart from the academic world, I want to thank the people very important to me on a personal level. I want to show my appreciation to my friends: Mikołaj, Karolina, Bartek, Ania, Basia, Przemek, Olga, Mateusz, Michał, Paweł, Magda, Monika. I thank you all for your support on different stages of my life and for lots of the good and the bad memories we share. Those shaped the person I am today and I deeply value them all.

Finally, and most importantly, I thank the people who are most dear to me: my parents Jan and Halina, my sister Justyna and my extended family. Their love, patience and unconditional support during my journey and especially the long years apart during my stay in Hamburg. Thank you for always being there for me to overcome the challenges in my life.

Eidesstattliche Versicherung / Declaration on oath

Hiermit versichere ich an Eides statt, die vorliegende Dissertationsschrift selbst verfasst und keine anderen als die angegebenen Hilfsmittel und Quellen benutzt zu haben.

Die eingereichte schriftliche Fassung entspricht der auf dem elektronischen Speichermedium.

Die Dissertation wurde in der vorgelegten oder einer ähnlichen Form nicht schon einmal in einem früheren Promotionsverfahren angenommen oder als ungenügend beurteilt.

Hamburg, den 03.03.2020

____

Unterschrift des Doktoranden